Cryogenic, coincident fluorescence, electron, and ion beam microscopy

Track and isolate proteins for near-atomic resolution electron cryo-microscopy

Boltje, D.B.

DOI
10.4233/uuid:b2bfbcac-a938-493d-a09d-380ad6132d61

Publication date
2025

Document Version
Final published version

Citation (APA)
Boltje, D. B. (2025). *Cryogenic, coincident fluorescence, electron, and ion beam microscopy: Track and isolate proteins for near-atomic resolution electron cryo-microscopy*. [Dissertation (TU Delft), Delft University of Technology]. https://doi.org/10.4233/uuid:b2bfbcac-a938-493d-a09d-380ad6132d61

Important note
To cite this publication, please use the final published version (if applicable).
Please check the document version above.

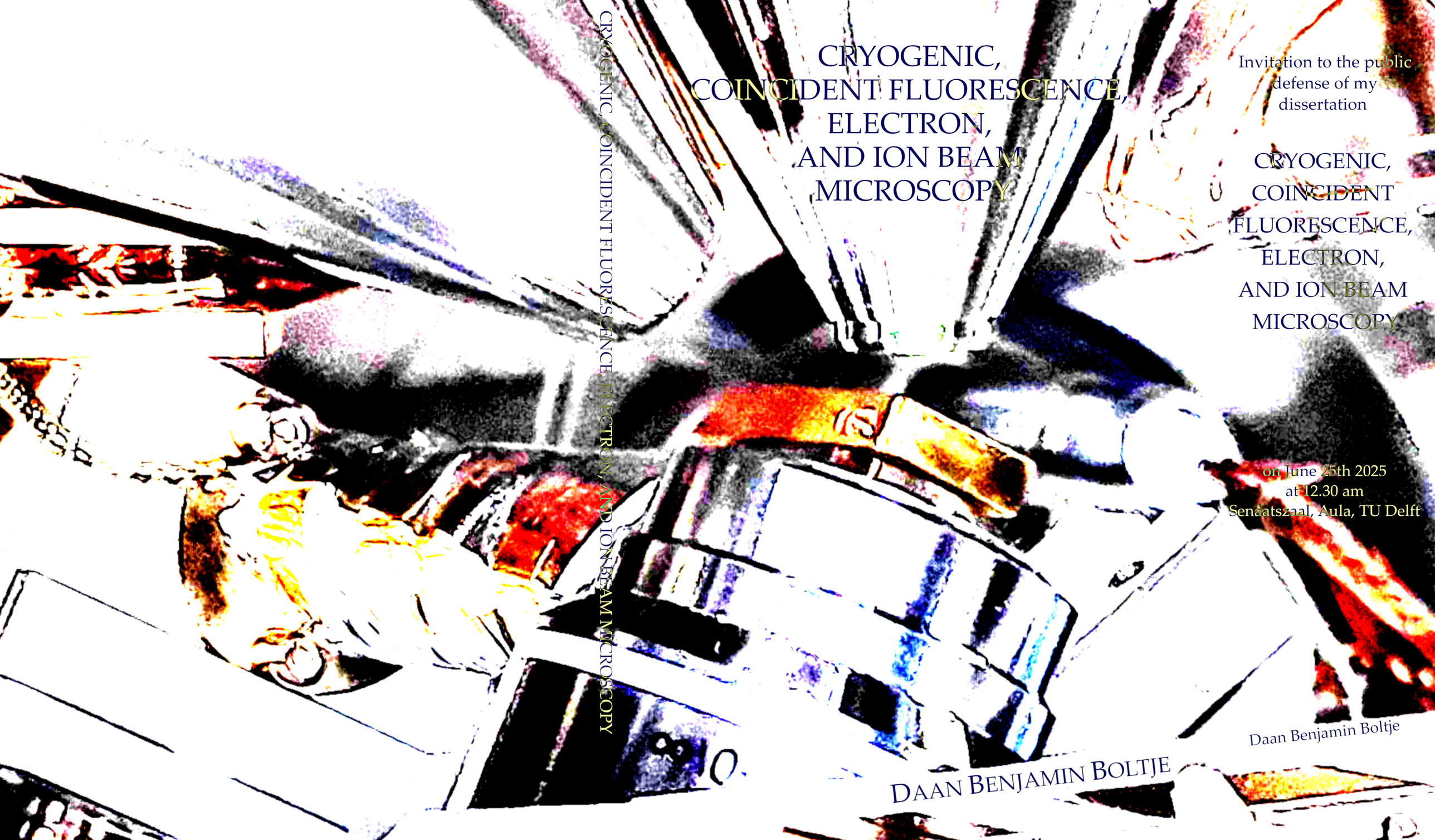

CRYOGENIC, COINCIDENT FLUORESCENCE, ELECTRON, AND ION BEAM MICROSCOPY

CRYOGENIC, COINCIDENT FLUORESCENCE, ELECTRON, AND ION BEAM MICROSCOPY

Invitation to the public defense of my dissertation

CRYOGENIC, COINCIDENT FLUORESCENCE, ELECTRON, AND ION BEAM MICROSCOPY

on June 25th 2025
at 12.30 am
Senaatszaal, Aula, TU Delft

Daan Benjamin Boltje

DAAN BENJAMIN BOLTJE

PROPOSITIONS

accompanying the dissertation

CRYOGENIC, COINCIDENT FLUORESCENCE, ELECTRON, AND ION BEAM MICROSCOPY

by

DAAN BENJAMIN BOLTJE

1. Fluorescence targets embedded in the interior of cells can be preserved inside a sub-diffraction limit sized lamella, through real-time measurements of fluorescence using a wide-field fluorescence microscope integrated in coincidence with a focused ion beam system. *This proposition pertains to this dissertation (chapter 2).*

2. Refractive index mismatch induced axial scaling is depth dependent and needs to be corrected for effective high resolution imaging and localization. *This proposition pertains to this dissertation (chapter 3).*

3. Live feedback on the thickness and uniformity of prepared lamellae reduces workflow complexity, and increases the lamella yield. *This proposition pertains to this dissertation (chapter 4).*

4. The Joule-Thompson cooling cycle can also be utilized to manufacture a very sensitive detector of water impurities in gas.

5. In experimental science, the key to overcoming challenges often lies not in reducing complexity, but to strategically allow it in e.g. the experimental design or procedure.

6. Synergy in an industrial doctoral track is only possible if all parties involved show equal amount of interest.

7. After the conception of new technology collaborating with early adopters is as important as developing said technology.

8. A protocolized healthcare system undermines patient care.

9. Procrastination makes life worthy of living.

10. The number of FTEs per published article, student, and doctoral candidate at Dutch universities has dropped over 7-fold in the past 20 years. While technological advances have boosted productivity, they only partly offset the significantly increased workload.

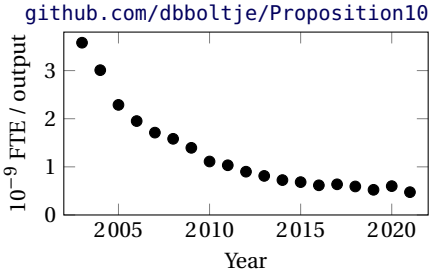

These propositions are regarded as opposable and defendable, and have been approved as such by the promotors prof. dr. ir. J.P. Hoogenboom and dr. A.J. Jakobi.

STELLINGEN

behorende bij het proefschrift

CRYOGENIC, COINCIDENT FLUORESCENCE, ELECTRON, AND ION BEAM MICROSCOPY

door

DAAN BENJAMIN BOLTJE

1. Fluorescerende kleurstoffen ingebed in cellen kunnen behouden blijven in een gesneden sectie dunner dan de diffractielimiet, door middel van real-time metingen van fluorescentie met een fluorescentiemicroscoop, geïntegreerd in een gefocusseerd ionenbundelsysteem. *Deze stelling heeft betrekking op dit proefschrift (hoofdstuk 2).*

2. Axiale schalingseffecten geinduceerd door een verschil in brekingsindex zijn diepte afhankelijk en moeten gecorrigeerd worden voor hoge-resolutie beeldvorming en lokalisatie. *Deze stelling heeft betrekking op dit proefschrift (hoofdstuk 3).*

3. Directe terugkoppeling op de dikte en uniformiteit van geprepareerde secties vermindert de complexiteit van de workflow en verhoogt de opbrengst. *Deze stelling heeft betrekking op dit proefschrift (hoofdstuk 4).*

4. De Joule-Thomson koelcyclus kan ook gebruikt worden om een zeer gevoelige detector voor water onzuiverheden in een gas te vervaardigen.

5. In de experimentele wetenschap ligt de sleutel tot het overwinnen van uitdagingen vaak niet in het verminderen van complexiteit, maar in het strategisch toestaan ervan, bijvoorbeeld in het ontwerp of de procedure van het experiment.

6. Synergie in een industrieel promotietraject is alleen mogelijk als alle betrokken partijen evenveel interesse tonen.

7. Na de ontwikkeling van nieuwe technologie is samenwerken met vroege gebruikers net zo belangrijk als het ontwikkelen van die technologie.

8. Geprotocolleerde gezondheidszorg ondermijnt de zorg voor patiënten.

9. Procrastineren maakt het leven levenswaardig.

10. Het aantal FTEs per gepubliceerd artikel, student, en promovendus aan Nederlandse universiteiten is in de laatste 20 jaar met een factor >7 afgenomen. Hoewel technologische vooruitgang de productiviteit heeft verhoogd, compenseert dit slechts gedeeltelijk de aanzienlijk toegenomen werkdruk.

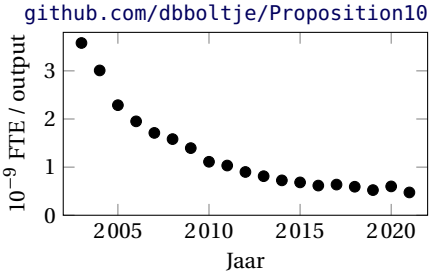

Deze stellingen worden opponeerbaar en verdedigbaar geacht en zijn als zodanig goedgekeurd door de promotors prof. dr. ir. J.P. Hoogenboom en dr. A.J. Jakobi.

CRYOGENIC, COINCIDENT FLUORESCENCE, ELECTRON, AND ION BEAM MICROSCOPY

Track and isolate proteins for near-atomic resolution electron cryo-microscopy

CRYOGENIC, COINCIDENT FLUORESCENCE, ELECTRON, AND ION BEAM MICROSCOPY

Track and isolate proteins for near-atomic resolution electron cryo-microscopy

PROEFSCHRIFT

ter verkrijging van de graad van doctor
aan de Technische Universiteit Delft,
op gezag van de Rector Magnificus Prof. dr. ir. T.H.J.J. van der Hagen,
voorzitter van het College voor Promoties,
in het openbaar te verdedigen op woensdag 25 juni 2025 om 12:30 uur

door

DAAN BENJAMIN BOLTJE

Master of Science in Physics,
Universität Stuttgart, Stuttgart, Germany,
geboren te Almere, Nederland.

Dit proefschrift is goedgekeurd door de promotoren.

Samenstelling promotiecommissie:

Rector Magnificus,	voorzitter
Prof. dr. ir. J.P. Hoogenboom	Technische Universiteit Delft, promotor
Dr. A.J. Jakobi	Technische Universiteit Delft, promotor

Onafhankelijke leden:	
Dr. M.E. Aubin-Tam	Technische Universiteit Delft
Dr. P. Dahlberg	Stanford University, USA
Prof.dr. G. Förster	Universiteit Utrecht
Prof.dr.ir. A.J. Koster	Leiden Universitair Medisch Centrum
Prof.dr. B. Rieger	Technische Universiteit Delft
Prof.dr. C. Joo	Technische Universiteit Delft, reservelid

Keywords:	Correlative microscopy, fluorescence microscopy, scanning electron microscopy, focused ion beam milling, lamella fabrication, cyrogenic electron tomograpgy
Printed by:	Ipskamp Printing B.V.
Front & Back:	Color photograph of the coincident 3-beam configuration, with rescaled contrast and color saturation through the auto contrast and brightness function in ImageJ.
Flipbook:	Snaphots from a movie recorded whilst milling a frozen hydrated lamella. Reflected light (grayscale) and fluoresence microscopy (green) images are overlaid.

ISBN 978-94-6384-784-1

An electronic version of this dissertation is available at
http://repository.tudelft.nl/.

Thuis ben je, waar het leven een puinhoop is.

— Arnon Grunberg

CONTENTS

ABSTRACT

Cryogenic electron tomography (cryo-ET) is a powerful technique to investigate biological structures at molecular resolution, which is essential to understand complex processes that occur within cells. Among imaging techniques, cryo-ET stands out as it can reveal intricate structural details without the need for external labels or markers. However, its utility is often limited by the difficulties in preparing high-quality biological samples. A major challenge is the production of ultra-thin, frozen-hydrated sections, or lamellae, ideally between 100 and 200 nm thick, which must remain below the inelastic mean-free path of electrons in vitreous ice. Achieving such thin, artifact-free sections is crucial for high resolution imaging.

The primary method for producing lamellae is through cryogenic focused ion beam (cryo-FIB), where the ion beam is used to fabricate the lamella, carefully removing cellular material to expose a cross-section of the cell for imaging with transmission electron microscope (TEM). This process is delicate and requires numerous steps to be performed with precision. Despite several improvements in cryo-FIB workflows, the accurate targeting of specific regions of interest for milling, particularly in complex biological specimens, remains a major hurdle.

In recent years, various improvements and refinements have been made to the cryo-FIB milling workflow, enhancing throughput, reliability, sample yield, and quality. Different approaches to fluorescence imaging have been incorperated into the cryo-FIB workflow to aid in selecting target cells and identifying regions of interest for milling. The aim of this dissertation is to further develop *in-situ* fluorescence microscopy for the cryo-FIB milling workflow through integration, and coincidence imaging, thus gaining additional insights *while* milling, and exploring new prospects and applications in structural biology.

Chapter 2 describes the experimental setup that was designed and built to prepare frozen-hydrated lamellae using *in-situ* fluorescence microscopy to guide the milling. By integrating a small cryogenic cooler, a custom positioning stage, and an inverted widefield fluorescence microscope into an existing focused ion beam scanning electron microscope, a three-beam cryogenic correlative microscope is created. As a result, fluorescence microscopy can guide targeting at each milling step, which is confirmed by transmission electron microscope tomogram reconstructions. Being able to observe the sample during and after milling improves the success rate and efficiency of producing lamellae for high-resolution imaging.

While integrating fluorescence microscopy (FM) into the cryo-FIB setup helps guide the process by identifying specific cells or subcellular regions, the refractive index mismatches between different materials during fluorescence microscopy lead to registration errors and distortions, making it difficult to precisely localize the target which can result in sub optimal milling and poor sample quality. To address this,

we develop a depth-dependent, non-linear scaling theory in Chapter 3, generally applicable in the field of optical microscopy. This analytical theory allows the calculation of a depth-dependent re-scaling factor based on the numerical aperture, the refractive indices, and the wavelength. It is validated through wave-optics calculations and experimental data obtained using a measurement scheme for different numerical apertures and refractive index mismatch values. The depth-dependent axial scaling theory is used to correct high resolution 3D data, acquired under various refractive index mismatch conditions. This shows the importance of correcting axial distortions during fluorescence microscopy, which arise from refractive index mismatches when imaging into frozen-hydrated samples, and correcting these is crucial for accurate targeting, ensuring that regions of interest are precisely selected for milling.

Another critical challenge is obtaining reliable, real-time feedback on lamella thickness, uniformity, and quality during the milling process. Typically, scanning electron microscopes (SEMs) are used to assess lamella thickness, but this approach assumes the lamella consists of homogeneous material, which is often not the case for cellular samples. Moreover, many current methods require pre-calibration before each imaging session, adding to the complexity and limiting throughput. Chapter 4 presents a set of solutions to these challenges by introducing three complementary methods for determining lamella thickness during focused ion beam (FIB) milling: (i) the application of quantitative 4D-scanning transmission electron microscopy (q4STEM) to frozen-hydrated lamellae, benchmarked against energy filtered transmision electron microscopy (EFTEM); (ii) the estimation of lamella thickness using reflected light microcopy (RLM), which accounts for the milling geometry; and (iii) exploiting thin-film interference to create real-time, per-pixel thickness maps. Together, these techniques provide immediate feedback on the thickness, lateral uniformity, and condition of the protective Pt layer during the milling process. Integrating these innovations into the cryo-FIB workflow not only improves the precision and reliability of lamella preparation but also enhances the reproducibility and yield of high-quality lamellae. By providing real-time feedback on key parameters such as thickness, uniformity, and Pt layer integrity, our approach reduces the complexity of the process and makes it more accessible for routine use in high-resolution cryo-electron microscopy studies. The ability to target regions of interest based on fluorescence, combined with thickness and quality control, enables more efficient, automated workflows for cryo-ET sample preparation.

The work presented shows a comprehensive set of tools and techniques for improving the workflow of cryo-FIB lamella fabrication. By addressing critical challenges in thickness measurement, fluorescence-based targeting, and axial distortion correction, this work paves the way for more automated, high-throughput, and reliable processes in cryo-electron microscopy (EM) sample preparation. In Chapter 5 we review the prospects and implementation in structural biology and showcase two examples of using direct targeting from fluorescence imaging, as part of ongoing investigations in collaboration with the groups of Arjen Jakobi and Dimphna Meijer

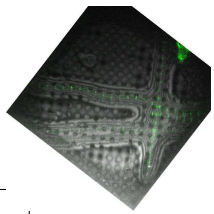

at the Kavli Institute of Nanoscience in Delft, concluding with an overview of further developments and possible improvements.

SAMENVATTING

Cryogene elektronen tomografie is een krachtige techniek om biologische structuren op moleculaire resolutie te onderzoeken, en is essentieel voor het begrijpen van complexe processen die binnenin cellen plaatsvinden. Deze vorm van tomografie onderscheidt zich van andere technieken doordat het mogelijk is om complexe structurele details waar te nemen, zonder de noodzaak van externe labels of markers. Het toepassen ervan wordt echter vaak beperkt door de uitdagingen in de voorbereiding van de biologische preparaten. Een belangrijkste stap is het maken van ultradunne, bevroren en gehydrateerde plakjes cel, ookwel lamellen genoemd, die idealiter een dikte hebben tussen 100 en 200 nm en daarmee onder de inelastische vrije weglengte van elektronen in ijs blijven. Het verkrijgen van dunne, artefactvrije plakjes is cruciaal voor de hoge resolutie beeldvorming.

Het maken van deze lamellen wordt gedaan met behulp van een gefocusseerde ionenbundel, waarmee er zorgvuldig cellulair materiaal verwijderd kan worden om zo een dwarsdoorsnede van de cel bloot te leggen, om deze vervolgens te kunnen bekijken in een transmissie elektronen microscoop. Het wegsnijden moet stapsgewijs en uiterst nauwkeurig gedaan worden. Ondanks verschillende verbeteringen van dit proces blijft het nauwkeurig uitsnijden van specifieke interessegebieden, met name in complexe biologische monsters, een grote uitdaging.

In de afgelopen jaren zijn diverse verbeteringen en verfijningen doorgevoerd in deze snij-workflows, waardoor doorvoersnelheid, betrouwbaarheid, opbrengst en kwaliteit zijn toegenomen. Hetgebruik van fluorescentie microscopie in de preparatie workflow heeft het selecteren en identificeren van interessegebieden makkelijker gemaakt. Het doel van dit proefschrift is om dit verder te ontwikkelen, door de fluorescentie microscoop te integreren in de opstelling met de gefocusseerde ionenbundel. Hierdoor is het mogelijk om *gelijktijdig* met het snijden te zien wat er gebeurd en kunnen er daarmee nieuwe inzichten verkregen worden in het snijproces en kunnen nieuwe toepassingen in de structurele biologie worden verkend.

Hoofdstuk 2 beschrijft de experimentele opstelling die is ontworpen en gebouwd om de bevroren lamellen te kunnen fabriceren met behulp van *in-situ* fluorescentiemicroscopie tijdens het snijden. Door een compacte cryogene koeler, een op maat gemaakte positionerings stage en een fluorescentiemicroscoop te integreren in een bestaande scanning elektronenmicroscoop uitgevoerd met een gefocusseerde ionenbundel, ontstaat er een drievoudige cryogene correlatieve microscoop die gebruik maakt van licht, elektronen en ionen. Hierdoor kan fluorescentiemicroscopie het bepalen van interessegebieden bij elke snijstap begeleiden, wat wordt bevestigd

door tomogram reconstructies uit de transmissie elektronenmicroscoop. Het vermogen om het monster tijdens en na het snijden te bekijken, vergroot de opbrengst en de efficiëntie van de lamel productie geschikt voor hoge resolutie beeldvorming.

Hoewel de integratie van fluorescentiemicroscopie in de opstelling helpt bij het sturen van het snijproces van specifieke cellen of subcellulaire regio's, leiden brekingsindex verschillen in fluorescentiemicroscopie tot registratiefouten en vervormingen. Dit bemoeilijkt de precieze lokalisatie van het interessegebied, en kan leiden tot een lagere kwaliteit lamel of zelfs het wegsnijden ervan. Om dit op te lossen, ontwikkelen we in Hoofdstuk 3 een diepte-afhankelijke, niet-lineaire schalingstheorie, die algemeen toepasbaar is binnen het vakgebied van de optische microscopie. Deze analytische theorie maakt het mogelijk om een diepte-afhankelijke herschalingsfactor te berekenen op basis van de numerieke apertuur, de brekingsindices en de golflengte van het gebruikte licht. De theorie wordt gevalideerd door middel van berekeningen en metingen, verkregen met een experimentele opstelling voor verschillende numerieke aperturen en brekingsindexverschillen. De diepte-afhankelijke axiale schalingstheorie wordt vervolgens toegepast om hoge-resolutie 3D-lichtmicroscopie data te corrigeren, die onder uiteenlopende brekingsindexmismatch-condities zijn verkregen. Dit laat zien dat het van belang is om axiale vervormingen in lichtmicroscopie te corrigeren, die ontstaan door brekingsindexverschillen in bevroren gehydrateerde lamellen. Het corrigeren hiervan is cruciaal voor een nauwkeurige lokalisatie, zodat het interessegebied exact kan worden uitgesneden.

Een andere uitdaging is het verkrijgen van betrouwbare, real-time feedback over de dikte, uniformiteit en kwaliteit van de lamellen tijdens het snijproces. Doorgaans worden scanning electronen microscopen gebruikt om de lameldikte te beoordelen, maar deze benadering gaat ervan uit dat de lamel uit homogeen materiaal bestaat, wat bij cellen vaak niet het geval is. Bovendien vereisen veel methoden een voorafgaande kalibratiestap, wat de complexiteit vergroot en de preparatiesnelheid beperkt. Hoofdstuk 4 presenteert een reeks oplossingen voor deze uitdagingen door drie complementaire methoden te introduceren voor het bepalen van de lameldikte tijdens snijden met een gefocusseerde ionenbundel: (i) de toepassing van q4STEM op bevroren en gehydrateerde lamellen, gevalideerd tegen energie gefilterede electronen tomografie; (ii) de schatting van de lameldikte met reflectie licht microscopie, waarbij gebruik gemaakt wordt van de ionenbundel snij geometrie; en (iii) het benutten van dunne-film interferentie om real-time een diktekaart van het lammel te genereren. Samen bieden deze technieken directe terugkoppeling op de dikte, laterale uniformiteit en de toestand van de beschermende platina laag tijdens het snijproces. Door dit te integreren in de snij workflow wordt niet alleen de precisie en betrouwbaarheid van lamelvoorbereiding verbeterd, maar ook de reproduceerbaarheid en opbrengst van hoogwaardige lamellen vergroot. Door real-time feedback te geven over kritische parameters zoals dikte, uniformiteit en de integriteit van de platina laag, vermindert onze aanpak de complexiteit van het proces en maakt deze het toegankelijker voor routinematig gebruik in cryo-elektronenmicroscopie met hoge resolutie. De mogelijkheid om interessegebieden te selecteren op basis van

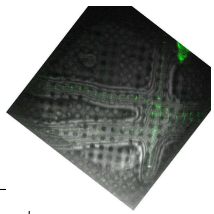

fluorescentie, in combinatie met dikte- en kwaliteitscontrole, maakt efficiëntere en meer geautomatiseerde workflows voor lammel preparatie mogelijk.

Het gepresenteerde werk biedt een uitgebreide set hulpmiddelen en technieken om de lammel preparatie workflow te verbeteren. Door uitdagingen aan te pakken op het gebied van diktemeting, fluorescentiegebaseerde doel bepaling en axiale vervormingscorrectie, kan dit werk leiden tot meer geautomatiseerde, snelle en betrouwbare processen in workflows voor lammel preparatie. In Hoofdstuk 5 bespreken we de vooruitzichten en implementatie binnen de structurele biologie en presenteren we twee voorbeelden van de directe bepaling van interessegebieden op basis van fluorescentie microscopie, als onderdeel van lopend onderzoek in samenwerking met de groepen van Arjen Jakobi en Dimphna Meijer aan het Kavli Institute of Nanoscience in Delft. We sluiten af met een overzicht van verdere ontwikkelingen en mogelijke verbeteringen.

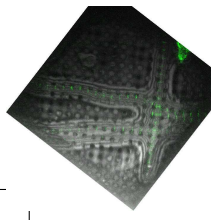

1 INTRODUCTION

The manipulation of light to magnify small objects has been around for centuries, and the advent of the first microscopes marked a significant milestone in the history of science. Studies of the microscopic world, conducted between 1665 and 1680 by Robert Hooke and Antoni van Leeuwenhoek, catalyzed a revolution in our understanding of biology. Together, they laid the groundwork for the field of microbiology, offering the first glimpses into the hidden world of microorganisms with observations of bacteria, protozoa, and sperm cells (Gest, 2004). As optical microscopy methodologies advanced, so did our comprehension of cellular biology, culminating in the formulation of cell theory during the 19th century (Ribatti, 2018). This progression paralleled the increasing need for enhanced visualization of cellular structures. The iterative cycle between instrumentation development and the pursuit of comprehending life at the minutest scales remains ongoing to this day.

EM has been, and continues to be, pivotal in this quest for understanding, as it remains the sole imaging method capable of discerning the intricate structural features within a cell. This is illustrated in the popular science book *Mr. Tompkins Inside Himself - Adventures in the New Biology* by George Gamow and Martynas Yčas, depicted in Figure 1.1a. Published in 1968, the book narrates Mr. Tompkins' exploration of the cellular architecture of his body during a dream journey, where the image shows how the insides of a cell could look, when sliced open and imaged using an electron microscope (Gamow et al., 1968). Given typical cell dimensions on the order of micrometers, the knife shown in this particular sketch is, of course, not true to scale.

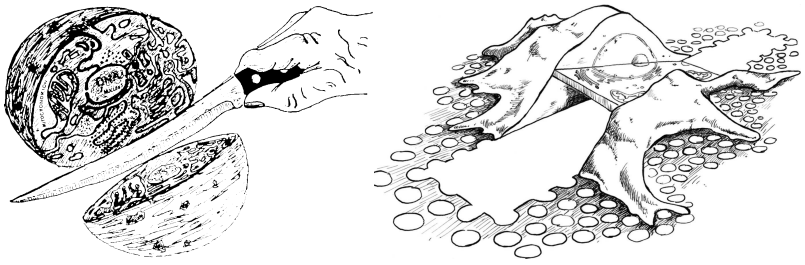

(a) (b)

Figure 1.1: Sectioning a cell. (a) A cell sliced open as illustrated in a 1968s popular science book (Gamow et al., 1968), and (b) the graphical abstract of a research article published 45 years later (Villa et al., 2013).

Fast-forwarding to 2013, where a focused beam of gallium ions has assumed the role of a microscopic scalpel, opening a window into the cell see Figure 1.1b (Rigort et al., 2012; Villa et al., 2013). A single cell is adsorbed onto a holey foil, and grazing incident ion bombardment has locally removed cellular material to unveil a cross-section of the cell's interior, priming it for high-resolution imaging with a TEM. While conceptually similar to the 1968 dream vision, there are many subtle differences in the practical realization, which are the results of significant technological developments in the past decades. Rather than inspecting a single cell from a living organism, the single adsorbed cell is obtained from a *culture of cells*, something which is only possible due to major developments in this field over the past 100 years (Jedrzejczak-Silicka, 2017). Furthermore, to image a cell at the highest possible resolution using an electron microscope, it needs to remain still, something which is obstructed by the cellular activity of living tissue. It can be affixed by an extremely rapid freezing process, causing the water within the cell to solidify into an amorphous (vitreous) state, thus preserving its biological structure (Dubochet et al., 1981). Finally, instead of imaging a cell cut in half inside a SEM, the thinly sliced section (lamella) is imaged by electron tomography using a TEM, which has required the field of electron microscopy to evolve since its conception in the 1930s (Gordon, 2014; Haguenau et al., 2003; Harris, 2015; Masters, 2009).

Resolving the specific three-dimensional structure of interacting proteins within the cellular context is imperative to advance disease understanding (Dalle-Donne et al., 2006; Ganten et al., 2006). Ideally, a specific protein of a few nanometers in diameter (akin to finding a needle) would be targeted within the volume of a cell ($\sim 1000\,\mu m^3$, similar to a haystack) and once found, subsequently fabricate a section encompassing it. Unfortunately, neither the FIB nor the SEM, provides a contrast mechanism for biomolecular composition, potentially leading to indiscriminate removal of material and inadvertent ablation of the protein of interest. Combining a FIB and SEM with FM is a potential solution to this challenge, as FM enables the visualization of specific parts of tissue, cells, individual organelles, and/or macromolecular assemblies within a cell through the use of fluorescent labeling. These techniques are discussed individually below before discussing the state of the art and how this work pushes the boundaries.

1.1 FLUORESCENCE MICROSCOPY

Fluorescence is a process where incident (excitation) light is absorbed by a substance, followed by the subsequent emission at a different wavelength. In general, the emitted light has a longer wavelength (lower energy), than the absorbed light, a process called Stokes shift. The first fluorescent microscopes were conceived in the early 1900s, and have evolved to allow targeted live cell imaging through the development of fluorescent stains (1930s), fluorescent-labelled antibodies (1940s), green fluorescent proteins (GFP, 1960s), their subsequent development as genetic tags (1990s) and novel fluorescent markers in recent years (Chalfie et al., 1994; Dunst

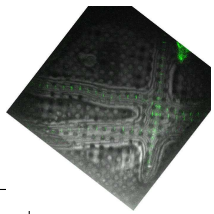

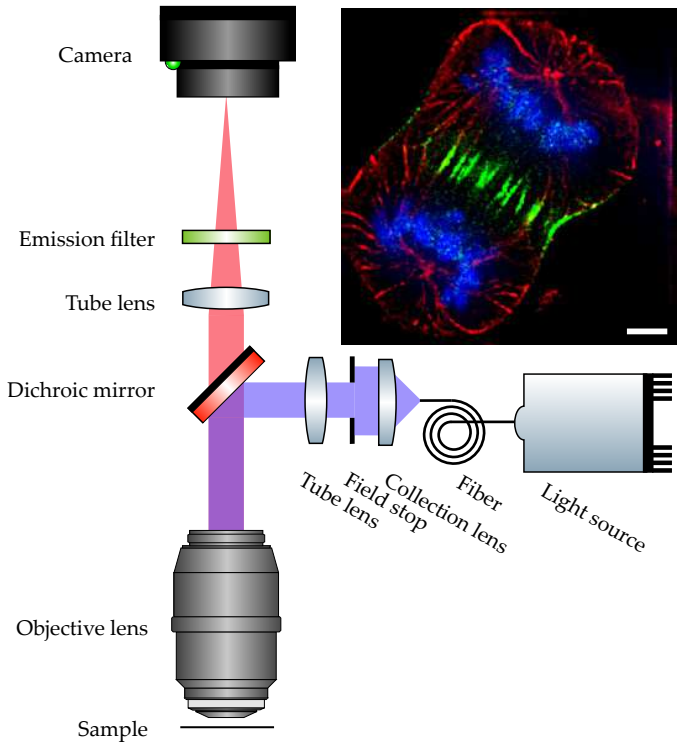

Figure 1.2: Schematic layout of an epi-fluorescence microscope. On the right an example fluorescence microscopy image showing an overlay of three components in a dividing human cancer cell. DNA is stained blue, a protein called INCENP is green, and the microtubules are red. Scale bar 10 µm, image from (Wikimedia, 2010).

et al., 2019; Hickey et al., 2021; Prasher et al., 1992; Renz, 2013). By labeling various biomolecules within a cell using distinct fluorescent markers, one can capture multicolor fluorescence images that provide insight regarding the presence and spatial arrangement of the labeled biological molecules or entities.

A FM setup functions by separating the excitation and emission paths using a dichroic mirror, as shown in Figure 1.2. An epifluorescence configuration is shown, where both excitation and emission light travel through the same objective lens (OL). In the emission arm, different distinct narrow bandpass emission filters assure that only light emitted from the fluorophore is imaged onto the camera. By omitting an emission filter it is generally possible to perform RLM, as (i) the spectral alignment between the the light source and the dichroic mirror is never perfect, and (ii) the camera sensors are designed to be extremely sensitive. In many modern FM setups, the optical objective lens is designed such that the imaging distance is set to infinity,

which allows for optical accessories to be placed into the light path. A tube lens (TL) is used to ensure that an image plane is created on the camera sensor.

In the excitation arm, light from a multicolor fiber-coupled light source is collected by a collection lens and, in conjunction with a field lens, is focused into the exit pupil of the OL. A field stop positioned between the collection and field lenses ensures that the illuminated area on the sample is matched with the area imaged by the camera sensor.

A critical parameter is the numerical aperture (NA), which is a dimensionless number that characterizes the range of angles over which the system can accept or emit light, and is defined as

$$\mathrm{NA} = n_1 \sin(\theta), \tag{1.1}$$

where n_1 is the refractive index of the immersion medium, and θ is the half-angle of the maximum cone of light that can enter or exit the lens. A higher NA allows for more light to be collected and thus resolve refined details as the attainable resolution d is given by

$$d = \frac{\lambda}{2\mathrm{NA}}, \tag{1.2}$$

where λ is the wavelength of light.

The strength of fluorescent microscopy is that it can resolve, for instance, spatial arrangement between two differently labeled biological molecules (see inset Figure 1.2). At the same time, this is also a weakness as the relation to, and the structure of *unlabelled* material remains invisible. In a way, the inverse holds true for electron microscopy, where an entire cell can be imaged with a high level of structural detail, but information on the type of biological molecules present is lacking.

1.2 ELECTRON MICROSCOPY

In contrast to visible light, electrons are able to resolve nanometer sized features when used for imaging, and the use of electrons to visualize a specimen at intricate levels of details is extremely broad. A SEM utilizes a focused beam of electrons to raster the surface point by point, while collecting back scattered (BSE) or secondary electron (SE) signals, generated by the specimen-beam interaction. This produces a high-resolution image with the contrast determined by material composition, (local) conductivity, surface morphology, electron signal recorded, acceleration voltage of the incident electrons, and more factors.

Secondary electron generation is an inelastic process, whereas back scattering is an elastic process. Both have a different scattering cross sections associated with them, describing the interaction probability between the incident electron beam and the specimen. The probability for elastic scattering is approximately proportional the atomic number squared, Z^2, while the inelastic scattering probability does not have such direct relation (Hawkes et al., 2007). Secondary electrons are characterized as

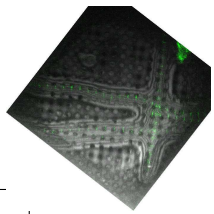

having energies less than 50 eV. This makes that only SEs near the specimen surface can escape and as such, the contrast is mostly dominated by sample topography (see for instance see Figure 1.3a). Over 95 % of an organisms weight is composed of H, C, N and O, having respectively $Z = 1,\ 6,\ 7$ and 8 (Alberts et al., 2002). As such, BSEs do not provide sufficient contrast without additional sample preparation, for instance staining the specimen with heavy metals like osmium, uranyl and lead. Depending on the procedure, specific biomolecular compounds will bind the high Z metals, and thus provide good contrast in the SEM.

Transmission electron microscopy

The maximum resolution obtained in an SEM depends on multiple factors, such as the electron beam spot size and interaction volume of the electron beam with the sample. Currently, the lower resolution limit lies around 1 nm, while the electron wavelength λ_{el} used is approximately 6.98 pm (at an kinetic energy K of 30 keV), as given by

$$\lambda_{\text{el}} = \frac{hc}{\sqrt{K^2 + 2Km_{\text{e}}c^2}}. \tag{1.3}$$

Here, h is Planck's constant, c is the speed of light, and m_{e} the rest mass of the electron. To further study macromolecules such as membrane proteins, protein-DNA complexes, and nucleic acid structures at ultra-high resolution, a TEM with a broad beam illumination scheme is used.

In a TEM, electrons pass through a thin specimen, where local phase differences in the exit electron wave after transmission through the sample are converted to intensity contrast to form an image providing detailed views of internal structures, see Figure 1.3b as an example. An operation voltage of 100 to 300 kV is used to reduce inelastic scattering limiting charging effects, and retaining spatial coherence as electrons transit the specimen (Dickerson et al., 2022; Herzik Jr et al., 2017). Although the electron wavelength in a TEM lies well below a nanometer, the attainable resolution is determined by aberrations and not diffraction contrary to visible light. Consequently, the realization of aberration corrected imaging paved the way to resolve structures at atomic resolution. Developments to do this for purified biological structures, have been ongoing since 50 years and is called single particle analysis (SPA), where the three-dimensional structure is reconstructed by computationally extracting the individual particles from high resolution images (Frank, 2015).

1.3 CRYOGENIC ELECTRON TOMOGRAPHY

Obtaining three-dimensional structures through SPA is only possible if highly purified and monodisperse macromolecules are imaged, computationally extracted, aligned and averaged, see Figure 1.3c. It is crucial that the macromolecules do not move during image acquisition. To this end, the purified samples are frozen in a thin

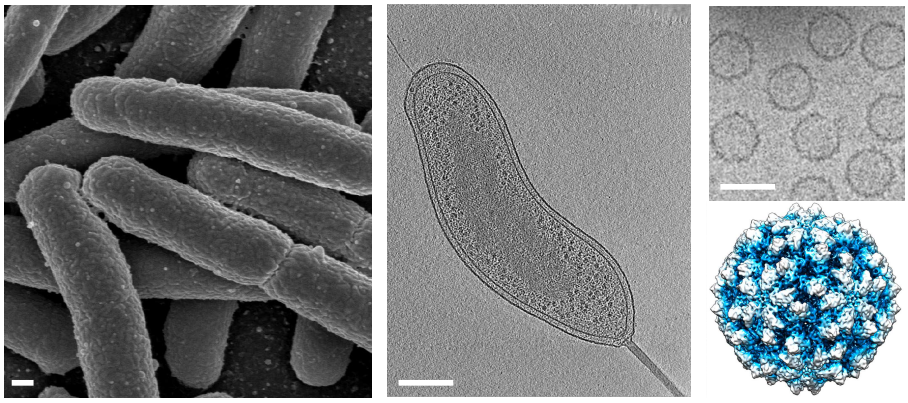

(a) (b) (c)

Figure 1.3: Different examples of electron microscope images. In (a), a scanning electron micrograph of bacteria where predominantly surface morphology is visible (Wikimedia, 2002), whereas in (b) is a bacteria as imaged with an transmission electron microscope, where electron travel through, and the internal structure can be visualized (Wikimedia, 2015).Finally in (c) a transmission electron micrograph of vitrified virions (top), where through isolating, averaging and computation a three-dimensional reconstruction of the virions can be made (bottom) (Wikimedia, 2018).Scale bars: (a) - 200 nm, (b) - 200 nm and (c) - 50 nm.

layer of amorphous (vitreous) ice. This can be achieved through *plunge freezing*, a process where the watery specimen is rapidly submerged into a cryogen such as a liquid ethane/propane mixture (about −188 °C). The use of this mixture allows for freezing rates of >100 000 °C/s due to the relatively high thermal conductivity and specific heat, compared to liquid nitrogen. In doing so, the water will solidify as an amorphous solid and will not have a chance to crystallize, thereby also keeping the biological structure intact (Dubochet et al., 1981).

Although it is possible to study macromolecular structures in high detail, the downside of SPA is that the cellular context is missing. This has been the main driving force behind developing cryo-ET on sections (lamellae) cut from frozen hydrated cells. Tomography is a well established technique, in which the sample is rotated whilst recording different views of the same area. By backprojecting these different views, the three-dimensional structure residing in the lamella, can be resolved. To attain high resolution, the lamella must be thinner than the inelastic mean-free path of electrons in water ice. This typically requires a thickness of approximately 100 to 200 nm (Vulović et al., 2013), and can be prepared using a focused ion beam (FIB).

FIB fabrication of lamellae

A focused beam of ions can also be scanned over the sample surface while measuring back scattered or secondary electron signals. Different species of ions can be used in dual beam systems, also known as a focused ion beam scanning electron microscope (FIB-SEM), though within the scope of this thesis, mostly gallium ions have been used.

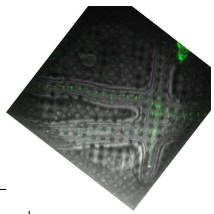

Although images can be acquired with the FIB, the use of an accelerated beam of ions also induces sputtering, a process where the impinging ions eject particles from the sample (Utke et al., 2008). As the amount of ejected material scales with the incident ion current, it is possible to acquire images at relatively low currents of 1 to 80 pA, whereas sputtering, or milling is often done at $\gg$80 pA.

FIB fabrication of lamellae has its roots in materials science. Early experiments demonstrated that this technique could also be successfully applied to frozen biological samples under cryogenic conditions, avoiding devitrification (Basgall et al., 2006; Hayles et al., 2007; Marko, Hsieh, et al., 2006; Marko, CE Hsieh, et al., 2006; Michael Marko et al., 2007). In recent years cryo-ET imaging on frozen hydrated lamellae, fabricated with a FIB, has been used to successfully study the molecular environment of the cell (Hagen et al., 2015; Mahamid et al., 2016). It is emerging as a powerful imaging technique in structural biology research, although the sample preparation workflow is fraught with challenges and difficulties (Berger et al., 2023).

1.4 CHALLENGES IN THE SAMPLE PREPARATION WORKFLOW FOR CRYO-ET

Preparing lamellae for high resolution imaging is a many step process starting at the cell culture. In many of the preparation steps prior to loading the specimen into the TEM, one needs to consider; correct EM grid preparation, cell density & distribution, the possible use of cryo-protectants, plunge freezing consistency, EM grid clipping, parasitic ice contamination, vitrification uniformity or partial recrystallization. A selection of these, specific to FIB prepared lamellae, are discussed in more detail below:

CAPTURING THE REGION OF INTEREST Given that lamellae have a local thickness of 50 to 300 nm while cells are typically micrometer-sized, only a small fraction of the total cellular volume is captured in a prepared lamella. Therefore, macromolecules, cellular structures, and interactions of interest that are not uniformly and abundantly distributed throughout the cell may have a low likelihood of being included within the prepared lamella.

LAMELLA THICKNESS The lamella thickness should be approximately 100 to 200 nm, and uniform to allow for high-quality imaging and accurate tomography. Biological samples are often heterogeneous in density and composition, making it challenging to mill uniformly and avoid preferential thinning.

ICE CONTAMINATION AND RE-CRYSTALLIZATION From the moment cells are plunge frozen, they need to remain well below approximately $-135\,^{\circ}\mathrm{C}$, as this is the transition temperature from vitreous to crystalline water ice (Dowell et al., 1960; Dubochet et al., 1981). At the same time, an amorphous ice layer can easily grow from water molecules residing the the vacuum rest gas. This ice layer decreases the contrast of the TEM image, lowers data quality, and limits the downstream achievable resolution.

Although careful preparation of lamellae is crucial for obtaining high-resolution imaging in TEM, combining fabrication through charged particles with visualization of biological function can be achieved through correlative techniques, such as correlative light and electron microscopy (CLEM), which integrate light and electron microscopy techniques.

1.5 STATE OF THE ART IN CORRELATIVE LIGHT AND ELECTRON MICROSCOPY

An image acquired with fluorescence microscopy typically contains a large fraction of low-intensity regions, leaving most of the specimen in the dark, as only specific parts of the sample (or cell) are fluorescently labeled and emit light, and from this *biological function* can be inferred. The SEM or TEM can acquire high-resolution imagery containing *structural* information. Combining these two image modalities into a single overlaid image, readily provides the biological function placed within the ultra-structural context, known as CLEM. With their different contrast mechanisms, creating an overlay can be challenging if the specimen is transferred between two separate (light and electron) microscopes, but can be overcome through integration, for which microscopy systems have been developed in the past decade. These solutions have however predominantly targeted room temperature, resin embedding type, applications. (De Boer et al., 2015; Timmermans et al., 2015; Zonnevylle et al., 2013).

As the advantages afforded in directly using biological information to determine the milling site outweigh the challenges, different methods have been developed for fluorescence targeted FIB milling. In 2016, Arnold et al. used monosized ferromagnetic polystyrene beads as fiducial markers in preparing frozen hydrated lamellae. The iron oxide in the magnetic beads is detectable in the FIB by the back-scattered electron detector and the polystyrene is autofluorescent when excited by green light in the FM (Arnold et al., 2016). Fluorescent imaging was performed using a standalone confocal microscope. After transferring the sample into the FIB-SEM, correlation was achieved through a 3D coordinate transformation.

The first *in-situ* optical microscope in a cryo-FIB-SEM was presented in 2019, simplifying sample handling and reducing the risk of sample contamination by limiting the number of cryo-transfer steps. The use of fluorescent data for *direct targeting* is still limited as in these systems the sample still had to be shuttled between FM and FIB-SEM modalities thus requiring repositioning of the sample inside the vacuum chamber (Gorelick et al., 2019). Since its introduction, the *in-situ* concept has been commercialized by different companies, with slightly different geometries (Smeets et al., 2021; ThermoFisher Scientific, 2021).

The utilization of biological information in the form of FM data for the purpose of precise, accurate and thus targeted FIB milling has so far been limited by stage repositioning and/or coordinate transformation errors. The concept of an integrated, coincident three-beam solution enabling *directed, and targeted* FIB milling through the use of FM, constitutes the primary focus of this thesis, and is discussed in full

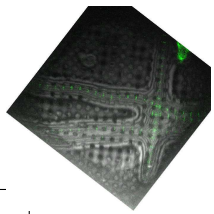

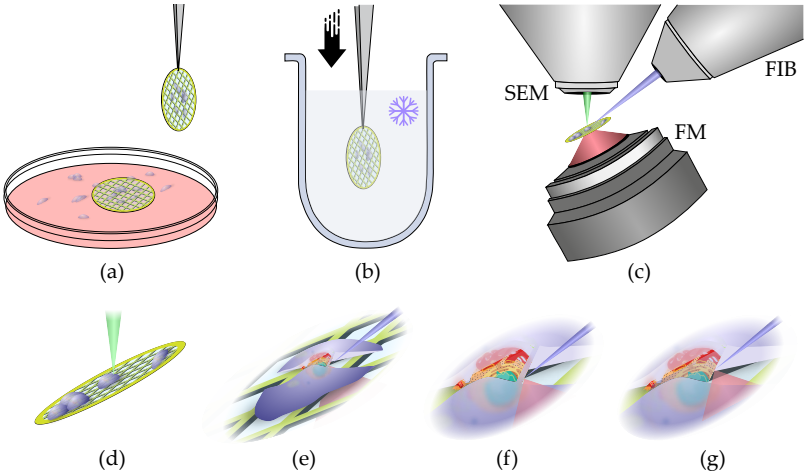

Figure 1.4: Schematic of the envisioned lamella fabrication workflow. (a) Cells (blue blobs) are cultured on electron microscopy grids (yellow mesh), inside a petridish containing liquid medium (pink). (b) The grid with cells adhered, is picked up with tweezers (gray) and rapidly submerged into a liquid ethane cryogen ($T = -188\,°C$, shaded blue). (c) The plunge frozen grid with cells is loaded into the three-beam coincident microscope, where SEM, FIB, and FM imaging modalities are aligned to the same point. (d) Using an overview image acquired in the SEM, possible cell targets are identified, and each is subsequently imaged in the FM to find the region of interest (ROI). (e) Using the FIB, material above and below the target is ablated to create the lamella. (f) The lamella is thinned with the FIB, while monitoring the state in the light microscope, until an approximate lamella thickness of 200 nm is reached, as shown in (g).

technical detail in Chapter 2. The conceptual workflow is illustrated in Figure 1.4, where cells are cultured inside a petri dish containing electron microscopy grids (extremely fine metal mesh). To be able and pinpoint the biology of interest, these cells are typically modified to express fluorescence. The cells also adhere to the grid, and with cell density high enough, a grid can be picked up from the petri dish and flash frozen through rapidly submerging it into a cryogen. The grid containing frozen cells is then loaded into the three-beam microscope and a low magnification overview image is acquired with the electron beam. Potential (isolated) target cells are identified and subsequently imaged with the fluorescence microscope. After setting the ROI, the focused ion beam is used to ablate material and create an initial section, also called lamella. Finally, this lamella is thinned down with the FIB, whilst continuous monitoring through the light microscope (Figure 1.4f and g).

With the specimen held in vacuum and at cryogenic temperatures, a dry objective lens is needed to image into frozen cells. This induces a refractive index mismatch (RIM) between the objective lens ($n_1 = 1.0$) and specimen ($n_2 = 1.28$ at $T = 109\,K$), inherently leading to axial scaling of the microscope coordinate system, and the intricacies of this effect are discussed in Chapter 3 (Kofman et al., 2019; Loginov et al., 2024; Pawley, 2006).

Chapter 4 extends the use of the light microscope beyond detecting fluorescence. By collecting pseudo monochromatic light, reflected from the specimen, the thickness of the lamella can be determined from thin film interference effects. In addition, the lamella thickness can also be estimated by recording the radial scattering profile from a 30 keV incident electron beam (Skoupỳ et al., 2023), where the scattered profile is imaged by adding a scintillator between the specimen and objective lens. With the intracellular structures sensitive to damage from the FIB, a protective layer containing platinum is usually applied prior to ion beam milling. The thickness and uniformity of this platinum rich layer can also be assessed in the RLM. The prospects and outlook for structural biology, along with preliminary results from two studies are presented in Chapter 5, and the conclusion from this work can be found in Chapter 6.

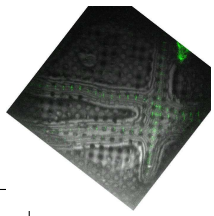

2

A CRYOGENIC, COINCIDENT FLUORESCENCE, ELECTRON, AND ION BEAM MICROSCOPE

To prepare a thin sample from a frozen-hydrated cell for cryogenic electron tomography, focused ion beam micromachining is employed. Conventional methods for preparing these samples lack precision in targeting specific structures or proteins. Fluorescence-guided focused ion beam milling can target precise locations but requires multiple sample transfers, increasing the risk of contamination and reducing accuracy in three-dimensional targeting. In this chapter, a method to fabricate frozen-hydrated lamellae using *in-situ* fluorescence microscopy to guide the milling, is presented. The approach involves retrofitting a compact cryogenic microcooler, a custom positioning stage, and an inverted widefield fluorescence microscope onto an existing focused ion beam scanning electron microscope, creating a coincident three-beam cryogenic correlative microscope. This setup allows for fluorescence microscopy-guided targeting at each milling step, verified by transmission electron microscope tomogram reconstructions. The ability to monitor the sample during and after milling enhances the success rate and increases the efficiency of producing lamellae suitable for high-resolution imaging.

2.1 INTRODUCTION

High-resolution 3D reconstructions of biological macromolecules in their near-native cellular environment are necessary to obtain a mechanistic understanding of complex, biological processes at the molecular scale. Cryo-ET allows imaging cellular structures at unprecedented resolution and clarity (Tegunov et al., 2021; Zimmerli et al., 2021). In cryo-ET, a sample is flash cooled, thinned to the appropriate thickness, and a tilt series of projections is acquired using a TEM (Koning et al., 2018; Turk et al., 2020). A prerequisite for high-resolution cryo-ET is that the sample is thinner than the inelastic mean-free-path of electrons in vitreous water ice—in practice, this means a sample thickness of approximately 100 to 200 nm (Vulović et al., 2013). To create sufficiently thin sections (lamellae) for high-resolution tomography, the use of a FIB-SEM has proven to be most successful in ablating the excess cellular material surrounding the region of interest (Chiang et al., 2007; Hylton et al., 2021; Villa et al., 2013). In recent years, various improvements and refinements have been made to the cryo-FIB milling workflow improving throughput, reliability, sample yield, and quality (Buckley et al., 2020; Schaffer et al., 2019; Tacke et al., 2021; Wolff, Limpens, et al., 2019).

This chapter has been published as: Boltje et al. (2022). "A cryogenic, coincident fluorescence, electron, and ion beam microscope." In: eLife 11, e82891.

Identification of the ROI for milling in the right location is a crucial step. Unfortunately, neither the SEM nor the FIB provides a contrast mechanism for biomolecular composition, leading to blind milling and possibly inadvertent ablation of the structure of interest. Cryogenic correlative light and electron microscopy (cryo-CLEM) can be employed to overcome this challenge. In this approach, the location of specific objects or cellular compartments is targeted for cryo-FIB milling using specific fluorescent labeling, thus allowing targeted FIB milling.

The first use of cryo-CLEM for fluorescence targeted FIB milling employed monosized ferromagnetic polystyrene beads as fiducial markers for FM and FIB-SEM correlation (Arnold et al., 2016). The signal from the iron oxide in the magnetic beads is detectable in the FIB-SEM by the back-scattered electron detector and the polystyrene is auto-fluorescent when excited by green light in the FM. FM imaging for target localisation was done in a stand-alone cryogenic spinning disk confocal microscope after which the sample was transferred to the FIB-SEM. Correlation was achieved by 3D coordinate transformation and a correlation accuracy on the order of tens of nanometer was shown. However, the error range remained relatively large, ranging from 0.2 to 1 µm depending on the number of fiducial markers used in the correlation. Arnold *et al.* estimated a success rate of 60 % when milling site-specific lamellas of 200 to 300 nm thick which would drop when aiming for a thickness of 100 to 200 nm.

More recently, Gorelick et al. (2019) equipped a FIB-SEM with an *in-situ* FM, simplifying sample handling and reducing the risk of sample contamination by limiting the number of cryo-transfer steps. Switching between FM and FIB-SEM imaging modalities required repositioning of the sample inside the vacuum chamber. The 2D positional error made in milling based on FM data is mostly determined by the relocation precision of the sample stage and was reported to be in the range of <420 nm along X and <220 nm along Y. These relatively large relocation errors prevented high enough localization accuracy to mill a lamella required for high-resolution tomograms, in a targeted fashion.

Coincident imaging with all three microscopes could mitigate the need for fiducial markers and the occurrence of relocation errors, thereby facilitating the application of cryo-CLEM for the cryo-ET workflow. Such a geometry would also allow FM imaging while milling, allowing real-time correction of the milling process in the case of errors, drift, or other misalignments.

Here, we present a coincident 3-beam cryo-CLEM solution, by mounting a tilted light objective lens inside the vacuum chamber such that widefield FM imaging can be done whilst FIB milling. The light microscope is combined with a compact cryogenic microcooler and a custom positioning stage. Our system can be integrated with existing dual beam systems to allow simultaneous, coincident imaging with both FM, SEM and FIB for *in-situ* FM-guided fabrication of frozen-hydrated lamellae.

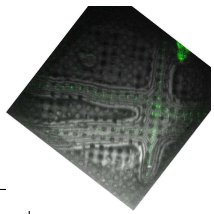

2.2 SYSTEM OVERVIEW

A principal design element of our microscope is the placement of the OL of the fluorescence microscope directly below the sample (Zonnevylle et al., 2013). This minimizes interference with the EM hardware residing in the upper half space of the EM and offers the following advantages (Figure 2.1): (i) the OL focal point can be aligned to the FIB-SEM working point, allowing simultaneous and coincident imaging with electron-, ion- and photon beams. (ii) *in-situ* FM-guided FIB milling of frozen hydrated lamella without any stage moves can be conducted. (iii) Quality control of the lamella fabrication process can be performed with the light microscopy (LM) at every step in the milling process. (iv) Multiple ROIs on the sample can be processed, by centring and focusing the fluorescent ROI in the LM image after a single, initial OL alignment. (v) An OL with a relatively high NA can be used, in our case an NA of 0.85, allowing high resolution fluorescence localization.

Vitrified cellular samples on TEM AutoGrids (Rigort et al., 2012) are positioned in between the objective lenses of all three microscopes. The AutoGrids are located on top of a thin indium tin oxide (ITO)-coated coverglass that serves as a beam stop to prevent exposure of the OL to electrons or ions. A cryogenic microcooler is used to keep the sample vitrified without the need to cool any of the microscope components, thus retaining unmodified imaging modalities of all three beams. The FM objective lens and microcooler can be moved about in the vacuum by custom piezo positioning stages. A sample shuttle transfer is implemented via a modified PP3006 transfer solution from Quorum Technologies (Quorum Technologies Ltd, 2021). The optical microscope hardware resides on a high vacuum (HV) door replacing the original door of the microscope, and it current design fits on a Thermo Fisher Scientific (TFS) SDB chamber. By adapting the design of the door, it will be compatible with dual beam systems retaining 52 degrees between SEM (top) and FIB (side) from other manufacturers. The piezo stages, microcooler, optical microscope and interface to the host system are controlled using the open-source acquisition software Odemis (Delmic B.V.) (Piel et al., 2022). In the following sections we will discuss the optical microscope, cryogenic sample holder and positioning stage in more detail.

2.3 OPTICAL MICROSCOPE

To allow optical inspection when the sample is in position for FIB milling at 10° angle of incidence, the OL is in a tilted position to retain perpendicular incidence to the sample surface (Figure 2.2). It resides in the HV chamber, along with the folding mirrors. All other optical components are mounted inside the optical module at ambient conditions and are separated by an optical vacuum window.

As the sample is held at cryogenic temperature, a relatively long working distance (WD) objective lens is required. We selected a Nikon CFI L Plan EPI 100xCRA objective lens (Nikon #MUE35900, 100×) for its intermittent NA of 0.85 and working distance

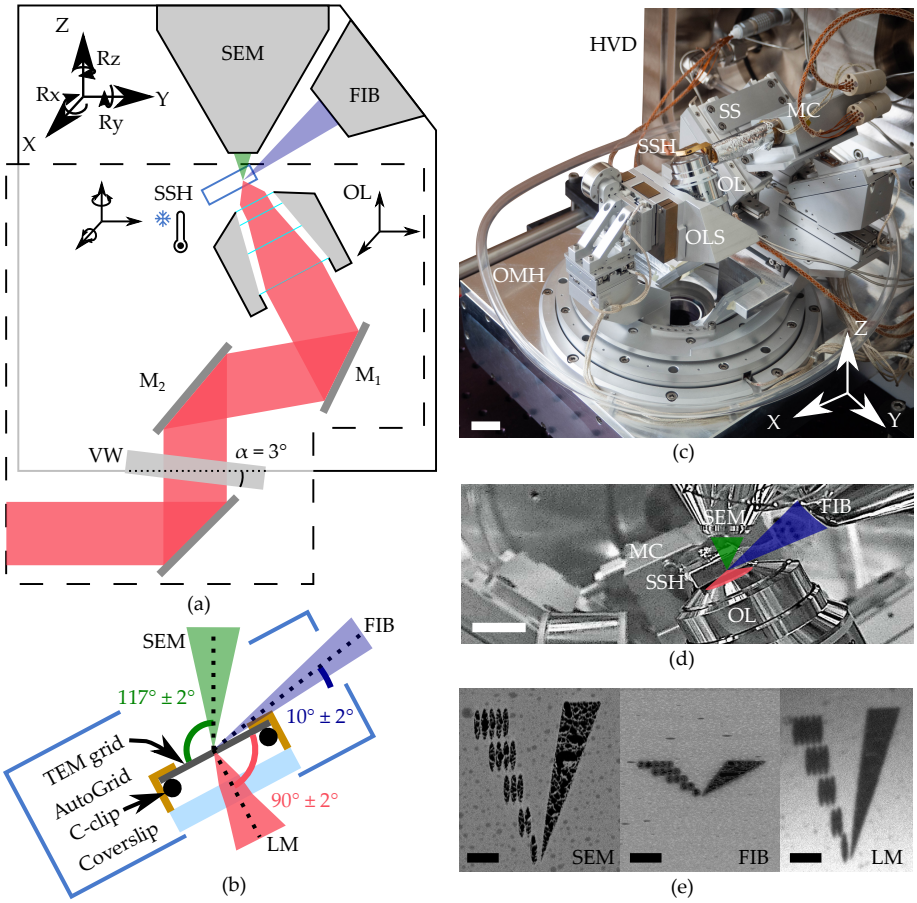

Figure 2.1: Cryogenic, coincident fluorescence, electron and ion beam microscope. (a) Schematic illustration showing the retrofitted hardware (dashed box) separated from the FIB-SEM hardware in respectively the lower and upper half-spaces of the microscope. (b) Schematic illustration of the sample shuttle holder (SSH) with the TEM grid (sample) clipped into an AutoGrid placed on top of the coverslip. The coincident point is formed by the electron-, ion- and light beams. Incident angles indicated are limited by the FIB access hole in the sample shuttle holder. (c) Photograph of the setup showing the HV door (HVD), optical module housing (OMH) on which the sample positioning stage (SS), objective lens stage (OLS), objective lens (OL) and microcooler (MC) are mounted. Scale bar 2 cm. (d) Infrared photograph acquired with the charge-coupled device (CCD) camera mounted on the FIB-SEM host system showing the microcooler and objective lens mounted inside the HV chamber. Scale bar 10 mm. (e) Images of an alignment pattern in the three imaging modalities, the light microscopy image is acquired by collecting reflected light from the sample. The alignment pattern is milled in the TEM grid coating using the FIB. Scale bar 3.5 µm.

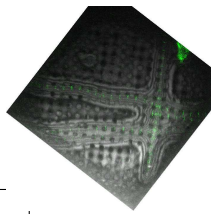

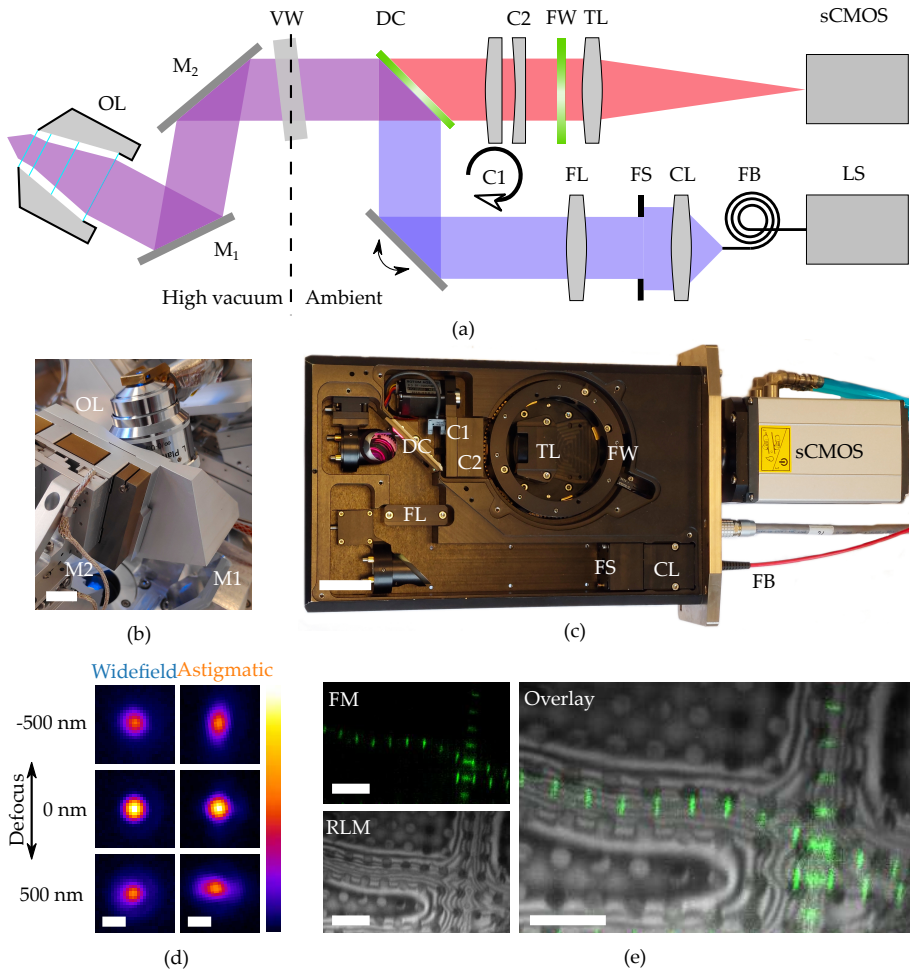

Figure 2.2: High-resolution fluorescence and reflected light microscopy allows to overlay fluorescence markers on sample structural layout. (a) schematic illustration showing the layout of the epi-fluorescence microscope. $M1$ and $M2$ form a folding mirror residing in high vacuum together with the objective lens (OL). The vacuum window (VW) separates the high vacuum from ambient conditions. Excitation and emission paths are separated by the dichroic mirror (DC). Two cylindrical lenses ($C1$ and $C2$) are placed in the emission path to allow for astigmatic point spread function shaping. Emission filters are mounted in the filter wheel (FW), and the tube lens (TL) focuses the image on the camera (sCMOS). The light source (LS) is coupled by a fiber (FB) to the optical module. Light emitted from the fiber is collected by the collector lens (CL), clipped by the field stop (FS) and imaged into the OL object plane by the field lens (FS). (a) Optical objective lens mounted on 3DOF stage along with $M1$ and $M2$. Scale bar 1 cm. (b) Annotated photograph showing the optical module. Scale bar 4 cm. (c) XY slices from point spread functions of the optical microscope, at different levels of defocus, both in case of wide field imaging and with induced astigmatic shaping. The point spread functions have been obtained by imaging and averaging individual fluorescent beads ($T_{sh} = 300\,\text{K}$, $N = 20$, $\lambda = 520\,\text{nm}$). Scale bars 0.5 µm. (d) Imaging modalities of the optical microscope. Left top: fluorescence microscopy (FM) image of drosophila myofibrils where Sls(700) is tagged with Alexa Fluor 488. Left bottom: reflected light microcopy (RLM) image of the same area as the FM image. Right: Overlay of the FM and RLM images. The circular pattern originates from the Quantifoil R 2/2 film and interference fringes are visible along the radial direction of the myofibrils due to the changing thickness. Scale bars 8 µm.

ranging between 0.85 to 1.2 mm depending on correction collar setting (0 to 0.7 mm). In our specific case (coverslip #1.5H, 0.170(5) mm thick) the WD is approximately 1 mm. Residual gas analysis with the OL in a separate vacuum setup did not show any foreign species due to the addition of the OL and we did not observe the imaging performance to deteriorate after repetitively pumping and flushing.

In addition to four fluorescence channels, the setup also allows for imaging with RLM by collecting light reflected by the sample from either of the excitation channels through an additional pass-through hole in the filter wheel. Overlaying the FM and RLM images facilitates targeted milling by combining fluorescence signal with contextual information Figure 2.2e.

Astigmatic point spread function (PSF) shaping is implemented by inserting two obliquely crossed cylindrical lenses, in the form of a Stokes variable power cross-cylinder lens set, in the detection path (Stokes, 1849; Thompson, 1899). One of the two lenses is mounted in a rotational mount, actuated by a stepper motor, and is used to switch between astigmatic and regular wide field imaging.

To validate the performance of the optical microscope, we recorded point spread functions at cryogenic conditions by imaging and averaging fluorescent beads (sample temperature 300 K, $N = 20$, $\lambda = 520$ nm). The full width half maximum (FWHM) of the widefield PSF is 370 and 1000 nm for the XY and Z directions respectively. The astigmatic PSF is recorded by setting $\theta = 92°$, which leads to an astigmatic deformation in the PSF, Figure 2.2d.

2.4 CRYOGENIC SAMPLE HOLDER

Conventional cryogenic FIB-SEM systems often use a cold-gas cooled sample holder consisting of a solid block of copper with positioning stage mechanics below it, which is incompatible with our design for the optical microscope. Our cryogenic sample holder (Figure 2.3) needs to: (i) keep the sample vitrified, (ii) allow the sample to be imaged from three sides simultaneously by SEM, FIB and LM, (iii) accept TEM grids clipped in AutoGrid cartridges, (iv) keep drift and vibration levels at a minimum and (v) shield the sample from contamination as much as possible. We opted for a cold-finger design where the central feature is a customized Joule-Thomson (JT) cryogenic microcooler optimized for its low vibrations, drift and small footprint (DEMCON kryoz), (DEMCON-kryoz, 2021; Lerou et al., 2008). The cooling mechanism is based on high pressure gas undergoing JT expansion through a restriction, producing a maximum net cooling power of ~200 mW. The cold stage consists of three layers of patterned borosilicate glass (D263T) housed in a titanium tube, and is braided to a cold finger. The 0.1 mm thick titanium tube provides adequate thermal isolation from the bigger aluminium body containing incoming gas lines, electrical wiring and a vacuum connection. The housing is leak tight and differentially pumped by the FIB-SEM vacuum system through a fluoropolymer tube.

This compact cooling solution provides local cooling to the sample. We found that it requires approximately two hours to reach <108 K and the cooler can keep the

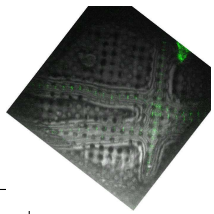

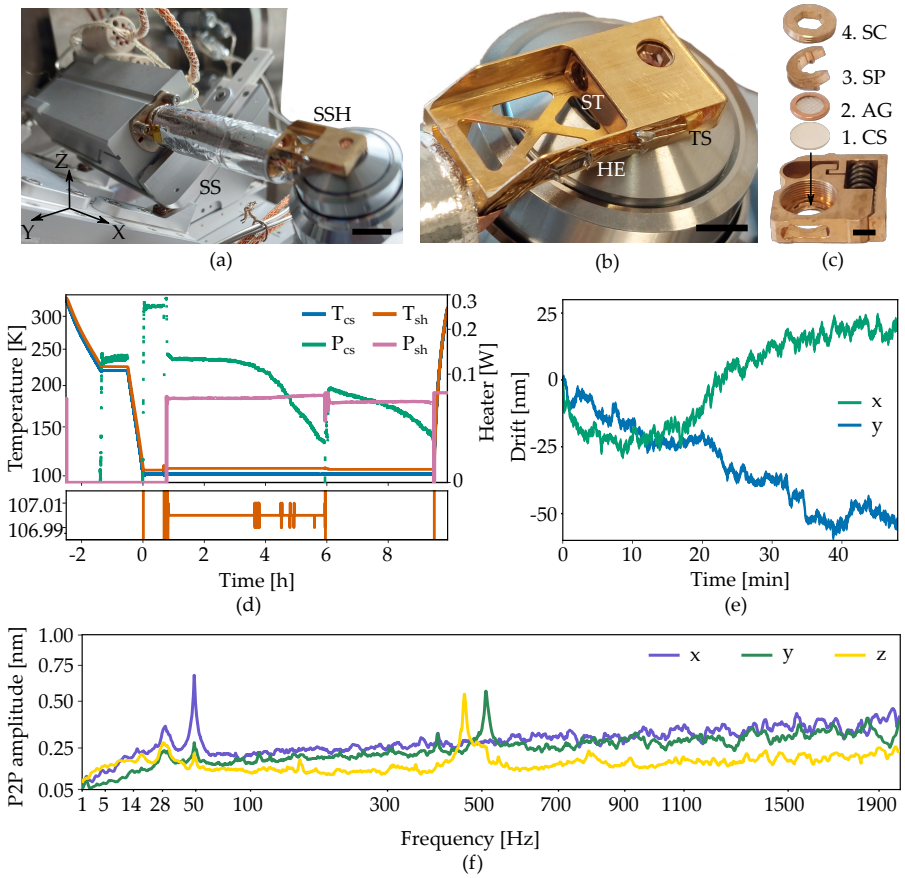

Figure 2.3: Cryogenic microcooler design and performance. Photographs of (a) the microcooler mounted on the sample positioning stage (SS), (b) the sample shuttle holder (SSH) in detail and (c) the shuttle (ST) and the stacking order of the coverslip (CS), AutoGrid (AG), spacer ring (SP) and screw (SC). Scale bars 10 mm, 5 mm and 2 mm respectively. (d) Microcooler thermal performance over time. T_{cs} and T_{sh} refer to the cold stage and shuttle holder temperatures (101.5 and 107 K respectively when stabilized). The heater power required for temperature stabilization is also plotted (P_{cs} and P_{sh}). The shuttle holder temperature is stabilized within 10 to 20 mK as shown at the bottom. As cryo pumping water from the rest gas slowly increases the radiative heat load, we changed the set point to 106 K at $t = 6$ h to have more heater power available for temperature stabilization. (e) Drift measured whilst regulating both cooler- and shuttle holder temperatures. (f) Peak to peak vibration amplitude as a function of frequency at 101 K cooler temperature (T_{cs}) and different directions. These spectra were measured with the microcooler mounted on an aluminium dummy stage inside the FIB-SEM system. The peak at 50 Hz originates from electrical interference.

sample cold for more than 9 h. The standing time is solely limited by cryopumping water from residual gas onto the cold surfaces as seen by the decrease in heater power (P_{cs} and P_{sh}) required for temperature stabilization. The lack of any liquid boil-off keeps the vibration- and drift levels very low. With the shuttle holder temperature stabilized within 10 to 20 mK (Figure 2.3d, bottom), the drift levels are approximately 1 nm/min along the y direction and 0.5 nm/min for the x direction. The peak to peak vibration levels are well below 1 nm in all directions. Peaks around 500 Hz are caused by high pressure gas undergoing expansion through a restriction in the cold stage. An internal braid decouples these vibrations best along the X direction, but is stiffer along Y and Z directions.

2.5 PIEZO POSITIONING STAGES

To position the sample within the vacuum chamber, the cryogenic microcooler is mounted on an in-vacuum piezo positioning stage having 5 degrees of freedom: X, Y, Z, R_x and R_z. It is built up from individual linear crossed roller bearing positioners using a piezo stick-slip mechanism (SLC Series, SmarAct GmbH) (Figure 2.4) (SmarAct GmbH, 2021). It is designed to have ±3 mm translation range in X, Y, Z and ±28° rotation range in R_x when aligned to the FIB-SEM coincident point. By setting $R_x = -28°$, the FIB maintains a 10° grazing incident angle to the sample surface. The stage has a clear aperture for the optical path and OL with the corresponding piezo positioning stage having 3 degrees of freedom: X, Y, Z.

The X and R_z axis of the sample stage operate independently whilst the Y, Z and R_x axis are coupled through a kinematic mount. The Y positioners are coupled to three positioners mounted on wedges, rotating them 45° in YZ plane. This geometry was optimized for its stiffness as rotations in R_x require the microcooler and connected tubing to be moved about. Z translation is obtained by moving the slanted positioners down whilst compensating the resulting Y shift with the Y positioners. In the detailed photograph on the right the microcooler mounting plate is shown. It has three ceramic balls on the bottom which mount into three kinematic mounts; two v-grooves and one point contact. Leaf springs on top keep the ceramic balls in place. The stage electronics are programmed such that all sample stage moves are performed in the (possibly rotated) sample coordinate system.

We measured the repositioning error of the stage by initiating a random move of the sample positioning stage and then returning to the start position. The same feature was brought into focus with FM (manually, by eye), and centered in the field of view (FOV). We then acquired images of the sample with the SEM and FIB. This procedure was repeated a number of times and the image to image shifts were used to determine the relative error in the X, Y and Z directions (sample coordinate system). From these measurements we estimated σ_X, σ_Y and σ_Z to be 41, 43 and 291 nm respectively (blue) when focusing using a widefield PSF. When using an astigmatic PSF (~110 mλ, orange) the repositioning error along Z is reduced significantly to 89 nm. To probe robustness to mechanical vibrations, we recorded

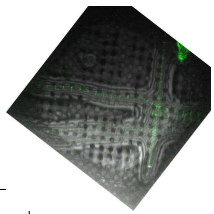

the vibration spectrum at room temperature With the microcooler mounted on the sample stage. The reduced stiffness of the sample stage alters the vibration spectrum, showing more and broader peaks above 100 Hz with respect to the aluminium dummy stage. However, the peak-to-peak vibration levels are well below 1 nm.

2.6 LIGHT MICROSCOPY-ASSISTED LAMELLA FABRICATION IN VITRIFIED CELLS

Sample loading and 3-beam alignment

With the microcooler at its operating temperature (<108 K), it is moved into the loading position by the piezo stage. Plunge frozen vitrified cells on a clipped TEM grid are loaded in the sample shuttle. The sample shuttle is picked up and transferred in using the modified Quorum transfer system. The sample stage is then positioned such that the TEM grid is brought into the SEM and FIB focus by positioning it near the coincident point of the FIB-SEM. Next, the OL stage is used to bring the sample into the optical microscope focus and care is taken to align the three beams by imaging a piece of bare grid foil with all imaging modalities. The thin (15 to 50 nm) grid foil allows precise alignment of all three beams in the following way: first the sample Z height is adjusted such that SEM and FIB image the same area on the sample. Next, the OL position is adjusted such that this area is also imaged in RLM and hence coincidence is achieved with the three beams. We found that the stability of the coincidence alignment was approximately 0.7, −0.2 and −0.05 µm/h for the X, Y and Z directions respectively. The largest drift is observed along the lamella width (X) which is typically not the most critical dimension, as the width usually spans several micrometers. See the Material & Methods section for more details.

After this, the objective lens stage is not moved anymore and sample navigation is done solely with the sample positioning stage (XY). Bringing a region of interest into the optical microscope focus is also done with the sample stage (Z) as X, Y, Z moves are performed in the rotated coordinate system of the sample. Having a region of interest in focus and centered in the FOV of the FM/RLM automatically aligns it to the center of the FIB and hence milling can commence.

Live monitoring and adjustment of FIB milling

FM and RLM images acquired before and during the milling process were used to monitor FIB milling (Figure 2.5). Drosophila and zebrafish myofibrils samples were used for these experiments (Sls(700) tagged with Alexa Fluor 488). The fluorescence (green) is overlaid on the reflected light (grayscale). A few cropped snapshots from this live recording are shown in Figure 2.5a. The image on the left shows the milling area by the dark blue rectangle and the fluorescent target is red encircled. Four different snapshots of this milling area are shown on the right. The varying color

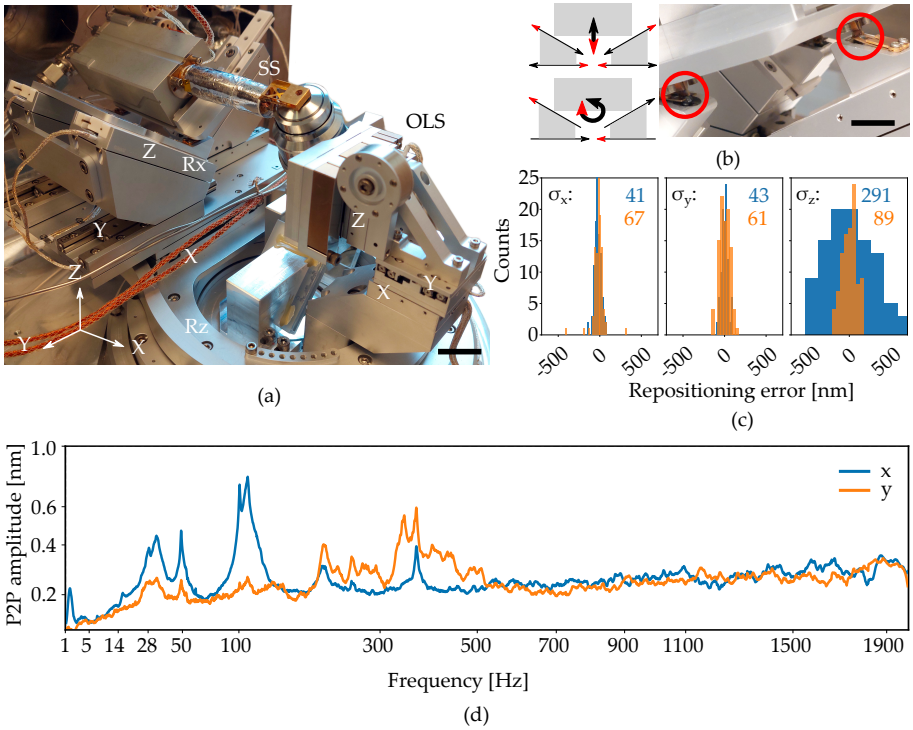

Figure 2.4: Piezo positioning stage design and performance. (a) Photograph of the piezo positioning stages used in the setup. The 5 degrees of freedom (DOF) sample stage (SS) moves the microcooler including sample holder around and the 3DOF stage (OLS) positions the OL. Scale bar 2 cm. (b) Schematic showing kinematic geometry for movements along Z and R_X. The microcooler is mounted on an interface plate having three ceramic ball contacts and mount to three kinematic mounts; two v-grooves and one point contact. (c) Repositioning error as measured when using the LM to repetitively centering and focusing the same feature in RLM. Images of the sample are acquired with the SEM and FIB and the image to image shifts are used to determine the repositioning error in the X, Y and Z directions (sample coordinate system). $\sigma_{X,Y,Z}$ indicated in blue and orange in nanometer. Number of measurements $N = 100$. (d) Peak to peak vibration amplitude as a function of frequency with the microcooler mounted on the 5DOF stage inside the FIB-SEM system. The peak at 50 Hz originates from electrical interference. Due to reduced stiffness of the sample stage (as compared to the aluminium dummy stage), an overall increase is measured whilst staying well below 1 nm peak-to-peak.

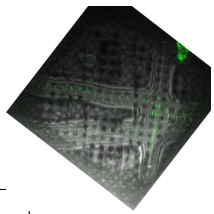

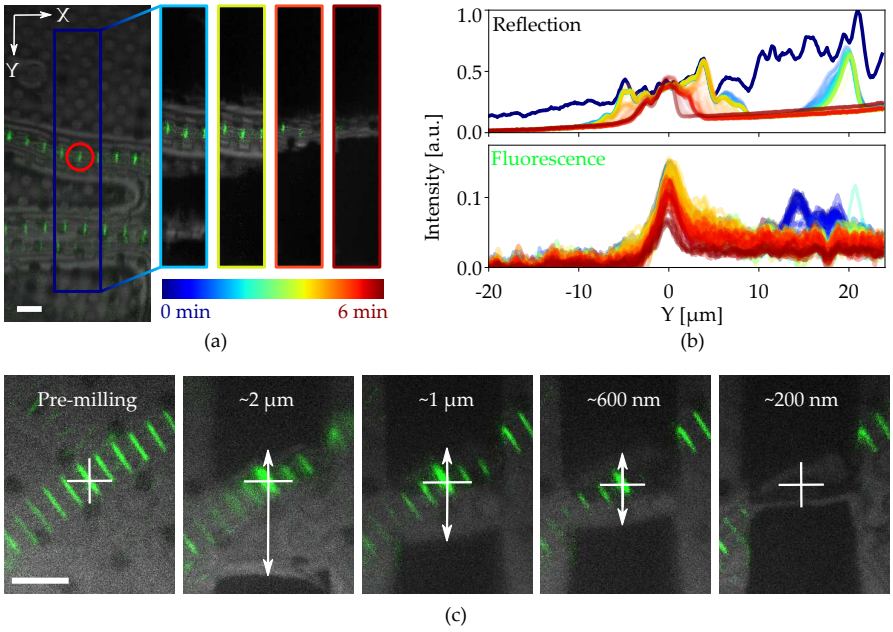

Figure 2.5: Light assisted FIB milling of frozen hydrated lamellae. (a) RLM and FM images were recorded whilst milling. The image on the left shows the indicated milling area marked in dark blue. The four images to the right show snapshots at different stages of milling, denoted with the varying color scale. This color scale is also used in (b) where the normalized integrated pixel intensity across the milling area Y direction is shown for both the reflection and fluorescence channels. (c) Stepwise milling progression as observed by RLM and FM. Estimated lamella thickness based on FIB images indicated at the top of the images. The fluorescent feature of interest is marked by the white cross and any misalignment (white arrows) can be corrected for. All scale bars are 5 µm. Drosophila and zebrafish myofibrils in (a) and (c) respectively. Fluorescence marks the Z-disc of the sarcomere.

scale is used to indicate the progress in time ranging from 0 to 6 min. In Figure 2.5b, the intensity of both the FM and RLM signals within the milling area are integrated along *X* and normalized. The dark blue curves are the integrated pixel intensity prior to milling. The light blue peak on the right in the reflection plot corresponds to the second (bottom) myofibril visible in Figure 2.5a. As the lamella gets thinner, the central reflected intensity peak becomes narrower (going from yellow to red). As the fluorescent target is larger than the lamella thickness, some loss of fluorescence is expected as is shown in the bottom plot. Although the fluorescence signal decreases it still remains after milling. The full video can be found in (Daan B Boltje, Hoogenboom, Jakobi, Jensen, Jonker, Kaag, Koster, Last, Agrela Pinto, and J. M. bibinitperiod o. Plitzko, 2022).

Quality control can be performed during every step of the milling procedure without the need for stage movements when switching between the different imaging modalities. Consequently, any misalignment of a feature of interest with respect to the center of the lamella is spotted and corrected for. After each step RLM and FM images are acquired. With the feature of interest marked by the white cross, it is easy to spot a misalignment (white arrows) and correct for this by shifting the milling patterns accordingly. This prevents accidentally milling away the feature of interest and increases sample preparation yield.

Fluorescence targeted milling and cryo-ET

We illustrate a fluorescence-targeted lamella fabrication workflow by targeting autophagic compartments in HeLa cells (Figure 2.6). We used a red fluorescent protein (RFP)-GFP tandem fluorescent-tagged LC3 (mRFP-GFP-LC3) single molecule-based probe that can monitor the autophagosome maturation process (Kimura et al., 2007a). This probe emits yellow signals (GFP plus RFP) in the cytosol and on autophagosomes but only red signals in autolysosomes because GFP is more easily quenched and/or degraded in the lysosome than RFP (Katayama et al., 2008). We selected regions of LC3-positive punctae using the mRFP-GFP fluorescence signal and focused this region in the center of the field of view. We then cut the lamella step-by-step and finally polished whilst making sure the feature of interest is still present (Figure 2.6a through d) at all stages. The contrast was increased to make the fluorescence visible (Figure 2.6d, left) and the final lamella imaged by FIB in the right panel. The sample containing the milled lamella was removed from the FIB-SEM using the transfer system and loaded into the autoloader of the cryo TEM. An overview image of the lamella was acquired and using the RLM image data we overlaid the FM signal guided by the the outline of the lamella as imaged by TEM and RLM. We then acquired tilt series at the sites still showing fluorescence and a z stack is reconstructed the tomograms. No signs of devitrification were visible in these reconstructions, indicating the sample has been well preserved during the entire procedure.

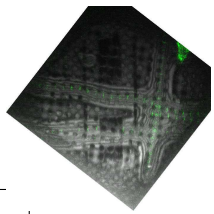

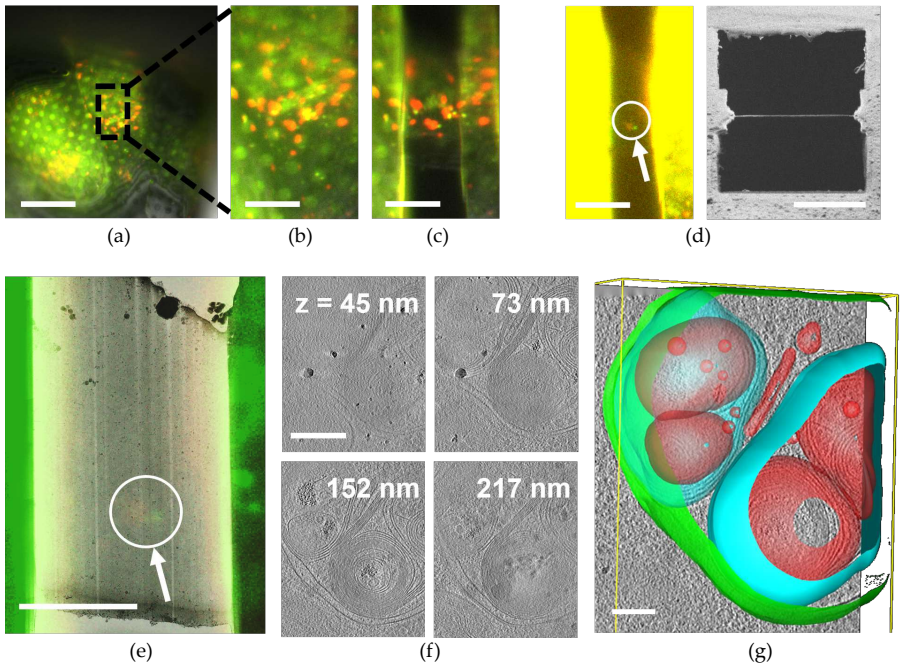

Figure 2.6: Light targeted FIB milling of frozen hydrated lamellae. (a) First the sample is brought into the center of the FOV and focussed properly. Green & yellow: autophagosomes and red: autophagolysosomes. (b) Close-up of **(a)** showing the milling area in more detail. (c) Snapshot taken at an intermediate milling step. (d) left; the lamella finished and polished, imaged in the FM and the contrast enhanced to show the feature of interest. Right; a snapshot acquired with the FIB showing the polished lamella. (e) the RLM channel is used to align the light microscope data with the TEM overview image. The fluorescent feature of interest indicates where the tomogram should be acquired. (f) *Z* slices of the reconstructed TEM tomogram with (g) segmentated membranes. Annotated are autophagolysosome outer membrane (green), autophagolysosome membraneous content (blue and red). Scale bars: (a) - 40 µm, (b) - 10 µm, (c) - 5 µm, (d) left - 10 µm, (d) right - 5 µm, (e) - 5 µm, (f) - 0.25 µm, (g) - 0.1 µm.

2.7 DISCUSSION

Currently, the system presented is solely compatible with samples in an AutoGrid form factor. With minor modifications, other planar sample types, such as samples prepared by the Waffle Method (K. Kelley et al., 2022), would fit inside the sample shuttle. Identifying grid bars and sample navigation can be done directly using the LM. Imaging through a relatively thick sample (~50 µm) pose potential challenges, as the increased imaging depth is likely to induce aberrations and increased scattering.

Although the system presented reduces the sample handling steps, contamination and avoids the use of fiducial markers, it also has its limitations: (i) Without an additional external cryo fluorescence microscope, FM can only be done when the sample is clipped and loaded into the FIB-SEM; (ii) A required working distance of ~1 mm prevents high (>1) NA objective lenses to be used; (iii) Implementing a cryo-immersion objective lens adds significant complications and is not straight forward; (iv) The integrated approach reduces the number of available methods for super resolution microscopy due to the need for a compact optical path.

External cryogenic super resolution microscopy can readily provide sub diffraction limit imaging and can provide a milling target, but the localization precision will only be as good as the correlation accuracy provided by the fiducial markers images in both LM and FIB. This same limitation also applies to the different commercially available integrated LM systems that can be retrofitted onto the FIB-SEM, but require in-vacuum stage movements (Smeets et al., 2021; ThermoFisher Scientific, 2021).

We have implemented a system of two rotatable cylindrical lenses to allow fluorescence imaging with an astigmatic PSF. We have demonstrated that astigmatic imaging improves re-localization accuracy after stage movements to within 90 nm along the optical axis. Further work could push this concept further towards quantitative localization of multiple or potentially even single fluorophores and consequently targeted milling with even lower positional errors. This would also open up the possibility for automated milling, based on acquired LM (astigmatic) data. For this to work, we would need to automatically correct for deviations in the coincident alignment or update the alignment regularly, but this requires more work to be done.

Moreover, an intriguing prospect would be to extend this concept towards cryogenic super resolution microscopy correlated with both SEM and FIB. Potentially, this could also allow for super resolution FM imaging after polishing the lamella, ultimately combining at the single protein level high resolution biological information with the structural data obtained from TEM.

2.8 CONCLUSION

We have developed a coincident 3 beam microscope for the cryo-ET workflow which allows direct light microscopy targeted lamella fabrication, without the need for repositioning or fiducial markers. The fluorescence signal intensity from the lamella can be monitored whilst milling making sure that the target remains intact. Any

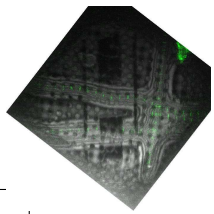

misalignment can be directly observed and corrected. The 5-channel inverted epi-fluorescent light microscope is diffraction limited in wide field imaging with an NA up to 0.85. Astigmatic point spread function shaping is achieved through the use of a Stokes variable power cross-cylinder lens set. This allows positioning of the sample for targeted milling with errors as small as 25 nm in XY and 90 nm in Z. The system utilises a novel, liquid nitrogen free cooler design having low levels of vibrations, drift, and an up time of more than nine hours. The entire cryogenic fluorescence microscope can be integrated into a regular FIB-SEM, effectively converting it into a cryo-LM-FIB-SEM, making it possible to add *in-situ* fluorescence targeted milling in an established cryo-ET workflow.

Our approach allows for a live, reflection and/or fluorescence image feed while milling takes place. This opens the additional possibility of an automated milling procedure in which the fluorescent feature of interest is with certainty inside the lamella, before the sample is transferred to the TEM.

2.9 ACKNOWLEDGMENTS

Drosophila flight muscle myofibrils were kindly provided by E.H. Chan & F. Schnorrer (Institut de Biologie du Développement de Marseille), and zebrafish myofibrils by Y. Hinits & M. Gautel (King's College London). We express our gratitude to Fulvio Reggiori (University of Groningen, Netherlands) for providing the HeLa cells and are thankful to Mingjun Xu for help during sample preparation. We thank Andries Effting (Delmic B.V.) for helpful discussions, and we would like to thank Ryan Lane (TU Delft) for his contribution in various PYTHON developments. The majority of the 3D CAD design was done by Thomas van der Heijden (Delmic B.V.), for which we are gratefull. This work was financially supported by; NWO-TTW project Nº 17152 to JPH, NIH grant RO1 AI127401 to GJJ, European SME2 grant Nº 879673 to Delmic B.V. and Eurostars grant Nº E13008 to SH and SR.

2.10 AUTHOR CONTRIBUTIONS

SH conceived and initialized the collaboration between the different research groups. Initial ideas and insight into the cryo-ET workflow was provided by JPH, AJJ, GJJ, AJK, JMP, SR and RW. The majority of the conceptual system design was done by DBB with feedback from JPH, AJJ, GJJ, AJK, JMP, SR, RW and SH. DBB, CTHJ and MGFL, planned and carried out the experiments. ST and ZW assisted in doing cryo-FIB milling and performed cryo-ET experiments. EBW helped with light microscopy experiments and PSF analysis. MJK performed the stage reposition measurements. AJJ and CAP prepared the HeLa samples whilst ZW provided the myofibril samples. DBB processed and analyzed the data with input from JPH, AJJ, CTHJ, MGFL, ST, ZW and EBW. DBB wrote the manuscript with input from EBW, AJJ, and JPH. All authors discussed the results and commented on the manuscript.

2.11 DECLARATION OF COMPETING INTEREST

AJJ, GJJ, CTHJ, MJK, AJK, MGFL, CAP, JMP, SR, ST, ZW, EBW and RW declare that they have no known competing financial interests or personal relationships that could have appeared to influence the work reported in this paper. DBB is, and CTHJ and MGFL were, employees of Delmic BV, JPH and SH have a financial interest in Delmic BV.

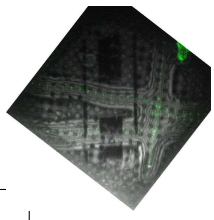

3

DEPTH-DEPENDENT SCALING OF AXIAL DISTANCES IN LIGHT MICROSCOPY

When fabricating frozen-hydrated lamellae for cryogenic electron tomography, precise targeting and milling are critical. When targeting inside a frozen cell through cryogenic fluorescence microscopy, a mismatch in refractive indices is unavoidable, leading to axial deformation in the acquired images. Over the years, various scaling factors have been proposed to correct this deformation, but none have accounted for depth-dependent, non-linear scaling. An analytical theory is presented to address this, by determining the leading constructive interference band in the objective lens pupil under refractive index mismatch conditions. This theory allows the calculation of a depth-dependent re-scaling factor based on the numerical aperture, the refractive indices, and the wavelength. The analytical results are validated through wave-optics calculations and experimental data obtained using a measurement scheme for different numerical apertures and refractive index mismatch values. Multiple datasets under various refractive index mismatch conditions are recorded, and corrected these using the depth-dependent axial scaling theory. Additionally, an online tool has been developed that visualizes the depth-dependent axial re-scaling for specific optical setups. Software to help microscopists accurately re-scale the axial dimension in their imaging data when working under refractive index mismatch conditions, is also provided.

3.1 INTRODUCTION

Optical sectioning has enabled imaging of large volumes by FM, as realized in confocal, two-photon microscopy (Pawley, 2006), structured illumination microscopy (SIM) (Saxena et al., 2015) and light sheet microscopy (Stelzer et al., 2021). For optimal imaging, aberrations need to be minimized by avoiding a RIM between the detection microscope objective immersion medium n_1 and specimen n_2 (Pawley, 2006). Failing to do so results in the blurring of the PSF of the microscope and therefore a loss in resolving power, as well as in a deformation of the recorded volume along the optical axis.

This axial deformation arises from the refraction of the peripheral rays on the RIM interface, causing an axial shift of their focal point with respect to the focal point of the paraxial rays (Diel et al., 2020). This effect can be characterized using focal shift $\Delta f = \text{AFP} - \text{NFP}$, where AFP is the actual focal position (the real position of the

This chapter has been published as: Loginov[†] and Boltje[†] et al. (2024). "Depth-dependent scaling of axial distances in light microscopy." In: Optica, pp. 553-568.
[†] These authors contributed equally to this work.

object) and NFP is the apparent or nominal focal position (the microscope z-position where the object is found in focus) (Pawley, 2006). Just as the true lateral distances are recalculated back from an image using the magnification of the objective M, so ought the actual focal positions (AFPs) (i.e. the true axial distances) to be re-scaled using the re-scaling factor $\zeta = \text{AFP}/\text{NFP}$. The accurate knowledge of the re-scaling factor enables reliable quantitative volumetric microscopy.

While it is generally unfavorable to have a refractive index mismatch, for e.g. illumination intensities in confocal microscopy, there are common imaging scenarios in which a mismatch is still present in the most optimal configuration (Diel et al., 2020; Pawley, 2006). For instance, as the resolving power of the microscope depends on the NA of the detection objective, high-NA oil immersion objectives ($n_1 = 1.52$) are used to image water-like specimens ($n_2 \approx 1.33$). In addition, embedding and fixation media rarely match exactly, in terms of refractive index, the immersion media of air, water, silicone, glycerol or oil objectives, leading to the axial deformation of the imaged volumes.

Refractive index mismatches are often more pronounced in integrated cryogenic fluorescence and/or correlative microscopy (Ando et al., 2018; De Boer et al., 2015; Kaufmann et al., 2014; Wolff, Hagen, et al., 2016). In such systems, light and electron microscopy are combined in a single setup, and air objectives are often used for imaging specimens with a higher refractive index. The use of air objectives is a straight-forward choice, as the specimen resides in a vacuum chamber for electron microscopy. In cryogenic fluorescence microscopy the specimen is cooled to temperatures below 120 K, which makes the use of a non-touching air objective favorable, as any other (touching) immersion objectives are challenging in terms of engineering (Daan B Boltje, Hoogenboom, Jakobi, Jensen, Jonker, Kaag, Koster, Last, Agrela Pinto, J. M. Plitzko, et al., 2022; Gorelick et al., 2019; S. Li et al., 2023; W. Li et al., 2023).

The development of the confocal microscope, along with its optical sectioning capability, allowed for 3D imaging, and hence the need for axial scaling theories arose. In the paraxial approximation, the axial distances are simply re-scaled using the ratio of the two refractive indices (Carlsson, 1991), which works well for low NA objectives. Visser *et al.* presented a scaling theory which is based on the contribution of the high-angle (or marginal) rays to the axial scaling (Visser et al., 1996). More recently, several scaling theories have been presented, which result in re-scaling factors somewhere in between the paraxial and high-angle approximations (Diel et al., 2020; Lyakin et al., 2017; Stallinga, 2005). The most accurate method to determine axial scaling are full wave-optics calculations of the microscope's point spread function under RIM (Egner et al., 2006; Hell et al., 1993; Sheppard et al., 1997). As these calculations are computationally expensive and complex, they are hardly used by microscopists to calculate the axial re-scaling factor.

The re-scaling factor can also be measured experimentally by observing the nominal focal position (NFP) of a fluorescent bead or interface through a medium with refractive index n_2, whilst knowing the AFP of said bead or interface. This can

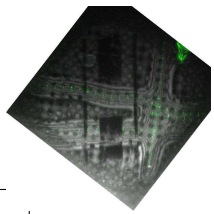

be done by constructing a sample cell where the fluorescence is present far from the coverslip, which is later filled with a liquid with n_2 (Besseling et al., 2015; Diel et al., 2020; Grauw et al., 1999). The AFP can be obtained through imaging with an objective where $n_1 = n_2$ (Besseling et al., 2015; Diel et al., 2020; Grauw et al., 1999) or by measuring Fabry–Pérot fringes in the transmission spectrum of the cell (Besseling et al., 2015). Alternatively, the apparent axial deformation of a spherical object, larger than the PSF of the microscope, can be used to measure the axial scaling (Diaspro et al., 2002; Visser et al., 1996). Recently, a different approach was presented where a coverslip was step-wise coated with a low-index polymer ($n_2 \approx 1.33$) and the AFP was measured using stylus profilometry (Petrov et al., 2020). With this method, the axial scaling can be measured in the range of a few microns from the coverslip, while the former methods are used to measure tens of microns away from the coverslip.

While the explicit axial scaling theories in literature are all depth-independent, there exist some reports in literature that this factor is actually depth-dependent. In 1993, Hell *et al.* wrote *"...it can be expected that the regions close to the cover glass are slightly more scaled than those in deeper regions of the specimen."* (Hell et al., 1993). Later, wave-optics calculations showed a non-linear dependence of the focal shift Δf on the imaging depth for high-NA objectives and large RIMs (Egner et al., 2006; Sheppard et al., 1997). For instance, Sheppard and Török reported a non-linear dependence of the focal shift Δf at a depth <30 µm from the coverslip using wave-optics calculations (NA = 1.3, n_1 = 1.52, n_2 = 1.33) (Sheppard et al., 1997), where the re-scaling factor was 5% larger close to the coverslip than at large distances. More recently, the measurements by Petrov *et al.* showed significant non-linear axial scaling for imaging depths < 4 µm (Petrov et al., 2020).

There is, up to now, no straightforward equation which can be used to explicitly calculate the re-scaling factor as a function of depth. Moreover, a depth-dependence of the re-scaling factor has not been measured experimentally for large depths, and for several NAs and multiple RIM conditions.

Here, we present an analytical theory which calculates the depth-dependent re-scaling factor as a function of the NA, the refractive indices n_1 and n_2, and the wavelength λ. The gist of the theory is in the determination of the leading constructive interference band in the objective lens' pupil under RIM. We compare the theory to both full wave-optics calculations and experiments. In the experiments, we have imaged the gap between two substrates that were brought closer to each other step by step. By filling the space between the substrates with a liquid with index n_2 we were able to measure the NFP, while the AFP was determined independently from the microscope by the piezo-stage holding the top substrate. We have measured the re-scaling factor ζ for several objectives with various NAs, immersion refractive index n_1, and sample refractive index n_2, with both RIMs where $n_1 < n_2$ and $n_1 > n_2$ in a wide range of depths and compared them to the analytical theory and the wave-optics calculations. We demonstrate that the axial re-scaling of 3D microscopy data, recorded with a refractive index mismatch, using the depth-dependent re-scaling factor outperforms the re-scaling using existing linear re-scaling theories from lit-

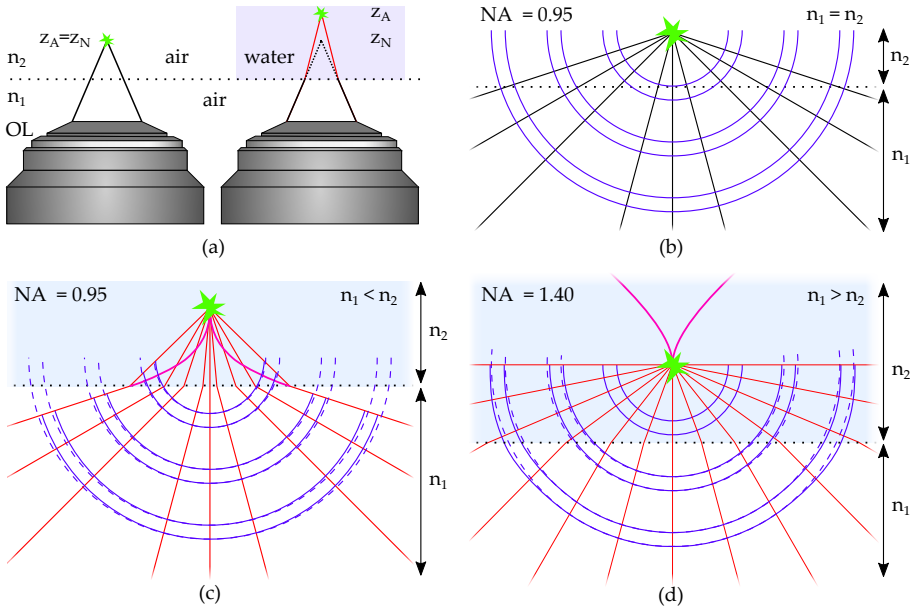

Figure 3.1: The effects of RIM demonstrated with geometrical optics. (a) An OL imaging a fluorescent object (green star) with- and without refractive index mismatch, left and right respectively. The dotted boxes are detailed out in panels b through d. (b) A fluorescent object (green star) sits $z_A = 10\,\mu$m deep from the refractive index interface (dotted line) between n_1 and n_2. With $n_1 = n_2 = 1.0$, rays (black) and wave-fronts (blue) are depicted. (c) In the case where $n_1 = 1.0, n_2 = 1.33$ the ideal spherical wave-fronts (dashed blue) are deformed (solid blue) after crossing the refractive index (RI) interface. Rays are depicted in red to indicate RIM and the caustical surface (purple) shows where geometrical optics breaks down. (d) In the opposite RIM case, where $n_1 = 1.52, n_2 = 1.33$, again the wave-fronts are deformed under RIM and total internal reflection occurs. The NA is 0.95 (b, c) and 1.4 (d).

erature. Finally, we provide the reader with an online web applet where one can visualize the depth-dependent axial re-scaling factor for their specific optical setup and PYTHON software to re-scale data acquired under RIM.

3.2 SCALING OF AXIAL DISTANCES DUE TO REFRACTIVE INDEX MISMATCH

Geometrical optics

Given a fluorescent object emitting light in an ideal, spherical fashion, a flat interface with a refractive index mismatch will cause disturbance to the fluorescent light propagation – in the form of refraction. When an objective lens is collecting light under RIM, this effect will be more pronounced with increasing NA of the OL (and therefore collection angle), see Figure 3.1a for the overall geometry.

This is further illustrated using geometrical optics in Figure 3.1b through d, where a light source is located 10 µm away from the interface between n_1 and n_2. In Fig-

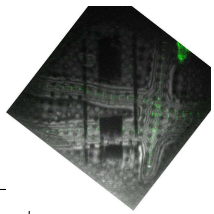

ure 3.1b no RIM is present ($n_1 = n_2 = 1.0$), where the undisturbed wave-fronts and rays are shown in solid blue and black respectively. The dotted horizontal line depicts the interface with the RIM. Figure 3.1c and d show two cases where RIMs are present respectively for $n_1 < n_2$ and $n_1 > n_2$. The black rays follow Snell's law when crossing the interface, resulting in the wave-fronts (solid blue) deviating from the ideal spherical shape (dashed blue). The caustic surface (purple) indicates where geometrical optics breaks down. From this simple illustration, we see that the effect of RIM becomes more pronounced with increasing collection angles (numerical aperture) and increasing RIM contrast $\Delta n = |n_2 - n_1|$.

When imaging with a microscope, there are two (independent) axial coordinates to be considered: the actual depth of the fluorescent emitter z_A, as measured from the RIM interface ($z_A = 10\mu$m in Figure 3.1) and the nominal depth of the focal plane of the microscope into the sample z_N. A 3D image stack recorded with a microscope under RIM has z_N as an axial coordinate. Similar to using the magnification M to re-calculate the true lateral dimensions, the axial coordinates should be re-scaled using the re-scaling factor $\zeta \equiv z_A / z_N$ to obtain a 3D stack with the actual depth z_A as an axial coordinate.

Geometrical optics can produce several estimates for the re-scaling factor ζ. The paraxial rays are nicely focused, even under RIM, producing the estimate (Carlsson, 1991):

$$\zeta_{\text{paraxial}} = n_2 / n_1. \tag{3.1}$$

Another geometrical optics estimate comes from Visser *et al.*, obtained from the marginal rays still fitting into the NA (Visser et al., 1996):

$$\zeta_{\text{marginal}} = \sqrt{\frac{(n_2^2 - \text{NA}^2)}{(n_1^2 - \text{NA}^2)}}. \tag{3.2}$$

The two re-scaling factor values ζ_{paraxial} and ζ_{marginal} are irreconcilable in a modern high-performance objective lenses (with NA $\rightarrow 0.95 \times n_1$). For the example shown in Figure 3.1c, $\zeta_{\text{paraxial}} = 1.33$ and $\zeta_{\text{marginal}} = 2.98$, whilst for Figure 3.1d $\zeta_{\text{paraxial}} = 0.88$ and $\zeta_{\text{marginal}} \rightarrow 0$. Although these estimates are derived from geometrical optics, ζ_{paraxial} and ζ_{marginal} do provide lower and upper bounds when $n_1 < n_2$ (reverse when $n_1 > n_2$) and are still useful checks in the wave-optics treatment.

Analytical expression describing depth-dependent axial scaling

When considering the PSF of a wide-field microscope under RIM two intrinsic length scales need to be considered: (i) several strictly geometrical parameters n_1, n_2, z_A, z_N, & NA, and (ii) the physical parameter of the (vacuum) wavelength of light used $\lambda = 2\pi / k$ which is independent from the exact RIM geometry, where k is the wave number. With changing imaging depth, the geometrical parameters z_A, z_N do change, while the wavelength of light λ does not. Following the derivation outlined

below, we find it is exactly the interplay between the two length scales that yields a depth-dependent re-scaling factor:

$$\zeta = \begin{cases} \min[\zeta_{\text{univ}}, \zeta_{\text{crit}}], & \text{if } n_2 \geq n_1 \\ \max[\zeta_{\text{univ}}, \zeta_{\text{crit}}], & \text{otherwise} \end{cases} \tag{3.3}$$

with

$$\begin{aligned} \zeta_{\text{univ}} &= \frac{n_2}{n_1} \times \frac{(1-\epsilon)+\frac{m}{n_1}\sqrt{\epsilon(2-\epsilon)}}{1-\left(\frac{n_2}{n_1}\right)^2\epsilon(2-\epsilon)}, \\ \zeta_{\text{crit}} &= \text{Re}\left(\frac{n_1-\sqrt{n_1^2-\text{NA}^2}}{n_2-\sqrt{n_2^2-\text{NA}^2}}\right), \\ m^2 &= n_2^2 - n_1^2, \\ \epsilon &= \frac{\lambda/4}{z_A n_2} \times \begin{cases} +1, & \text{if } n_2 \geq n_1 \\ -1, & \text{otherwise} \end{cases} \end{aligned}$$

where ζ is the axial re-scaling factor ($\zeta \equiv z_A/z_N$), n_1 is the immersion refractive index, n_2 the sample refractive index, λ the wavelength (in vacuum), z_A the actual depth of the imaged object and NA the numerical aperture. The re-scaling factor ζ is a combination of the depth-dependent and NA-independent ζ_{univ} which approaches the paraxial limit ζ_{paraxial} for large depths, and the depth-independent and NA-dependent ζ_{crit} at shallow depths. ζ_{crit} becomes relevant at such shallow depths where the assumptions used to derive ζ_{univ} breakdown.

Derivation of analytical theory through wave-optics

With geometrical optics ambiguous in defining the re-scaling factor ζ we have to turn to wave-optics.[1] The most complete wave-optics theory describing aberrations occurring under RIM was developed by Hell *et al.* (Hell et al., 1993). Wave-optics provides a clear prediction of the behavior of a microscope imaging under RIM. A scalar (radially symmetric) PSF of a wide-field microscope under RIM is an integral over Bessel-beams:

$$\text{PSF}\left(x, y, z_A, z_N\right) = \left| \int A(\theta) \times J_0(r\, k_r) \times e^{i\Phi(\theta)} \sin\theta \, \mathrm{d}\theta \right|^2, \tag{3.4}$$

where the PSF is dependent on both the actual depth z_A and on the nominal depth z_N, as an image with intensities $I(x, y, z_N)$ is a convolution of fluorophore distribution $f(x, y, z_A)$ and the PSF(x, y, z_A, z_N). For a given depth z_A of a fluorescent object there is a focal plane depth $z_N(z_A)$ where the PSF is maximal (i.e. the object is in focus), and $\zeta(z_A) \equiv z_A/z_N(z_A)$. Under RIM, the two intrinsic length scales mentioned above

1 This is the gist of the full derivation found in Loginov et al. (2024)

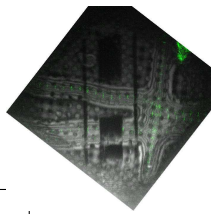

play a role. These two length scales are fused together in Equation 3.4 via the phase function $\Phi(\theta)$:

$$\Phi(\theta) = k'_z(\theta) \times z_A - k_z(\theta) \times z_N, \tag{3.5}$$

where k_z and k'_z are the axial wave-numbers of the Bessel beams, respectively for a matched case and one undergoing RIM. With changing imaging depth, the geometrical parameters also change (e.g. the path length difference between the paraxial and the marginal rays). Reversely, the wavelength of light does not depend on the depth, and so it is the interplay between geometrical and physical length scales that results in a depth-dependent re-scaling factor $\zeta(z_A) \neq \text{const}$.

The maxima positions of Equation 3.4 can be estimated by finding the stationary points θ^* where $\mathrm{d}\Phi/\mathrm{d}\theta = 0$ (Loginov et al., 2024; Stamnes, 2002). There is always a stationary point at $\theta = 0$, and a stationary point might appear for a single non-zero θ. For a given z_A and z_N, there is an interference between the contributions from the two critical points ($e^{i\Phi(0)}$ and $e^{i\Phi(\theta^*)}$) which controls the shape of the PSF. And when the interference is the most constructive – then the object appears in focus. The stationary phase points of the simplified version of Equation 3.4 correspond to the rays of geometrical optics (Keller, 1962; Stamnes, 2002; Wolf, 1959). Hence, the re-scaling factor must fall within the bounds set by ζ_{paraxial} and ζ_{marginal}. Contrary to the purely geometrical optics approach, we have now two contributions to balance: the paraxial one $e^{i\Phi(0)}$ and the intermediate one $e^{i\Phi(\theta^*)}$.

Their relative strengths depend on the width of the stationary points of Φ, and hence on the second derivative of Φ (Loginov et al., 2024). Instead of finding the exact weight of each contribution, we study how the phase function $\Phi(\theta)$ behaves in several focal positions $z_N(z_A)$, which can be determined by full vectorial PSF calculations. In doing so the following condition is set when deriving an explicit formula for ζ:

$$\Phi(\theta^*) - \Phi(0) \approx -\frac{\pi}{2}, \tag{3.6}$$

where a fixed $-\pi/2$ separation is assumed, as if the two stationary points constitute a single and uninterrupted constructive interference area when the microscope is in focus. With this approximate condition, Snell's law, and the Ewalds' spheres scaling, an explicit formula for ζ can be derived (Loginov et al., 2024).

Re-scaling microscopy data

When re-scaling microscopy data from the native z_N coordinate into the true depth coordinate z_A, it is convenient to use the re-scaling factor as a function of the *nominal depth* z_N instead of the actual depth z_A. In this case, a different dimensionless parameter δ can be used for the derivation:

$$\delta \equiv \frac{\lambda/4}{n_1 z_N}, \tag{3.7}$$

and:

$$m\sqrt{\zeta^2-1} = n_2\zeta - n_1(1+\delta),$$
$$\zeta^2 - 2\frac{n_2}{n_1}(1+\delta)\zeta + (\frac{m}{n_1})^2 + (1+\delta)^2 = 0,$$

yielding the re-scaling factor as a function of z_N:

$$\zeta(z_N) \quad = \frac{n_2}{n_1} \times (1+\delta) + \frac{m}{n_1}\sqrt{\delta(2+\delta)}. \tag{3.8}$$

3.3 METHODS

Wave-optics calculations

The computations of the integrals were performed through a MATLAB script producing 2D PSF cross-sections ($r \times z_N$, $10 \times 20\,\mu m$) on a $N^2 = 2048 \times 2048$ pixel grid from $M = 2000$ Bessel-beam components, specifics can be found in (Loginov et al., 2024). To minimize the number of Bessel function invocations, each of the integrals I_i was represented as a double matrix product:

$$I_i = J_i^{N\times N} \times A_i^{M\times M} \times E^{M\times N},$$

where $J_i^{N\times N}$ is the matrix containing the Bessel function, $A_i^{M\times M}$ is the diagonal matrix created from all the position independent factors and $E^{M\times N}$ is the matrix containing the z_N dependent phase change of M Bessel-beams.

For every RIM condition, a series of 2D PSF cross-sections (lateral × axial, XZ planes) was generated with the actual depth z_A changing from 0.2 to 5 µm with a step of 0.2 µm. Step sizes of 0.5 µm and 1.0 µm were used respectively from 5.5 to 25 µm and from 26 to 150 µm. The axial center of the calculated PSF frame was shifted with the actual depth z_A using the paraxial scaling factor $z_N^0 = z_A(n_1/n_2)$. In the lateral center of each frame, the Z profile was extracted and passed through a Butterworth low-pass filter (5^{th} order, sampling and critical frequencies $f_s = 0.1\,\text{nm}^{-1}$, $f_c = 0.003\,\text{nm}^{-1}$) to remove high frequency ringing oscillations. The axial focal position z_N^* was determined by taking the maximum of the filtered profile and the re-scaling factor was computed as $\zeta = z_A/z_N^*$.

Axial scaling measurements

We measured the depth-dependent axial scaling using a fluorescence microscope setup described earlier (Daan B Boltje, Hoogenboom, Jakobi, Jensen, Jonker, Kaag, Koster, Last, Agrela Pinto, J. M. Plitzko, et al., 2022), for different refractive index mismatches and numerical apertures, as listed in Table 3.1 (CC for correction collar). A schematic of the measurement scheme is shown in Figure 3.2a, where a sapphire ball (BA, Ceratec, 2 mm diameter, grade 10) is separated from a coverslip (CS, Thorlabs #CG15CH2, 22 × 22 mm, #1.5H thickness). The sapphire ball was glued to a

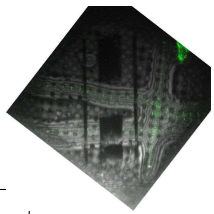

Table 3.1: Overview of microscope objectives and refractive indices in the measurements.

NA	Nikon #	M	Pixel size [nm]	FOV [µm]	CC	n_1	n_2
0.70	MRH08630	60 ×	108.3	110.9	Yes	1.0	1.0
|	|	|	|	|	|	1.0	1.34
|	|	|	|	|	|	1.0	1.52
0.85	MUE35900	100 ×	65	133.12	Yes	1.0	1.0
|	|	|	|	|	|	1.0	1.34
|	|	|	|	|	|	1.0	1.52
0.95	MRD00605	60 ×	108.3	110.9	Yes	1.0	1.0
|	|	|	|	|	|	1.0	1.34
|	|	|	|	|	|	1.0	1.52
1.25	MRD77400	40 ×	162.5	166.4	No	1.34	1.34
1.40	MRD01901	100 ×	65	133.12	No	1.52	1.52
|	|	|	|	|	|	1.52	1.34
|	|	|	|	|	|	1.52	1.0

glass strip (GS) with a small droplet of UV curable glue (Norland Optical Adhesive 63). Fluorescent beads (FB, diameter 190 nm, excitation 480 nm, emission 520 nm, Bangs Labs #FSDG002) were dropcasted on the coverslip using a micropipette. Both surfaces were cleaned with acetone, isopropyl alcohol and dried with nitrogen. The glued sapphire ball was dipped in the solution and dried three times to apply the beads to the surface. Beads on both surfaces were imaged by acquiring a z-stack with the fluorescence microscope using an excitation wavelength of 485 nm (Lumencor SPECTRA X), dichroic mirror (Semrock #FF410/504/582/669-Di01-25x36) and an emission filter (Semrock #FF01-525/30-25). The objective lens was mounted upright and was moved by stick-slip piezo positioners (SmarAct GmbH) in X, Y and Z. The correction collar setting of the OL was optimized to minimize spherical aberrations when imaging beads on the coverslip. The glass strip with sapphire ball was mounted to the sample shuttle holder (SSH), Figure 3.2b. This holder was moved by piezo positioners, and hence the distance between the coverslip and the ball was controlled. Details on the positioning systems can be found in (Daan B Boltje, Hoogenboom, Jakobi, Jensen, Jonker, Kaag, Koster, Last, Agrela Pinto, J. M. Plitzko, et al., 2022).

We used different objective lenses, but all were compatible with the Nikon CFI60 optical system, and were used together with a 200 mm tube lens (Nikon #MXA20696). Care was taken to center the pupil of the objective lens to the center of the tube lens, after which the objective lens was solely moved along the optical axis. With the distance between ball and coverslip set, a z-stack was acquired by moving the objective lens. In Figure 3.2c the maximum intensity projection along Y is shown for such a z-stack, where the fluorescent beads were imaged using a 100×, 0.85

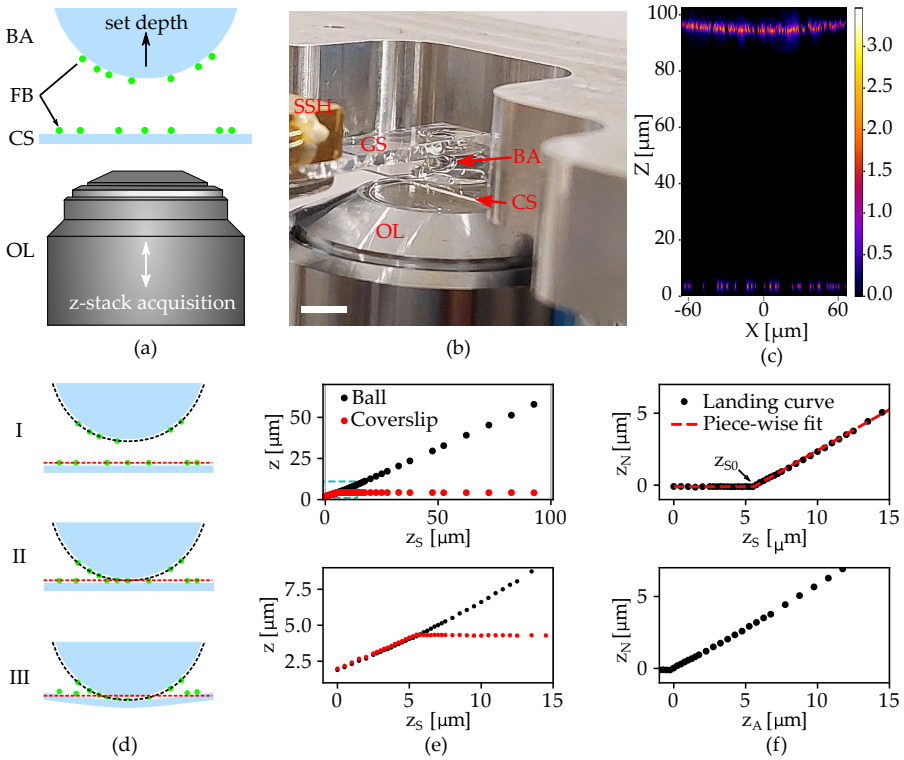

Figure 3.2: The experimental setup, and data analysis procedure, used to measure depth-dependent axial scaling. (a) Schematic showing the movable optical objective lens (OL) and sapphire ball (BA) at opposite sides of the static coverslip (CS), with fluorescent beads (FB) on their surfaces. (b) Photograph showing the objective lens (OL), coverslip (CS) and sapphire ball (BA). The ball is glued to a glass strip (GS), which is mounted to the sample shuttle holder (SSH). Scale bar 3 mm. (c) Maximum intensity projection along the Y axis of a recorded z-stack where $n_1 = n_2 = 1.0$. The bottom fluorescent signal originates from beads residing on the coverslip, and the signal at the top from beads on the sapphire ball, shown by the visible curvature. (d) Schematic showing three different distances between ball and coverslip, going from clear separation (I) to contact (II) and deformation of the coverslip (III). The dashed lines indicate the position of both ball (red) and coverslip (black). (e) The position of the coverslip and ball versus the set ball-coverslip distance z_S (top) and the same data near the coverslip (bottom). (f) The landing curve (in z_N coordinates), plotted against the set depth z_S (top). The fit values from a piecewise linear fit are used to determine the contact point between ball and coverslip, and this yields the observed focal depth z_N versus the actual depth z_A from which the re-scaling factor $\zeta = z_A/z_N$ was calculated (bottom).

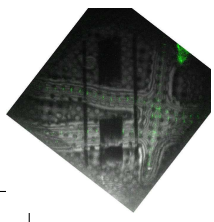

NA objective (Nikon #MUE35900) in the absence of a refractive index mismatch ($n_1 = n_2 = 1.0$). The bottom fluorescent signal originates from fluorescent beads residing on the coverslip. The signal at the top comes from the beads on the sapphire ball, as recognized by the visible curvature.

The AFP was varied by changing the distance between ball and coverslip, and the contact point between them was first approximately set by having both the fluorescent beads on the coverslip and bottom side of the ball in focus of the microscope. Next, the starting AFP (z_A, typically around 100 µm) was set by moving the ball away from the coverslip and the AFP was reduced step by step (see Figure 3.2d, I through III). At each set depth z_A, a z-stack is recorded around the coverslip and ball separately (by moving the objective lens, −4 to 8 µm and −8 to 8 µm respectively, both with a step size of 0.25 µm). To ensure the second z-stack was acquired around the beads on the surface of the ball, we used ζ_{marginal} and ζ_{paraxial} estimates for < 20 µm and, > 20 µm respectively. At the end of the measurement sequence the ball was forced into contact with the coverslip, slightly deforming it by setting negative values of AFP on purpose (to about −2 µm), see Figure 3.2d, III.

The 3D positions of all fluorescent beads in the recorded z-stack were acquired using the PSF Extractor software (Daan B Boltje, Hoogenboom, Jakobi, Jensen, Jonker, Kaag, Koster, Last, Agrela Pinto, J. M. Plitzko, et al., 2022; Daan Benjamin Boltje et al., 2022) and the X, Y and Z locations of all fluorescent beads were extracted. From these, the position of the coverslip z_{CS} was determined by taking the median of the z positions of the beads on the cover slip and a least squares paraboloid fit on the coordinates of the beads residing on the ball surface was used to determine the lowest point of the ball z_B. These z positions are plotted against the set depth z_S in Figure 3.2e for the ball (black) and coverslip (red). Around 5.5 µm the ball and coverslip make contact, effectively deforming the coverslip at lower set depths. The coverslip position was subtracted from the lowest point of the ball ($z_N = z_B - z_{CS}$) and plotted against (z_S), see Figure 3.2f (top). A piece wise linear function of the form

$$z_N(z_S) = \begin{cases} z_{N0}, & \text{if } z_S \leq z_{S0} \\ z_{N0} + (z_S - z_{S0})/m, & \text{otherwise} \end{cases}$$

is used to determine the offset z_{N0} between coverslip and ball, the inflection point z_{S0} and the slope of the curve m. The fit is performed using a Levenberg-Marquardt non-linear least squares algorithm. We fit the data from −2 to 20 µm around the inflection point, and pass the measured values to the uncertainty parameter *sigma* in SCIPY.OPTIMIZE.CURVE_FIT (Virtanen et al., 2020). This artificially increases the uncertainty with increasing depth, and ensures that the inflection point can be found reproducibly for all datasets. The fit values are used to calculate the AFP for each set depth $z_A = z_S - z_{N0} + mz_{S0}$. The result is shown in Figure 3.2f (bottom), where the observed nominal depth z_N versus the actual depth z_A is plotted, from which the re-scaling factor ($\zeta = z_A/z_N$) was computed.

Re-scaling of 3D microscopy data

To demonstrate and test the re-scaling of 3D microscopy data, we recorded z-stacks of fluorescent beads embedded in an agarose hydrogel for $n_1 < n_2$, $n_1 = n_2$ and $n_1 > n_2$, where the $n_1 = n_2$ case serves as a ground truth for the re-scaling of the mismatched cases. To prepare the sample, we first coated a cover slip with fluorescent beads (190 nm, excitation 480 nm, emission 520 nm, Bangs Labs #FSDG002) by dropcasting from isopropyl alcohol (IPA). Next, an agarose gel was prepared (2w%) by mixing Milli-Q water and agarose (Low EEO, Fisher Scientific) and heating to boil in a microwave. 25 µL of the same beads in IPA were added to 225 mL agarose gel while warm. The mixture was pipetted into a glass sample cell composed of a microscope slide to which two small pieces of microscope slide as spacers were glued (using Norland 81 optical adhesive) roughly 0.5 cm apart, on top of which a #1.5 cover slip (180 µm thickness) was glued. After filling the cell with the agarose gel containing the beads, the cell was sealed with optical adhesive. After each gluing step, the sample was cured by exposure to UV light (~350 nm) for 90 s, and during the last curing step the beads were protected using a piece of aluminum foil.

Confocal z-stacks of the same volume were repeatedly recorded with different objectives using a Nikon C2-SHS C2si confocal on a Nikon Eclipse Ti inverted microscope with a 488 nm excitation laser. If the microscope objective had a correction collar, we optimized its position to minimize spherical aberrations while inspecting beads on the cover slip before the recording of the z-stack. We used the following procedure to record the z-stacks (with a 500 nm z step size). On the back of the sample (i.e. the side of the microscope slide) a spot was drawn using a felt marker. We then imaged this spot in bright field using a 10×/0.4 NA air objective and chose a reference feature in this spot to find back the same position in the sample. Next, we switched to the 100×/1.4 NA oil objective, and recorded a confocal z-stack including the cover slip interface. We then removed the immersion liquid from the sample, and found the same position again using the 10×/0.4 air objective. At this position, we again recorded a z-stack, but now with the 100×/0.85 NA air objective. Finally, we recorded at the same position a (ground truth) z-stack using a 40×/1.25 NA water objective. For single bead comparison, we cropped volumes in the three stacks comprising the same beads in the ground truth (water immersion) stack and the axially deformed stacks (air, oil immersion). We determined the cover-slip-to-sample interface as the intensity peak of the beads deposited on the cover slip and cropped the z-stack above the cover slip.

Re-scaling of the data was done either using the linear theories (Carlsson, 1991; Diel et al., 2020; Lyakin et al., 2017; Stallinga, 2005) where the voxel size in z was simply corrected, or using the depth-dependent re-scaling. For the latter, the AFP of each slide in the stack was calculated using equation 3.8, with the Lyakin scaling factor as the critical value. Next, a linear z-stack was generated with a z step size corresponding to the original stack and a range corresponding to the final AFP. The intensities in this z-stack were interpolated (using inverse distance weighting) from

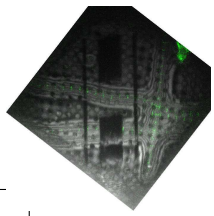

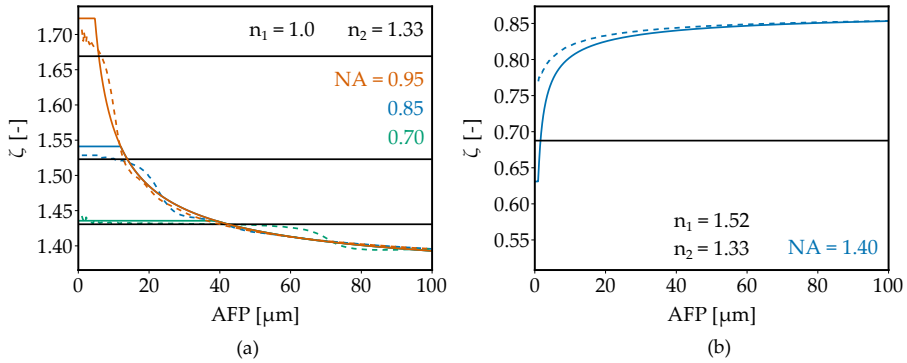

Figure 3.3: Axial re-scaling factor ζ versus AFP for different NAs and RIM contrasts, obtained through analytical expression Equation 3.3 (colored solid) and as calculated using wave-optics (colored dashed). For each NA the re-scaling factor as calculated by Lyakin *et al.* is included as a black solid line (Lyakin et al., 2017). (a) ζ as a function of AFP for NAs of 0.95, 0.85 and 0.70 at $n_1 = 1.0$ and $n_2 = 1.33$. (b) ζ as a function of AFP for an NA of 1.4 at $n_1 = 1.52$ and $n_2 = 1.33$.

the two nearest slices in the (non-linear) AFP z-stack. A Jupyter Notebook to perform the linear and non-linear re-scaling is available at (Wee et al., 2023).

Refractive index measurements

The refractive indices of the immersion oils used in this study were measured using an Abbe refractometer (Atago 3T). The indices were measured at $T = 25$ °C and at a wavelength $\lambda_D = 589.3$ nm. Using a measured dispersion value, the indices were converted using Cauchy's relation to $\lambda = 520$ nm (Jenkins, 1976). This resulted in the following refractive indices: $n^{25}_{520} = 1.5197$ (Type DF immersion oil, Cargille) and $n^{25}_{520} = 1.3421$ (Immersol^{TM} W 2010 immersion oil, Zeiss).

3.4 VALIDATION THROUGH WAVE-OPTICS CALCULATIONS

We first validate the derived analytical expression, by comparing it to wave-optics calculations, performed as described in Section 3.3. This is shown in Figure 3.3a and b respectively for RIM contrasts of $n_1 = 1.0 \rightarrow n_2 = 1.33$ and $n_1 = 1.52 \rightarrow n_2 = 1.33$. The axial re-scaling factor ζ is plotted versus depth, as obtained through analytical expression Equation 3.3 (colored solid) and as calculated using wave-optics (colored dashed).

For $n_1 < n_2$ (Figure 3.3a) the re-scaling factor increases at shallow depths, where the re-scaling (constant) maximum is determined by the numerical aperture of the optical system (i.e. the z_A-independent value of ζ_{crit}). At increasing depths it levels towards the n_2/n_1 limit, following the universal (i.e. NA-independent) curve ζ_{univ}. The wave-optics calculations deviate from the analytical expression due to some

oscillations remaining after data processing of the computed 2D PSFs. Despite this, they follow the general trend in the NA-independent regime (ζ_{univ} in Equation 3.3) for the different NAs plotted. At shallow depths, the plateau from the analytical expression (ζ_{crit} in Equation 3.3) is reproduced by the wave-optics calculations, though the exact re-scaling factor value fits between the analytical expression and the re-scaling factor as calculated by Lyakin *et al.* (Lyakin et al., 2017).

In the case of $n_1 > n_2$ (Figure 3.3b) the re-scaling factor as given by Equation 3.3, decreases at shallow depths, also reaching a plateau value determined by the numerical aperture. For this RIM contrast the plateau is very small, yielding a fast changing re-scaling factor in the first 10 µm after the refractive index interface. Imaging deeper, the re-scaling factor again levels towards the n_2/n_1 limit. The wave-optics calculations show less extreme axial scaling at shallow depths, while we find good agreement for depths > 15 µm.

3.5 VALIDATION THROUGH EXPERIMENTS

Five different objective lenses are used to measure depth-dependent axial re-scaling factors as explained in Section 3.3, varying in numerical aperture, immersion refractive index n_1 and magnification. Immersol^{TM} W 2010 immersion oil (Zeiss, $n_{520}^{25} = 1.3421$) and Type DF immersion oil (Cargille, $n_{520}^{25} = 1.5197$) were used in experiments. We will first discuss two cases in detail below, $n_1 = 1.0 \rightarrow n_2 = 1.34$ for a NA of 0.85 and $n_1 = 1.52 \rightarrow n_2 = 1.34$ for a NA of 1.4. For the other cases listed in Table 3.1, figures are presented in Supplement 1 and will be discussed afterwards.

$NA = 0.85$, $n_1 = 1.0$, $n_2 = 1.34$

In Figure 3.4, the axial re-scaling factor ζ is plotted against the actual depth z_A. The measurements (solid blue dots) are plotted alongside the wave-optics calculations (dashed blue lines), analytical solution (solid black lines) and literature theories (solid colored lines). From our individual sets of measurement data, the mean (solid black dots) is computed by binning along z_A, plotted in the center of each bin (bin sizes of 1 and 10 µm respectively for 0 to 10 µm and 10 to 100 µm). We estimate an upper error limit of $(100\,\text{nm}/z_N + 100\,\text{nm}/z_A)\zeta$, in determining the various z positions, composed of errors from: (i) positioning of the piezo stages, (ii) determining the position of ball and coverslip by fluorescent bead localization, and (iii) fitting uncertainties in the landing curve. The total measured error for the re-scaling factor (shaded blue area) is the sum of the rolling standard deviation of the measurements and the upper error limit. It increases significantly at shallow depths, which is confirmed by acquiring data without RIM present, and applying the same data analysis as shown in Figures S4 and S10.

Results are shown for a RIM contrast of $n_1 = 1.0 \rightarrow n_2 = 1.34$ in Figure 3.4, where the uncertainty in the measurement data increases at shallow depths, while at

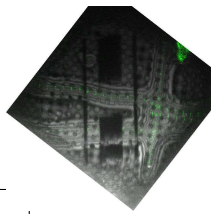

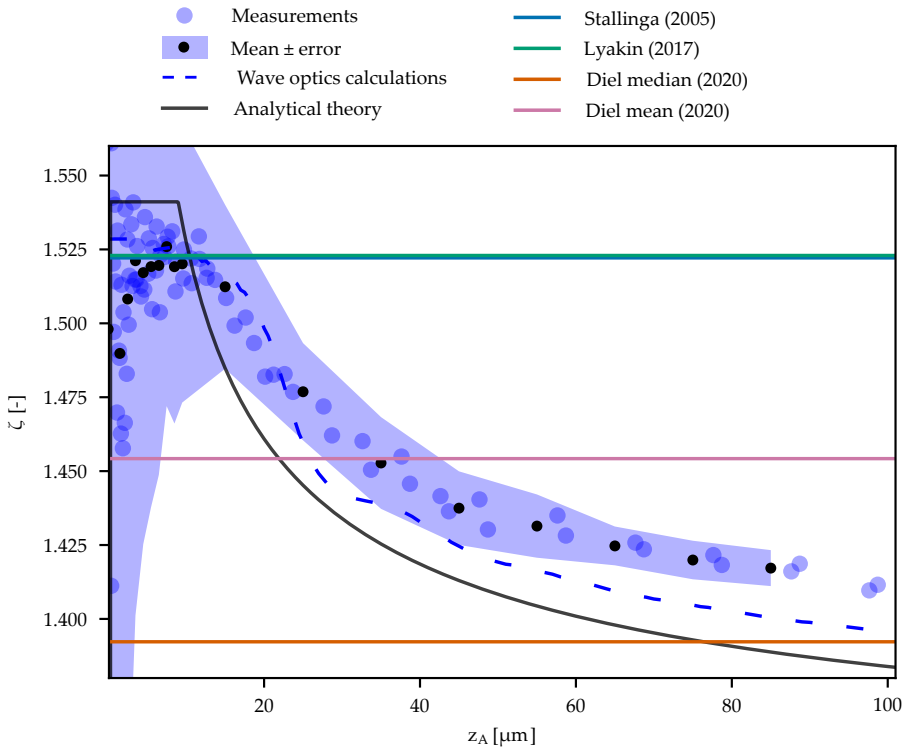

Figure 3.4: Axial re-scaling factor ζ versus AFP for an NA of 0.85, imaging under a RIM contrast of $n_1 = 1.0 \rightarrow n_2 = 1.34$. Measurement data (solid blue dots) are plotted alongside the wave-optics calculations (dashed blue lines), analytical solution (solid black lines, Equation 3.3) and depth-independent theories (solid lines). Two sets of measurement data are plotted individually and from this data the mean (solid black dots) is computed by binning along z_A, plotted in the center of each bin (bin sizes of 1 and 10 µm respectively for 0 to 10 µm and 10 to 100 µm). The measurement error (shaded blue area) is the sum of the measurements standard deviation and an estimated upper error limit.

larger depths the measurements capture the decay of the re-scaling factor but are slightly higher than the wave-optics calculations and analytical theory. Although we have taken care to align the optical system, we do expect some misalignment and/or residual optical aberrations to be the cause of this deviation. Especially, residual spherical aberration induced by a non-perfect correction collar setting could influence the measurements.

Looking at the exact value of the plateau at shallow depths, the analytical expression overestimates the re-scaling factor compared with the measurements and wave-optics calculations. In fact, both re-scaling factors from Lyakin and Stallinga give better agreement with the measured data (Lyakin et al., 2017; Stallinga, 2005) and in practical terms seems to provide a better value for ζ_{crit}. At extreme depths of $z_A = 10\,\text{mm}$ the depth-dependent re-scaling factor approaches the $n_2/n_1 = 1.34$ limit set by Carlsson *et al.* (not shown in Figure 3.4) (Carlsson, 1991). At more realistic imaging depths of 100 µm, the median from Diel coincides with the depth-dependent re-scaling factor and their mean gives a good agreement at $z_A = 40\,\mu\text{m}$.

$NA = 1.4$, $n_1 = 1.52$, $n_2 = 1.34$

In Figure 3.5, the axial re-scaling factor ζ is plotted against the actual depth z_A. We find good agreement between measurement data and the analytical theory when imaging under a RIM contrast of $n_1 = 1.52 \rightarrow n_2 = 1.34$, as show in Figure 3.5. The measurements presented agree with the analytical theory and only start to drop more at shallow depths ($< 4\,\mu\text{m}$). The relative error when approaching $z_A = 0$ increases for z_A and z_N as the error in both is affected by determining the point at which the sapphire ball touches the coverslip. We have also included re-scaling factors as measured by Petrov *et al.* where they use a method with a much smaller measurement errors (see also inset) (Petrov et al., 2020). Combining the measurement data from Petrov at shallow depths, and our own measurements data at larger depths, we find very good agreement with the analytical theory presented. Although the analytical expression provides a plateau for the re-scaling factor $\zeta_{\text{crit}} = 0.64$, this is not reproduced in the measurement data from Petrov.

Our wave-optics calculations also match the analytical theory at larger depths, but deviate below $z_A = 4\,\mu\text{m}$. At the same time, they do overlap with wave-optics calculations from Egner & Hell (Egner et al., 2006). At these shallow depths, an offset of a few tens of nanometers in the NFP has a dramatic effect on the re-scaling factor and hence super-critical angle fluorescence (SAF) effects are significant (Siemons et al., 2022). Although SAF is not included in the analytical derivation, it is considered in the wave-optics calculations through the Fresnel transmission coefficients when using the vector PSF model. The axial deformation is, however, enhanced by SAF, as the NFP shifts <40 nm away from the objective (Siemons et al., 2022). Therefore, the difference in the re-scaling factor between the wave-optics calculations and the analytical theory has already been reduced by the incorporation of SAF in the calculations.

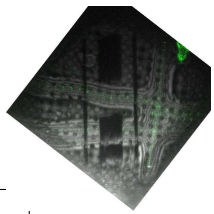

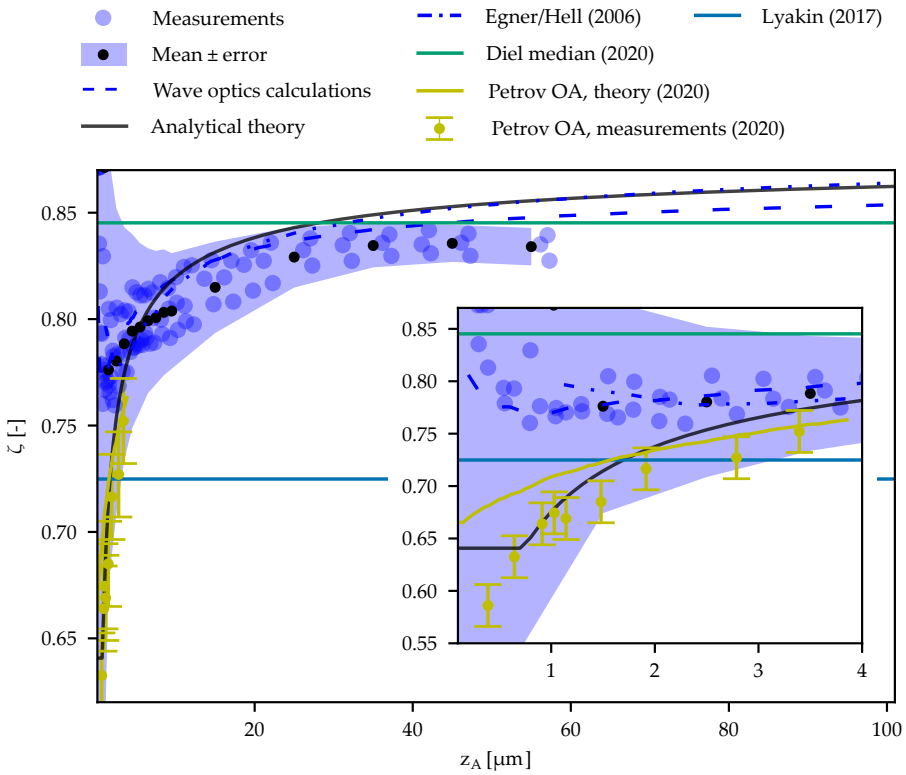

Figure 3.5: Axial re-scaling factor ζ versus AFP for an NA of 1.4, imaging under a RIM contrast of $n_1 = 1.52 \rightarrow n_2 = 1.34$. Measurement data (solid blue dots) are plotted alongside the wave-optics calculations (dashed blue lines), analytical solution (solid black lines, Equation 3.3) and depth-independent theories (solid lines). Three sets of measurement data are plotted individually and from this data the mean (solid black dots) is computed by binning along z_A, plotted in the center of each bin (bin sizes of 1 and 10 µm respectively for 0 to 10 µm and 10 to 100 µm). The measurement error (shaded blue area) is the sum of the measurements standard deviation and an estimated upper error limit. Measured data and theory as presented by Petrov *et al.* and wave-optics calculations from Egner & Hell are included (Egner et al., 2006; Petrov et al., 2020).

Up to depths of $z_A = 1\,\mu\text{m}$, there is a ~250 nm difference in the NFP found between $\zeta = 0.64$ (analytical theory) and $\zeta = 0.78$ (wave-optics calculations). This is too large to be caused by the chosen method of determining the focal position (i.e. maximum axial intensity (Egner et al., 2006) vs. minimal lateral width (Petrov et al., 2020)). As such, we do not have a fitting explanation for the discrepancy between the wave-optics calculations and the analytical theory along with measurements from Petrov *et al.*.

Other imaging scenarios

The measurement data for the remaining cases listed in Table 3.1, are shown in Figures S1 through S11, where the re-scaling factor ζ is plotted against z_A, alongside the wave-optics calculations, analytical solution and depth-independent theories. For each objective lens used we acquired data without a refractive index mismatch present and applied the same data analysis procedures as for axially scaled measurements (Figures S1, S4, S6, S9, S10). In all cases, the spread in the measurement data increases below $z_A = 10\,\mu\text{m}$ as uncertainties in determining both z_A and z_N increase. At higher depths, no reproducible deviations away from $\zeta = 1.0$ are found in these data, and we note a maximum error of about 2 % in the measurements. The data shown in Figure S9 is of special interest where we have used a water immersion objective to verify our measurement method and analysis when having immersion oil ($n = 1.34$) present between the coverslip and sapphire ball. We find a mean re-scaling factor of 0.99 ± 0.05 (standard deviation) over the entire depth range, and apart from the increased scatter near $z_A = 0$, the re-scaling factor remains approximately constant ($\zeta = 1.0$) as a function of depth for each individual dataset.

The objective lens with the lowest numerical aperture which we used in our measurements had a NA of 0.7, of which the results are presented in Figure S2 and S3 ($n_1 = 1.0 \rightarrow n_2 = 1.34$ & $n_1 = 1.0 \rightarrow n_2 = 1.52$). In both cases, the wave-optics calculations reproduce the analytical expression, while the measurements only reproduce the general trend for higher RIM contrast of $n_1 = 1.0 \rightarrow n_2 = 1.52$. In the case of $n_1 = 1.0 \rightarrow n_2 = 1.34$, the measurement uncertainties obscure a clear trend in the measurement data.

The RIM of $n_1 = 1.0 \rightarrow n_2 = 1.52$ for the 0.85 NA objective lens is shown in Figure S5. Both the wave-optics calculations and measurement data reproduce the behavior of the re-scaling factor as predicted by the analytical expression. Comparing against the measurement data, Lyakin and Stallinga again provide the best critical value ζ_{crit}.

In the case of the 0.95 NA air objective (Figures S7 and S8), again the wave-optics calculations reproduce the analytical expression over the entire depth range. For the measured data however, the trend of the NA independent regime $\zeta_{\text{universal}}$ is reproduced, but the measurements fail to replicate the strong increase to the plateau given by ζ_{crit} below $z_A = 20\,\mu\text{m}$. Along with depth-dependent re-scaling being more prominently present with increasing NA, so is the sensitivity to any remaining (i.e.

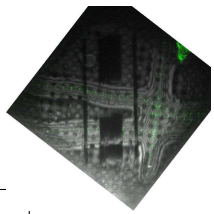

spherical or tilt) aberrations in the optical setup. We have taken care to minimize these, but we estimate that residual aberrations lower the effective NA, obscuring the rise to the plateau in the measurements.

For the 1.4 NA oil immersion objective, we present the RIM case of $n_1 = 1.52 \rightarrow n_2 = 1.0$ in Figure S11. Again the general depth-dependent behavior is reproduced in the measurements, but the re-scaling factor is underestimated at the coverslip while it is overestimated when imaging deeper into the sample.

3.6 AXIAL RE-SCALING OF 3D MICROSCOPY DATA

To test axial re-scaling of 3D microscopy data using our depth-dependent theory, we recorded confocal z-stacks of beads suspended in an agarose hydrogel, from the cover slip to 100 µm depth (z_N). These z-stacks were recorded using the 100×/0.85 NA air, 40×/1.25 NA water and 100×/1.4 oil objectives (see Table 3.1). As the refractive index of the agarose gel ($n_2 = 1.3356$ (Fujiwara et al., 2020)) is very close to the refractive index of the immersion medium of the water objective, we can use these z-stacks as a ground truth for the axial re-scaling of the data. We recorded the z-stacks at the exact same location in the sample to allow for direct comparison of the same beads in different imaging scenarios.

$n_1 < n_2$

The case $n_1 < n_2$ is particularly relevant for cryo-fluorescence microscopy where air immersion is used to observe a frozen or vitrified sample. Thus, we evaluate a typical situation with NA = 0.85, $n_1 = 1.0$ and $n_2 = 1.336$ (Daan B Boltje, Hoogenboom, Jakobi, Jensen, Jonker, Kaag, Koster, Last, Agrela Pinto, J. M. Plitzko, et al., 2022). Before re-scaling the data, we quantitatively compare the re-scaling factors of the depth-dependent and linear theories, as plotted in Figure S12. As we have found that the theories of Lyakin and Stallinga result in approximately equal re-scaling factors, we choose to plot only the Lyakin re-scaling factor. As the critical value of the depth-dependent re-scaling factor, we use the Lyakin re-scaling factor. Therefore, the depth-dependent re-scaling factor is 1.532 close to the cover slip and falls off to ~1.4 deeper into the sample (see Figure S12a). When plotting the focal shift Δf as a function of depth (AFP) we see that depth-dependent focal shift equals the Lyakin focal shift close to the cover slip and gradually transitions to the Diel (median) focal shift at larger depth (see Figure S12b).

To see how significant the difference between the theories is for this imaging scenario, we plot the absolute and relative difference between the depth-dependent and linear theories as function of depth (AFP). Figure S12c shows that for Lyakin the difference is obviously zero near the cover slip, but quickly increases to a large difference (>1 µm) after a depth of >25 µm. On the other hand, Diel (median) differs significantly (~1 µm) at a depth of 20 µm, but is the linear theory with the smallest

relative difference at >50 µm depth. Finally, Diel (mean) is in between the other two linear theories, having a smaller difference close to the cover slip than Diel (median), and a smaller difference at large depth than Lyakin. Where the relative difference between the depth-dependent theory and the theories of Lyakin and Diel median can exceed 5 %, the relative difference for the Diel mean theory is below 3 % (see Figure S12d).

Figure 3.6 shows the re-scaling of the 3D microscopy data of beads in an agarose hydrogel with NA = 0.85, $n_1 = 1.0$ and $n_2 = 1.336$. Overlays are plotted of the re-scaled z-stacks (grays) and the ground truth z-stack recorded with the water immersion objective (reds). As $n_1 < n_2$, the recorded z-stack was stretched in the axial direction to return to the ground truth axial distances. Deep into the sample ($z_A \approx 90\,\mu$m), Diel (mean) shows the largest re-scaling error where the z-stack is overstretched, whereas the depth-dependent and Diel (median) re-scaling collapses onto the ground truth data, although the PSF is elongated in the axial direction due to spherical aberrations induced by the refractive index mismatch. Closer to the cover slip ($z_A \approx 20\,\mu$m), both the depth-dependent and Diel (mean) re-scaling overlap with the ground truth z-stack, whereas Diel (median) has a slight (absolute) error as the axial distances have not been stretched enough. This agrees with the re-scaling factors plotted in Figure S12.

$n_1 > n_2$

The case of $n_1 > n_2$ is relevant for oil immersion observation of samples in water. Thus, we here evaluate a typical situation with NA = 1.4, $n_1 = 1.52$ and $n_2 = 1.336$. We quantitatively compare the re-scaling factors of the depth-dependent and linear theories in Figure S13. As NA > n_2, we cannot use Diel (mean). The depth-dependent re-scaling factor equals the Lyakin re-scaling factor close to the cover slip, but surpasses the Diel (median) at $z_A \approx 30\,\mu$m. The same trend is seen in the focal shift Δf. In this imaging scenario, the axial positional difference between Lyakin and the depth-dependent re-scaling theory increases after a few micrometers in depth, resulting in a significant difference >6 %. While the absolute difference between Diel (median) and the depth-dependent theory is small close to the cover slip (<1 µm) and ~2 µm um at large depths, the relative error is large (~20 %) close to the cover slip and small at large depths (~2 %).

In Figure 3.7 the re-scaling of the 3D microscopy data is plotted. As $n_1 > n_2$, the recorded z-stack was compressed in the axial direction to return to the ground truth axial distances. At larger depth ($z_A \approx 65\,\mu$m), the depth-dependent re-scaling nicely coincides with the ground truth, whereas the axial distances in the Diel (median) re-scaling has been compressed too much (see second row). Closer to the cover slip ($z_A \approx 15\,\mu$m) the depth-dependent re-scaling again nicely coincides with the ground truth, but the Diel (median) re-scaling has been compressed too little.

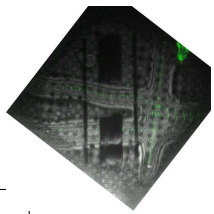

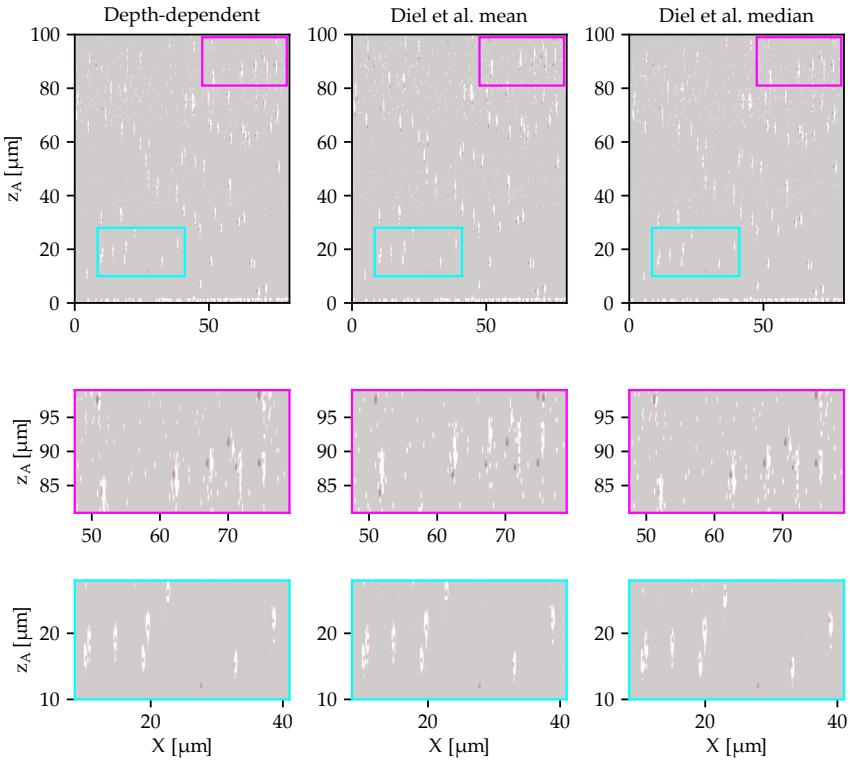

Figure 3.6: Axial re-scaling of 3D microscopy data with NA = 0.85, $n_1 = 1.0$, $n_2 = 1.336$ using the depth-dependent and linear theories. Maximum intensity projections along Y of the (re-scaled) confocal z-stack of beads embedded in an agarose hydrogel. The stacks have been re-scaled using the depth-dependent (left), Diel (mean) (middle) and Diel (median) (right) re-scaling factors. Overlays are plotted of the re-scaled z-stacks (grays) and the ground truth z-stack recorded with the water immersion objective (reds). The two bottom rows are cut-outs of the upper row, where the cut-outs at larger depths appear more noisy due to the intensity re-scaling due to fluorescence intensity loss at large depths. The beads are slightly displaced in X due to imperfections in the manual overlay of the z-stacks.

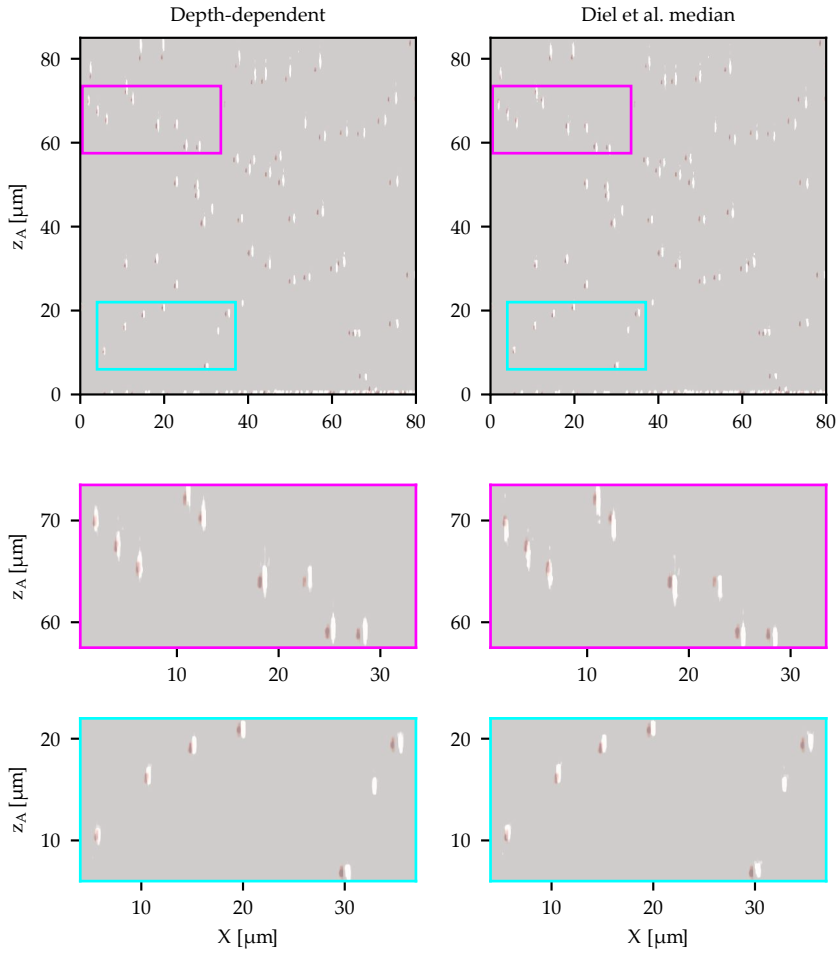

Figure 3.7: Axial re-scaling of 3D microscopy data with NA = 1.4, $n_1 = 1.52$, $n_2 = 1.336$. Maximum intensity projections along Y of the (re-scaled) confocal z-stack of beads embedded in an agarose hydrogel. The stacks have been re-scaled using the depth-dependent (left) and Diel (median) (right) re-scaling factors. Overlays are plotted of the re-scaled z-stacks (grays) and the ground truth z-stack recorded with the water immersion objective (reds). The two bottom rows are cut-outs of the upper row. The beads are slightly displaced in X due to imperfections in the manual overlay of the z-stacks.

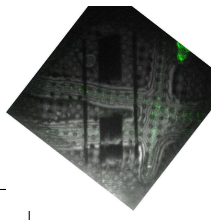

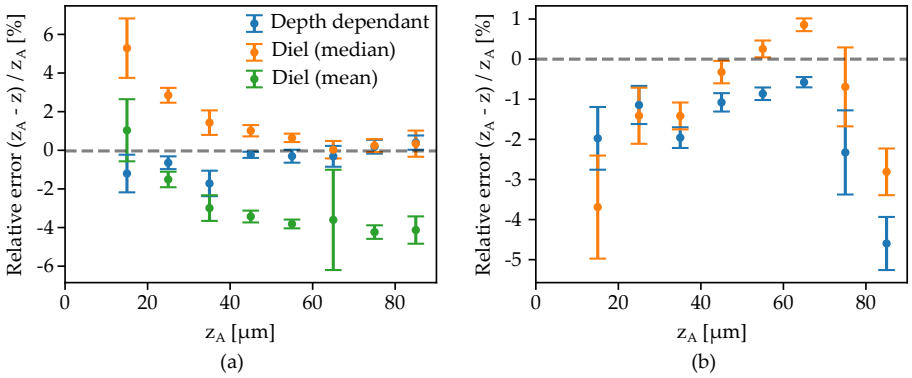

Figure 3.8: Relative error of the re-scaled z position compared to the ground truth z_A as recorded using a water immersion objective. The relative error is binned along z_A in bins of 10 µm and the mean of each bin is plotted in the center of each bin. The standard deviation is plotted as an error bar. The dashed gray line indicates 0 and acts as a guide to the eye.

Quantitative comparison

To quantify how well the acquired data can be corrected using the depth-dependant re-scaling factor, we localize all individual fluorescent beads present in the data recorded using the PSF-EXTRACTOR software (Daan Benjamin Boltje et al., 2022). We compare the z position found in the re-scaled data to the ground truth value z_A and divide this difference over z_A. This is shown in Figure 3.8 for both imaging scenarios, where we bin the data (bin size 10 µm), plot the mean of each bin along with the standard deviation as error bar, and plot the data centered with respect to the bin. In Figure 3.8a (NA = 0.85, n_1 = 1.0, n_2 = 1.336), we omit the first bin (0 to 10 µm) as it only contains 3 data points. The depth-dependent theory outperforms both Diel theories in the axial re-scaling of this data, where we note a maximum error of 2 % when using depth-dependent axial re-scaling, whereas the errors for the linear theories approaches 5 %.

The same analysis and data processing is done for NA = 1.4, n_1 = 1.52, n_2 = 1.336, to quantify the error in re-scaling using the Diel (median) and depth-dependent theory, see Figure 3.8b. There is not one theory that outperforms the others over the depths measured here. Still, the depth-dependent theory results in a smaller error closer to the cover slip, as is to be expected following Figure 3.5. In addition, this measurement did not include beads near the cover glass ($z_A < 20$ µm) where a relative difference up to 20 % between the two theories is expected (see Figure S13).

We should note that the objective lens used in this experiment did not have a correction collar. This means that we could not completely get rid of spherical aberration (SA) when imaging close to the cover slip. The presence of SA near the cover slip contradicts the optical conditions in the derivation of the analytical theory and therefore affects the legitimacy of the depth-dependent re-scaling factor, result-

ing in a higher re-scaling error. This shows that proper re-scaling also requires an optimization of the correction collar before the acquisition of the 3D microscopy data.

3.7 SOFTWARE FOR DEPTH-DEPENDENT RE-SCALING

Re-scaling acquired z-stacks using Python

To re-scale z-stack acquired under RIM, we have written PYTHON software which is available at `https://github.com/hoogenboom-group/SF` (Wee et al., 2023). Jupyter Notebooks are used to read image data and, based on the specific imaging conditions, use inverse distance weighting to rescale the intensities along the axial coordinate correctly. The same axial pixel size from the original data is used, but depending on the RIM mismatch, the re-scaled z-stack will map a shorter or larger axial range.

Interactive online tool for plotting the re-scaling factor versus imaging depth

We have made an online interactive tool where the depth-dependent re-scaling factor can be plotted and compared to existing depth independent scaling theories using PLOTLY DASH (Inc, 2023), the source code of which is available at (Wee et al., 2023). The code is accessible via the URL `https://axialscaling.pythonanywhere.com/`. The refractive indices n_1 and n_2, the NA and the wavelength λ can be varied. In addition, the focal shift Δf = can be plotted for the depth-dependent re-scaling factor, as well as for two depth independent scaling theories. Both the re-scaling factors and the focal shift resulting from the depth-dependent theory can be exported to file. All the measurement data and wave optics calculation results found in this manuscript and the accompanying supplemental materials are also included in the interactive plot.

3.8 DISCUSSION

The various re-scaling theories found in the literature can be understood as a result of different (overt or covert) assumptions on which maximum constructive interference contribution is leading. For example, Lyakin *et al.* used an analysis similar to ours, but explicitly sets the critical point θ^* such that $k'_z(\theta^*) = \frac{1}{2} \times (k'_z(0) + k'_z(\theta_{\max}))$ (Lyakin et al., 2017):

$$\zeta_{\text{Lyakin}} = \frac{n_1 + \sqrt{n_1^2 - \text{NA}^2}}{\sqrt{4\left(n_2^2 - n_1^2\right) + \left(n_1 + \sqrt{n_1^2 - \text{NA}^2}\right)^2}}. \tag{3.9}$$

The same value was proposed earlier by Stallinga while posing different criteria of minimal variation of the phase function: $\theta^* : \min \langle (\Phi - \Phi(\theta^*))^2 \rangle$ (Stallinga, 2005). For

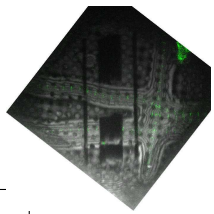

Diel *et al.* the ζ_{median} corresponds to setting $\theta^* : k_r(\theta^*) = 1/2 k_r(\theta_{\text{max}}) = \frac{1}{2} k_0 \times \text{NA}$ (Diel et al., 2020), such that

$$\zeta_{\text{median}} = \sqrt{\frac{n_2^2 - \frac{\text{NA}^2}{4}}{n_1^2 - \frac{\text{NA}^2}{4}}}. \tag{3.10}$$

These estimates for ζ are geometrical in nature, where the actual wavelength is not taken into account. This results in an implicit omission of the interference nature of the PSF under RIM. Somewhat less obviously, the criterion of Stallinga is also geometrical (Stallinga, 2005). While it does demand minimal variation in the value of Φ in order to achieve the highest possible constructive interference, it does not take into account that the well minimized phase function can become several 2π in range (when both z_A and z_N are large enough) and thus lead to destructive interference anyway.

In order to be able to correct for depth-dependent axial scaling in experiments where imaging under RIM is unavoidable, it is crucial that (i) the position of the coverslip (or more general, the RIM interface) is determined precisely and, (ii) spherical aberration at the interface is reduced to an absolute minimum by selecting the cover glass the objective is optimized for, or by optimizing the position of the correction collar. In practical terms, this would require that the objective lens used is fitted with a correction collar, which is often the case for high-NA objective lenses.

One such case would be cryo-fluorescence microscopy used in the cryo-electron tomography workflow, where a RIM is generally present due to the large temperature difference between the optical objective and the sample. With fluorescence microscopy, targets can be identified in frozen hydrated cells and consequently sufficiently thin sections can be prepared by ablating the excess cellular material surrounding the target with a focused ion beam (Chiang et al., 2007; Hylton et al., 2021; Villa et al., 2013). The aimed thickness of this frozen section is approximately 100 to 200 nm, which makes it crucial to precisely determine the target position with respect to the RIM interface (outer cell surface) (Vulović et al., 2013). If axially scaled distances measured with the light microscope are not corrected, targeting errors in the range of 300 to 1200 nm will occur with cell thicknesses ranging up to micrometers. Moreover, the *depth-dependence* of these errors will be important when fabricating sections out of thicker ice whilst using fluorescence microscopy to find targets in for instance organoids, as can be done in high pressure frozen samples (K. Kelley et al., 2022; Schiøtz et al., 2023).

With the provided software (Wee et al., 2023), one can easily plot the depth-dependent re-scaling factor for the relevant imaging scenario, but also re-scale their 3D microscopy data, without having to judge which linear theory will hold in this scenario or perform full wave-optics calculations. We should note, however, that although the data will be axially re-scaled, our software does not provide any correction of the shape of the point spread function (PSF) due to spherical aberrations. To

correct for this, one would require deconvolution with a depth-dependent PSF as demonstrated in (Kim et al., 2016).

Our measurements are limited by the relatively high uncertainty in determining the re-scaling factor near $z_A = 0$. It would therefore be interesting, for future research, to use the method from Petrov *et al.* to measure the re-scaling factor for the scenario with a 0.85 NA air objective when imaging $n_1 = 1.0 \rightarrow n_2 = 1.33$.

3.9 CONCLUSION

We have presented an analytical theory to correct for the depth-dependent axial deformation when imaging with light microscopy in the presence of a refractive index mismatch between the sample and the microscope objective immersion medium. Using the resulting equation, a re-scaling factor as a function of depth can be calculated from imaging parameters numerical aperture (NA), the refractive indices of the objective (n_1) and sample (n_2), and the wavelength (λ), for a RIM with both $n_1 < n_2$ and $n_1 > n_2$. We performed wave-optics calculations to verify the theory and find a very good agreement between the two. In addition, we performed experiments to measure the axial scaling, where we find a good agreement at larger depths, whereas closer to the cover slip, the measurements suffer from large uncertainties. We do find good agreement with the accurate measurements done by Petrov *et al.* (Petrov et al., 2020) in the case when imaging with a high-NA oil immersion objective into a water sample.

Next, we tested the depth-dependent theory versus existing linear theories in the literature on 3D microscopy data with a known ground truth. We find that for NA = 0.85, $n_1 = 1$, $n_2 = 1.33$ the depth-dependent theory outperforms existing linear theories for depths up to 80 µm with a maximum relative error of 2 %. For NA = 1.4, $n_1 = 1.52$, $n_2 = 1.33$, the depth-dependent theory performs as good as the best linear theory in literature. However, we think its performance was compromised by the presence of a small spherical aberration near the cover slip, which could not be corrected for as the objective did not have a correction collar. Moreover, we could not compare close to the cover glass (< 10 µm), where the linear theory used in the comparison was expected to break down.

Finally, we have presented a web applet to be used by microscope users to calculate the re-scaling factor for their imaging parameters. In addition, we have shared software to re-scale 3D data sets using the depth-dependent scaling factor.

Our re-scaling theory is the first to include the depth dependence of axial scaling due to a refractive index mismatch. It will be of use in imaging scenarios where the refractive indices of the sample and objective cannot be matched, such as in integrated, cryogenic, and correlative light and electron microscopy setups, or in the imaging of water-like samples using high-NA oil immersion objectives.

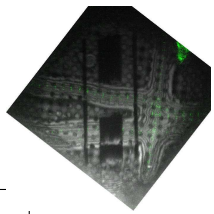

3.10 ACKNOWLEDGMENTS

We thank Hans C. Gerritsen and Gerhard A. Blab for the useful discussions, Bernd Rieger for feedback on our results and Alfons van Blaaderen for the use of the refractometer. This work is part of the Cryo3Beams project (project Nº 17152) financed via the High Tech Systems and Materials programme of the Applied and Engineering Sciences domain of the Dutch Research Council (NWO).

3.11 AUTHOR CONTRIBUTIONS

EBW did preliminary experiments and was overall the project supervisor. The derivation of analytical theory and verification through wave-optics calculations were done by SVL. The experimental design, work, and analysis for verification were done by DBB. MNFH and EBW carried out experiments for the axial re-scaling of 3D microscopy data. DBB, SVL and EBW wrote the manuscript with input from MNFH, and JPH. All authors discussed the results and commented on the manuscript.

3.12 DECLARATION OF COMPETING INTEREST

SVL, MNFH and EBW declare no conflicts of interest. DBB is employed by Delmic BV, JPH has a financial interest in Delmic B.V.

3.13 SUPPLEMENTAL INFORMATION

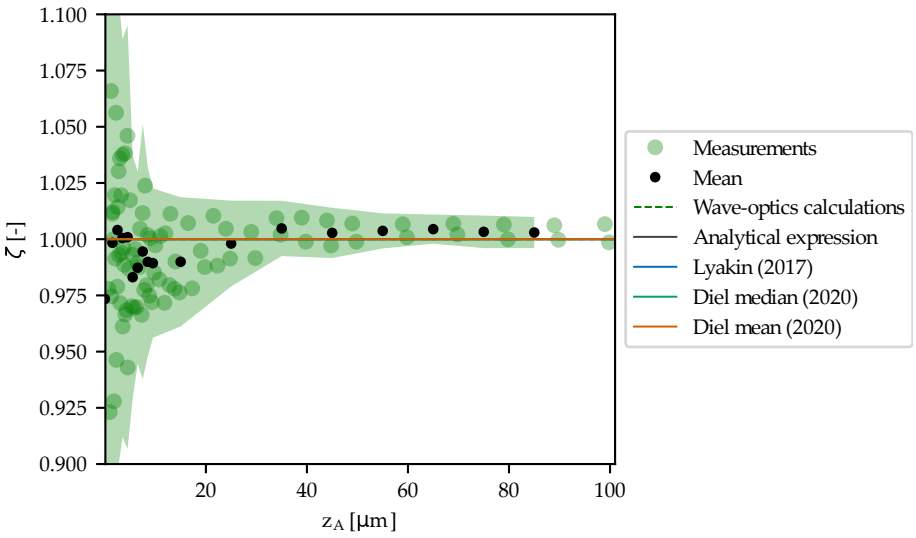

Figure S1: Re-scaling factor versus depth for 0.7 NA optical objective, $n_1 = 1.0$ and $n_2 = 1.0$. Measurement data (green dots) are plotted alongside the wave-optics calculations (dashed blue lines), analytical solution (solid black line) and depth-independent theories (solid lines). The wave-optics calculations, analytical solution and depth-independent theories overlap at $\zeta = 1.0$. 2 sets of measurement data are plotted individually and from this data the mean (solid black dots) is computed by binning along z_A, plotted in the center of each bin (bin sizes of 1 and 10 µm respectively for 0 to 10 µm and 10 to 100 µm). The measurement error (shaded green area) is the sum of the measurements standard deviation and an estimated upper error limit.

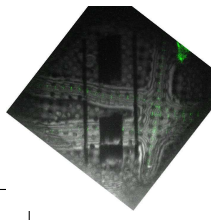

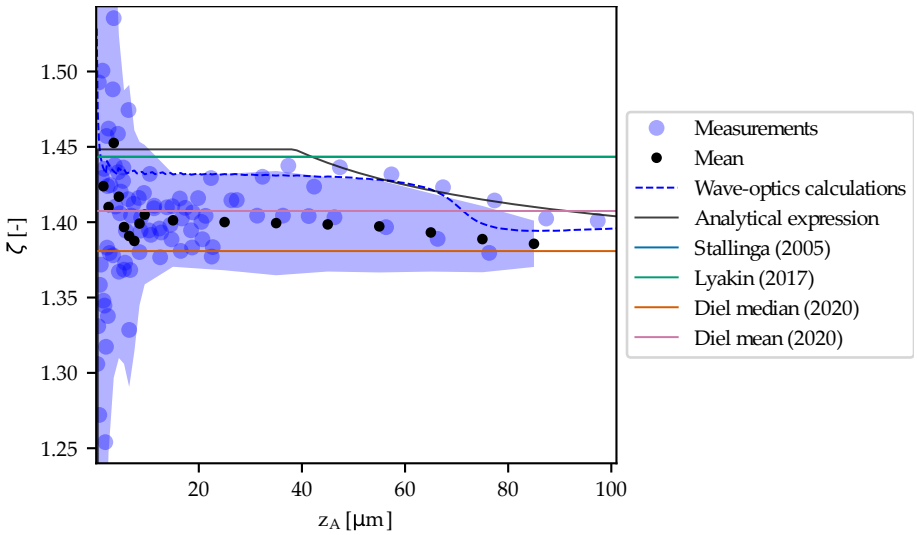

Figure S2: Re-scaling factor versus depth for 0.7 NA optical objective, $n_1 = 1.0$ and $n_2 = 1.34$. Measurement data (blue dots) are plotted alongside the wave-optics calculations (dashed blue lines), analytical solution (solid black line) and depth-independent theories (solid lines). 4 sets of measurement data are plotted individually and from this data the mean (solid black dots) is computed by binning along z_A, plotted in the center of each bin (bin sizes of 1 and 10 µm respectively for 0 to 10 µm and 10 to 100 µm). The measurement error (shaded blue area) is the sum of the measurements standard deviation and an estimated upper error limit.

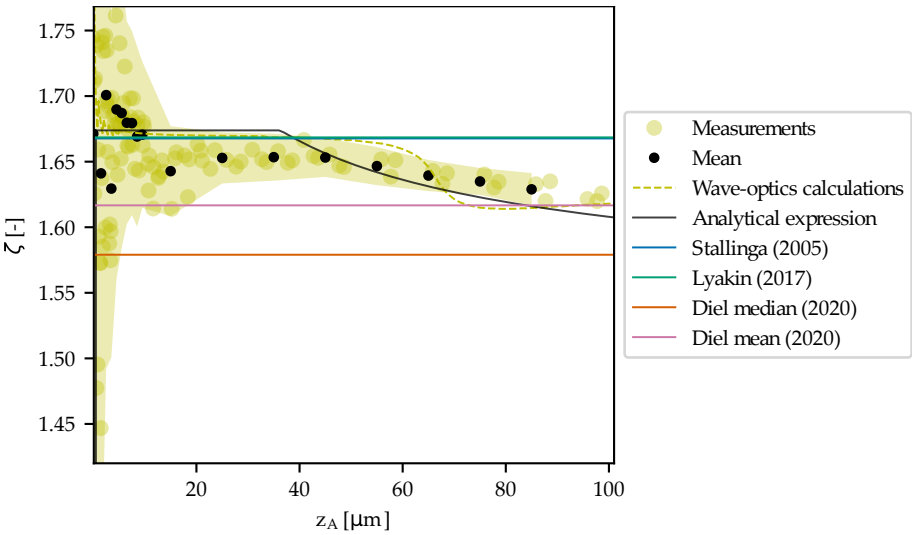

Figure S3: Re-scaling factor versus depth for 0.7 NA optical objective, $n_1 = 1.0$ and $n_2 = 1.52$. Measurement data (yellow dots) are plotted alongside the wave-optics calculations (dashed blue lines), analytical solution (solid black line) and depth-independent theories (solid lines). 3 sets of measurement data are plotted individually and from this data the mean (solid black dots) is computed by binning along z_A, plotted in the center of each bin (bin sizes of 1 and 10 µm respectively for 0 to 10 µm and 10 to 100 µm). The measurement error (shaded yellow area) is the sum of the measurements standard deviation and an estimated upper error limit.

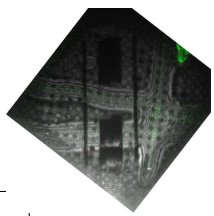

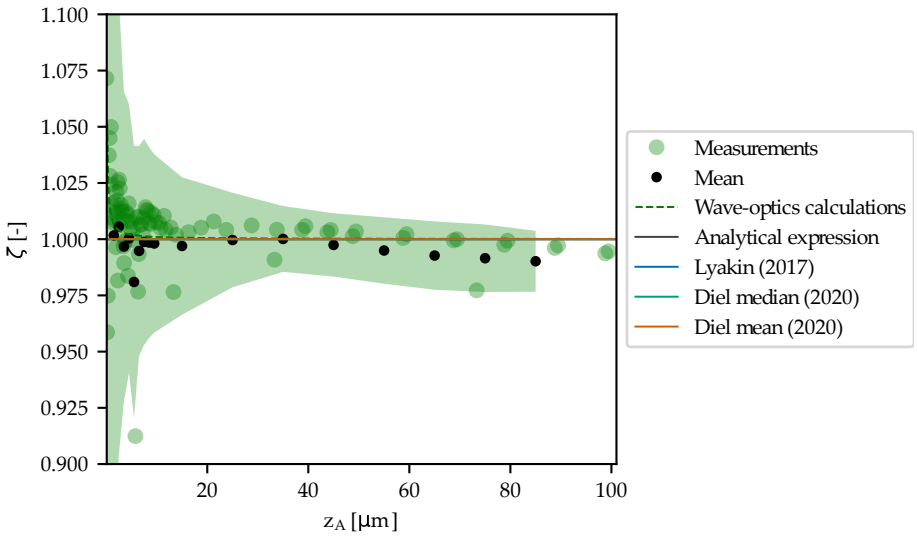

Figure S4: Re-scaling factor versus depth for 0.85 NA optical objective, $n_1 = 1.0$ and $n_2 = 1.0$. Measurement data (green dots) are plotted alongside the wave-optics calculations (dashed blue lines), analytical solution (solid black line) and depth-independent theories (solid lines). The wave-optics calculations, analytical solution and depth-independent theories overlap at $\zeta = 1.0$. 3 sets of measurement data are plotted individually and from this data the mean (solid black dots) is computed by binning along z_A, plotted in the center of each bin (bin sizes of 1 and 10 µm respectively for 0 to 10 µm and 10 to 100 µm). The measurement error (shaded green area) is the sum of the measurements standard deviation and an estimated upper error limit.

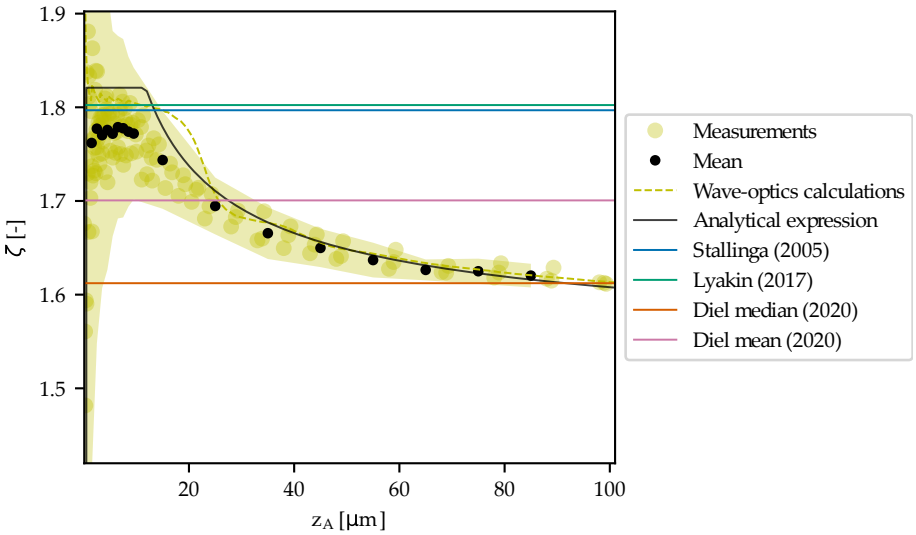

Figure S5: Re-scaling factor versus depth for 0.85 NA optical objective, $n_1 = 1.0$ and $n_2 = 1.52$. Measurement data (yellow dots) are plotted alongside the wave-optics calculations (dashed blue lines), analytical solution (solid black line) and depth-independent theories (solid lines). 3 sets of measurement data are plotted individually and from this data the mean (solid black dots) is computed by binning along z_A, plotted in the center of each bin (bin sizes of 1 and 10 µm respectively for 0 to 10 µm and 10 to 100 µm). The measurement error (shaded yellow area) is the sum of the measurements standard deviation and an estimated upper error limit.

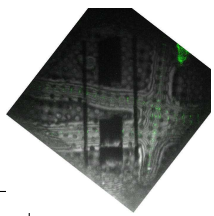

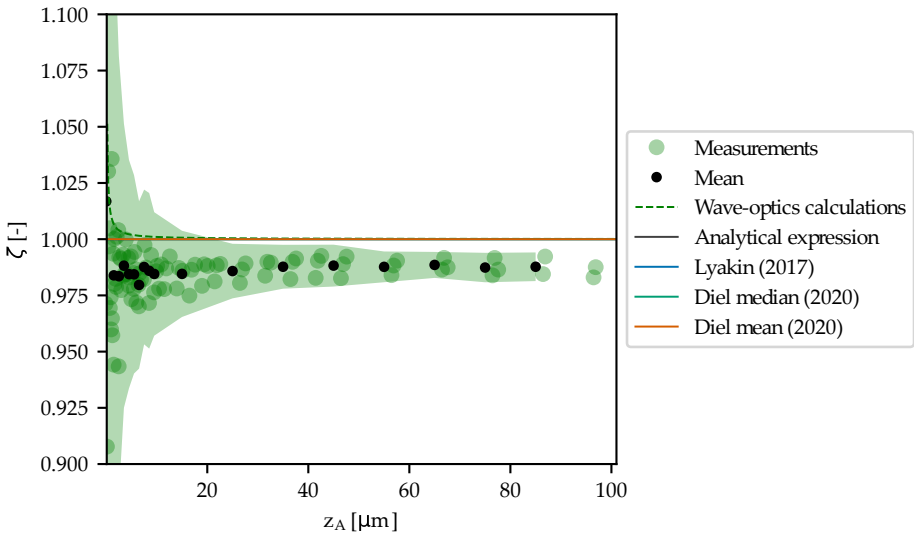

Figure S6: Re-scaling factor versus depth for 0.95 NA optical objective, $n_1 = 1.0$ and $n_2 = 1.0$. Measurement data (green dots) are plotted alongside the wave-optics calculations (dashed blue lines), analytical solution (solid black line) and depth-independent theories (solid lines). The wave-optics calculations, analytical solution and depth-independent theories overlap at $\zeta = 1.0$. 3 sets of measurement data are plotted individually and from this data the mean (solid black dots) is computed by binning along z_A, plotted in the center of each bin (bin sizes of 1 and 10 µm respectively for 0 to 10 µm and 10 to 100 µm). The measurement error (shaded green area) is the sum of the measurements standard deviation and an estimated upper error limit.

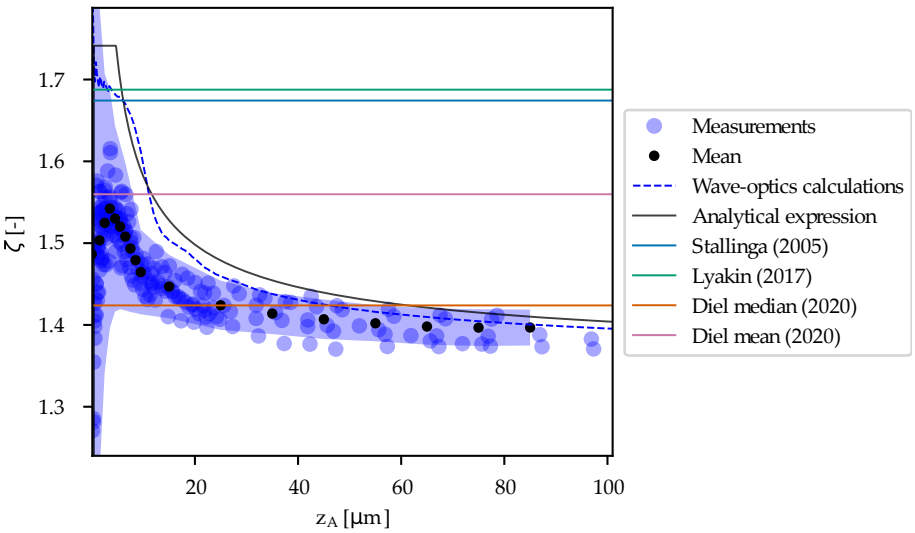

Figure S7: Re-scaling factor versus depth for 0.95 NA optical objective, $n_1 = 1.0$ and $n_2 = 1.34$. Measurement data (blue dots) are plotted alongside the wave-optics calculations (dashed blue lines), analytical solution (solid black line) and depth-independent theories (solid lines). 9 sets of measurement data are plotted individually and from this data the mean (solid black dots) is computed by binning along z_A, plotted in the center of each bin (bin sizes of 1 and 10 µm respectively for 0 to 10 µm and 10 to 100 µm). The measurement error (shaded blue area) is the sum of the measurements standard deviation and an estimated upper error limit.

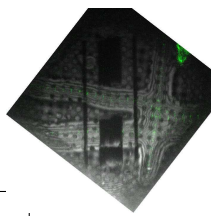

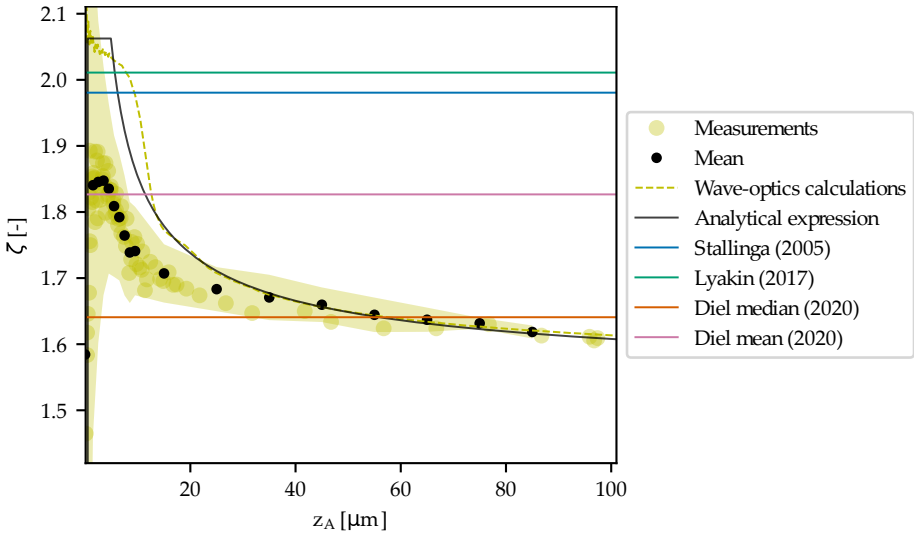

Figure S8: Re-scaling factor versus depth for 0.95 NA optical objective, $n_1 = 1.0$ and $n_2 = 1.52$. Measurement data (yellow dots) are plotted alongside the wave-optics calculations (dashed blue lines), analytical solution (solid black line) and depth-independent theories (solid lines). 3 sets of measurement data are plotted individually and from this data the mean (solid black dots) is computed by binning along z_A, plotted in the center of each bin (bin sizes of 1 and 10 µm respectively for 0 to 10 µm and 10 to 100 µm). The measurement error (shaded yellow area) is the sum of the measurements standard deviation and an estimated upper error limit.

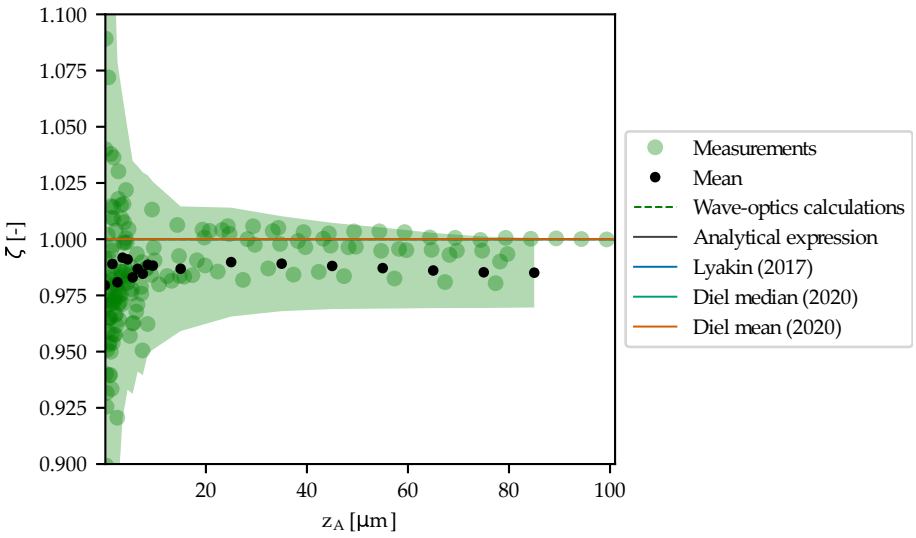

Figure S9: Re-scaling factor versus depth for 1.25 NA optical objective, $n_1 = 1.34$ and $n_2 = 1.34$. Measurement data (green dots) are plotted alongside the wave-optics calculations (dashed blue lines), analytical solution (solid black line) and depth-independent theories (solid lines). The wave-optics calculations, analytical solution and depth-independent theories overlap at $\zeta = 1.0$. 6 sets of measurement data are plotted individually and from this data the mean (solid black dots) is computed by binning along z_A, plotted in the center of each bin (bin sizes of 1 and 10 µm respectively for 0 to 10 µm and 10 to 100 µm). The measurement error (shaded green area) is the sum of the measurements standard deviation and an estimated upper error limit.

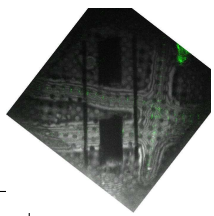

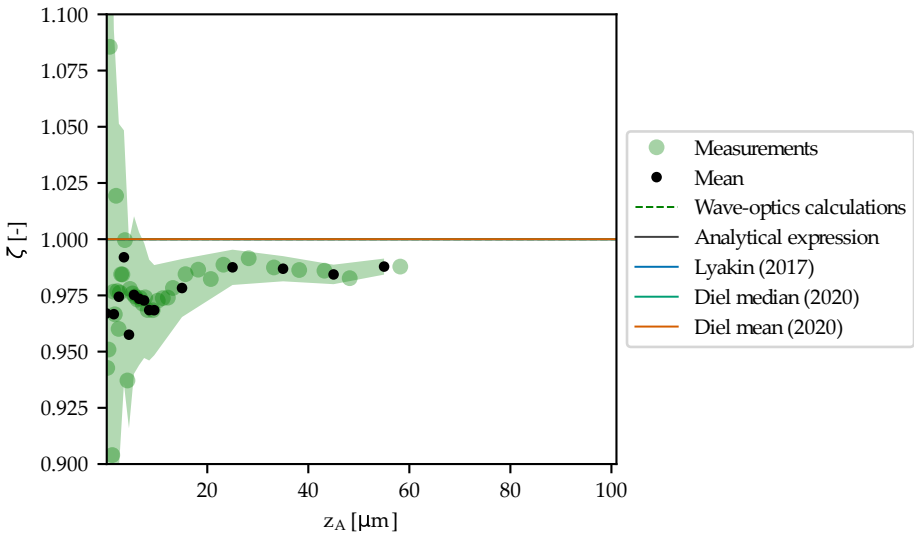

Figure S10: Re-scaling factor versus depth for 1.4 NA optical objective, $n_1 = 1.52$ and $n_2 = 1.52$. Measurement data (green dots) are plotted alongside the wave-optics calculations (dashed blue lines), analytical solution (solid black line) and depth-independent theories (solid lines). The wave-optics calculations, analytical solution and depth-independent theories overlap at $\zeta = 1.0$. 1 sets of measurement data are plotted individually and from this data the mean (solid black dots) is computed by binning along z_A, plotted in the center of each bin (bin sizes of 1 and 10 µm respectively for 0 to 10 µm and 10 to 100 µm). The measurement error (shaded green area) is the sum of the measurements standard deviation and an estimated upper error limit.

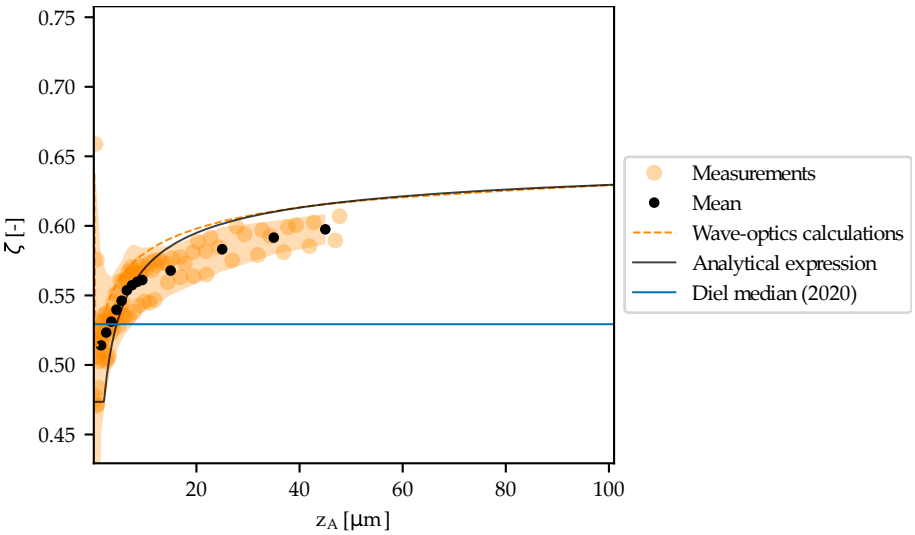

Figure S11: Re-scaling factor versus depth for 1.4 NA optical objective, $n_1 = 1.52$ and $n_2 = 1.0$. Measurement data (dark orange dots) are plotted alongside the wave-optics calculations (dashed blue lines), analytical solution (solid black line) and depth-independent theories (solid lines). 3 sets of measurement data are plotted individually and from this data the mean (solid black dots) is computed by binning along z_A, plotted in the center of each bin (bin sizes of 1 and 10 µm respectively for 0 to 10 µm and 10 to 100 µm). The measurement error (shaded dark orange area) is the sum of the measurements standard deviation and an estimated upper error limit.

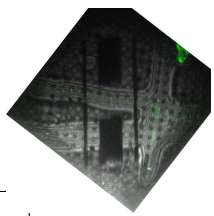

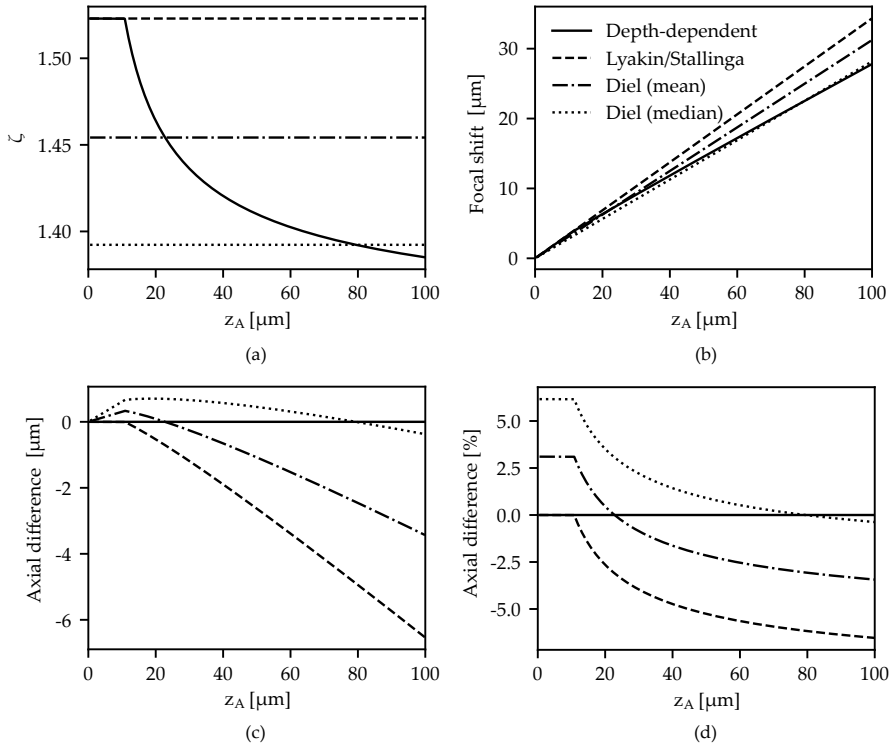

Figure S12: Quantitative comparison of the linear scaling theories from literature to the depth-dependent analytical theory for NA=0.85, $n_1 = 1.0$ and $n_2 = 1.336$. **(a)** The re-scaling factor ζ vs AFP for the depth-dependent theory (solid), Lyakin *et al.* (dashed) Lyakin et al., 2017, Diel *et al.* mean (dash-dot) and median (dot-dot) Diel et al., 2020. **(b)** The focal shift vs AFP of the aforementioned theories. **(d)** Axial difference vs AFP for the theories. **(d)** Relative difference between the theories.

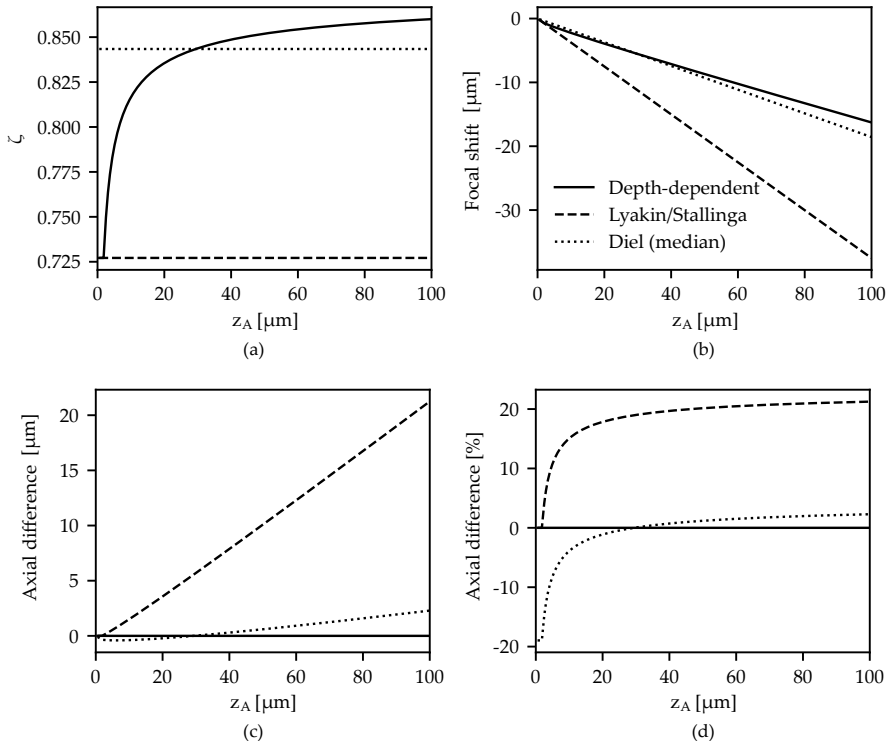

Figure S13: Quantitative comparison of scaling theories in case of NA = 1.4, $n_1 = 1.52$, $n_2 = 1.336$. **(a)** The re-scaling factor ζ vs AFP for the depth-dependent theory (solid), Lyakin *et al.* (dashed) Lyakin et al., 2017 and median (dot-dot) Diel et al., 2020. **(b)** The focal shift vs AFP of the aforementioned theories. **(d)** Axial difference vs AFP for the theories. **(d)** Relative difference between the theories.

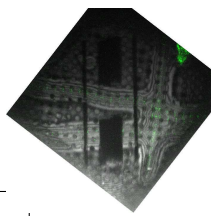

4

THICKNESS AND QUALITY CONTROLLED FABRICATION OF FLUORESCENCE-TARGETED FROZEN-HYDRATED LAMELLAE

Cryogenic FIB milling is essential for fabricating thin lamella-shaped samples out of frozen-hydrated cells for high-resolution structure determination. Structural information can only be resolved at high resolution if the lamella thickness is between 100 and 200 nm. While the lamella fabrication workflow has undergone significant improvements since its conception, quantitative, live feedback on lamella thickness, quality, and biological target inclusion is still lacking. Taking advantage of a coincident light microscopy integrated into the FIB-SEM, we present three different strategies that together allow accurate, live control during lamella fabrication. First, we combine 4D-STEM with FM targeting to determine the lamella thickness. Second, with RLM we screen target sites for ice contamination and monitor lamella thickness and integrity of the protective Pt coating during FIB milling. Third, we exploit thin-film interference to obtain fine-grained feedback on thickness uniformity below 500 nm. We finally present a full workflow for fluorescence-targeted and quality controlled fabrication of frozen-hydrated lamellae, benchmarked with excellent agreement to EFTEM measurements and reconstructed tomograms obtained with electron cryo-tomography.

4.1 INTRODUCTION

Cryogenic electron tomography (cryo-ET) has become an integral technique in the quest for a mechanistic understanding of complex biological processes at the molecular scale, as it remains the sole imaging method capable of discerning intricate structural features within a cell without labeling Tegunov et al., 2021; Turk et al., 2020; Zimmerli et al., 2021. However, its utility in gaining biological insights is often hampered by constraints in sample preparation, particularly the need for thin, ideally artifact-free, cellular sections. These thin sections can be fabricated out of frozen hydrated cells using a focused ion beam scanning electron microscope. In FIB-SEM grazing-incidence ion bombardment locally removes cellular material, revealing a cross-section of the cell's interior (lamella), which is then primed for high-resolution imaging with a TEM Chiang et al., 2007; Hylton et al., 2021; Rigort et al., 2012; Villa et al., 2013. To achieve optimal structural resolution, the ideal lamella thickness must be around 100 to 200 nm, remaining well below the inelastic mean-free path of electrons in vitreous ice, which is about 320 nm for TEM imaging at 300 keV (Yesibolati et al., 2020).

This chapter has been published as: Boltje et al. (2025). "Thickness and quality controlled fabrication of fluorescence-targeted frozen-hydrated lamellae." In: Cell Reports Methods, pp. 2025–01.

In recent years, various improvements and refinements have been made to the cryo-FIB milling workflow, enhancing throughput, reliability, sample yield, and quality. Gas injection systems (GISs) in the cryo-FIB microscope enable the deposition of a Pt layer, which protects the target region from ion exposure. Maintaining the integrity of this Pt layer during milling is crucial to obtain thin lamellae and prevent ion-induced damage. Different approaches to *in-situ* fluorescence imaging have been integrated into the cryo-FIB workflow to aid in selecting target cells and identifying regions of interest for milling Arnold et al., 2016; Daan B Boltje, Hoogenboom, Jakobi, Jensen, Jonker, Kaag, Koster, Last, Agrela Pinto, J. M. Plitzko, et al., 2022; Buckley et al., 2020; Gorelick et al., 2019; Kuba et al., 2021; W. Li et al., 2023; Schaffer et al., 2019; Smeets et al., 2021; Tacke et al., 2021; ThermoFisher Scientific, 2021; Wolff, Limpens, et al., 2019. However, precise localization of the target in cryo-FIB coordinates remains challenging due to registration errors and aberrations that result from refractive index mismatches during fluorescence microscopy Loginov et al., 2024. *In-situ* feedback during cryo-FIB milling on lamella quality—specifically its thickness and uniformity, the condition of the protective Pt layer, and the inclusion of the biological target—could significantly improve fabrication yield in the frozen-hydrated lamella workflow.

The lamella thickness and uniformity can be assessed using SEM Conlan et al., 2020; Mierlo et al., 2014. However, this method assumes the lamella is composed of a homogeneous material, which is not the case for cellular samples. Additionally, most methods require independent calibration before each imaging session and come with practical drawbacks Skoupỳ et al., 2023. Quantitative thickness estimations for cellular specimens have been reported when imaging the periphery of a cell in the TEM Last et al., 2023, but these have not been extended to the lamella fabrication workflow. Alternatively, using q4STEM imaging, we recently demonstrated that lamella thickness can be robustly estimated directly in the FIB-SEM without additional calibrations, provided the instrument setup allows for transmission imaging Skoupỳ et al., 2023.

Up to now, routine fabrication of sufficiently thin frozen-hydrated sections remains challenging due to a lack of direct, quantitative feedback on all key parameters that determine the lamellla quality: thickness, uniformity, ice contamination, state of the protective Pt GIS layer, and inclusion of the biological target.

Here, we utilize a coincident FM-FIB-SEM setup Daan B Boltje, Hoogenboom, Jakobi, Jensen, Jonker, Kaag, Koster, Last, Agrela Pinto, J. M. Plitzko, et al., 2022 for automated *fluorescence-targeted* lamella preparation and present three complementary techniques to estimate the thickness of a frozen-hydrated lamella during the milling process without requiring prior calibration. We (i) apply the previously presented q4STEM method to frozen-hydrated lamellae and benchmark the measured thickness against EFTEM, (ii) image the lamella from the foil side using RLM and estimate its thickness based on the known milling geometry, and (iii) exploit thin-film interference on a per-pixel basis, yielding a fine-grained thickness map of the lamella and providing quantitative feedback on lateral thickness variations.

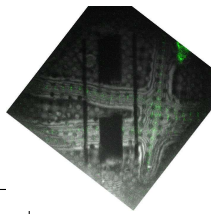

Furthermore, we address the axial scaling effects caused by the RIM during the selection of fluorescence microscopy targets and incorporate this correction into our approach for automated milling of fluorescent targets. Finally, we integrate all of these techniques to show a fluorescence-targeted lamella fabrication workflow with precise control over both lamella thickness and quality.

4.2 RESULTS

Fluorescent targeting under refractive index mismatch

In our three-beam coincident setup, cryo-fluorescence microscopy is used to identify targets in frozen-hydrated cells, after which surrounding material is ablated with the FIB to create a lamella containing the target. Due to the large temperature difference between the optical objective (at room temperature) and the sample held at 100 K, a dry objective lens ($n_1 = 1.0$) is used to image the cellular material, which primarily consists of vitrified water ($n_2 = 1.28$ at $T = 109$ K) Kofman et al., 2019. This creates a RIM, resulting in a depth-dependent deformation of the optical microscope's axial coordinate Loginov et al., 2024. Correctly accounting for the RIM induced axial deformation is crucial when fabricating lamellae around fluorescent targets embedded in frozen-hydrated cells.

To compensate for the axial compression caused by the RIM, the z-position of the interface between vacuum and specimen must be precisely determined. In our coincident three-beam microscope, the sample holder is oriented such that an incident angle of 10° is maintained with the FIB, and consequently, the SEM has an incident angle of 118°. The optical objective is positioned below the specimen and images the ROI at right angles through the EM grid, as shown in Figure 4.1a.

When an AutoGrid-mounted sample is loaded into the system, the correct height for three-beam coincidence is initially achieved by moving the objective lens to the coincident point of the FIB-SEM. To identify the z-position of the air-specimen interface, the objective stage is used to focus on the grid foil while avoiding ice in the optical path, thereby preventing a RIM. This ensures that the measured axial (microscope or nominal, z_N) position of the grid foil matches the actual position z_A (Figure 4.1b). The alignment pattern is then imaged using SEM, FIB, and LM, with the light microscopy image captured by collecting reflected light from the sample (Figure 4.1c).

With an NA of 0.85, and the refractive indices of both the objective lens and the sample, the axial scaling behaves linearly as long as fluorescent emitters are no deeper than about 9 µm Loginov et al., 2024. The upper thickness limit for obtaining vitreous plunge-frozen hydrated cells is 10 µm Wagner et al., 2020. Therefore, the focal shift (i.e., the difference between the actual and measured emitter position) for a targeted emitter ranges from 0 to ~2.7 µm, scaled linearly at ~300 nm shift per micrometer of emitter depth. This is schematically illustrated in Figure 4.1d, where

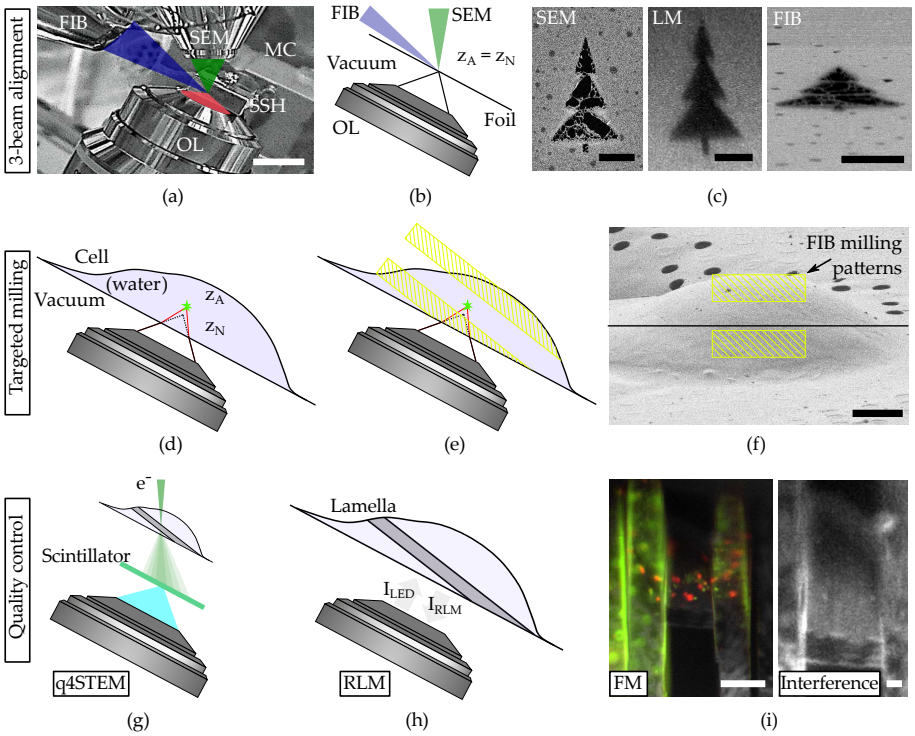

Figure 4.1: The alignment of the experimental setup used for lamella fabrication (a through c), the targeting & milling approach (d through f) and techniques for quality control (g through i). **(a)** Infrared photograph acquired with the camera mounted on the FIB-SEM host system showing the three coincident beams (SEM, LM and FIB) along with the microcooler and OL mounted inside the microscope chamber. The EM grid containing frozen cells is contained in the sample shuttle holder (SSH) and epi-fluorescence imaging is done from the bottom (transparent red). **(b)** Alignment of the optical microscope is done by moving the objective lens, without a RIM present. The AutoGrid and coverslip have been omitted for clarity. **(c)** Milled pattern imaged with three imaging modalities after alignment, the light microscopy image is acquired by collecting reflected light from the sample. **(d)** When targeting fluorescence inside a cell, the axial coordinate is distorted due to RIM. The measured axial position (z_N) of the fluorescent emitter does not coincide with the actual position (z_A). **(e)** The bottom milling pattern is positioned close to the coincident point, as the fluorescent emitter *always* sits further away from the objective lens due to axial scaling. **(f)** Placement of the asymmetric milling pattern with respect to coincidence (black line), in the FIB field of view prior to rough milling a cellular structure. **(g)** Schematic diagram showing the geometry and detection principle used to measure lamella thickness with q4STEM (Skoupỳ et al., 2023). By collecting scintillation light from the scattered electron pattern with the optical system, the lamella thickness can be determined. **(h)** Schematic showing the lamella orientation with respect to the objective lens. The lamella thickness can be estimated by collecting the reflected light intensity from the lamella (I_{RLM}), both through the known imaging geometry and interference effects, see also **(i)**, right. **(i)** The fluorescence intensity can be monitored during and in between milling, thus the presence of the biological target inside the lamella is guaranteed. Thin film interference effects are present in RLM, as seen by the intensity gradient going from bottom (dark) to the top (bright) of the lamella. In addition, interference fringes are visible originating from a Newton interferometer geometry. Both of these effects can be exploited to determine the thickness of the lamella. Scale bars: **(a)** 2 cm, **(c)** 5 µm, **(f)** 5 µm, **(i)** 10 µm (left), 2 µm (right).

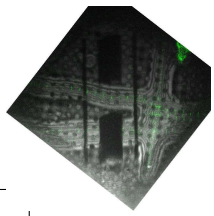

a fluorescent object at actual depth z_A is imaged at the axial coordinate z_N due to the optical microscope's aberrations Loginov et al., 2024.

To quantitatively correct the focus shift, precise measurement of the scaled distance is needed, which is achieved by determining the focal length difference between the foil (the RIM interface) and the fluorescent emitter. Since lamella fabrication occurs in a step-wise process, with lamella thickness after rough milling typically ranging around 2 to 3 µm, we adopted an alternative approach. When imaging from a low ($n_1 = 1$) to a high ($n_2 = 1.28$) refractive index, the optical microscope's axial coordinate system appears compressed. This enables an asymmetric milling pattern, where the bottom pattern is placed a few hundred nanometers away from the coincident point (Figure 4.1e and f). Consequently, the top milling pattern is set approximately ~2.7 µm away from the coincident point, ensuring that the fluorescent ROI is captured within the rough-cut lamella.

Quality and thickness control are ensured through three complementary techniques that estimate the thickness of a frozen-hydrated lamella during the milling process. We apply our previously presented q4STEM method Skoupỳ et al., 2023 to frozen-hydrated lamellae (Figure 4.1g). By leveraging the known imaging geometry and interference effects present in the RLM, we can estimate lamella thickness and verify the presence of the fluorescent target inside the lamella using FM (see Figure 4.1h,i). Further details on these methods are discussed below.

Automated milling of fluorescent targets

We set out to implement *in-situ* fluorescence targeting to establish automated lamella preparation on selected cellular targets. Our workflow is illustrated in Figure 4.2, where potential target cells are identified using a low-magnification SEM image (white markers) prior to applying the Pt coating with the GIS. Each site is imaged using FM to refine target positions, and additionally, the sites are screened using RLM. During the sample preparation, ice crystallites occasionally form, and larger clusters can obscure the target site. These clusters are often found below the foil side of the grid and thus remain invisible in the SEM image. They not only obstruct fluorescence imaging but also induce additional axial scaling when located directly beneath the target. If present along the lamella's milling direction, they may also hinder subsequent tilt series acquisition in the TEM. RLM imaging using the integrated optical microscope helps identify and discard these sites (Figure 4.2, red marker with white cross), thereby increasing the success rate of high-quality lamella for cryo-ET.

Once N final milling targets have been selected, asymmetric rough milling of the lamella is performed in an automated fashion using the stored XYZ stage coordinates obtained from the FM imaging. For each milling site, the Odemis acquisition software positions the stage and automatically captures images in the relevant channels of the light microscope Piel et al., 2022. This imaging occurs both before and after rough milling, resulting in N milled sites (yellow marker with an R in Figure 4.2)

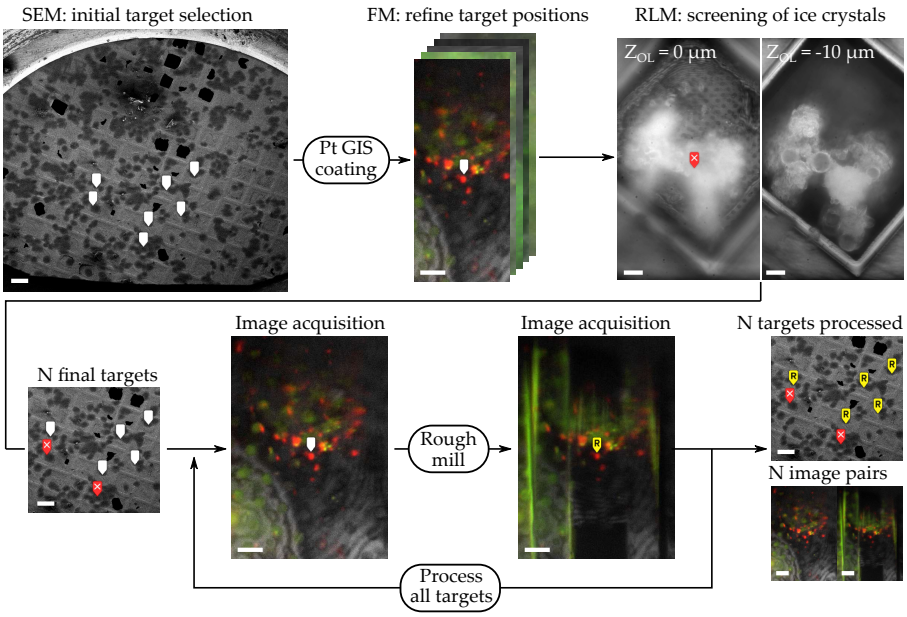

Figure 4.2: Fluorescence targeted, automated lamella preparation workflow for selected cellular targets. Initial target cells are identified in a low magnification SEM image (white markers, 1 keV, 25 pA, ~ 2 mm horizontal field width). After applying the Pt coating, the target positions are refined through fluorescence imaging and targets are screened for the presence of ice crystals using the RLM. *N* final targets are rough milled automatically, whilst acquiring FM images before and after. Scale bars: 100 µm (SEM images), 10 µm (RLM images) and 100 µm (FM images).

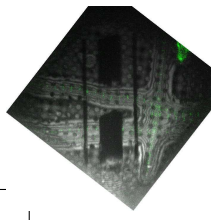

and corresponding image pairs. More examples of these image pairs are shown in Figures S.2 and S.3 and were acquired over approximately four weeks during milling of different biological specimens.

In this study, the Helios Nanolab 650 FIB-SEM (Thermo Fisher Scientific) was used to carry out the milling, with our integrated cryo-light microscope retrofitted as described previously Daan B Boltje, Hoogenboom, Jakobi, Jensen, Jonker, Kaag, Koster, Last, Agrela Pinto, J. M. Plitzko, et al., 2022. Instructions to mill a pre-defined pattern with the FIB are sent through the XTLib interface (Thermo Fisher Scientific) by adjusting the SEM scan rotation. An iFast script (Thermo Fisher Scientific) executes the milling process, after which the scan rotation is returned to its original value, indicating that milling at this site is complete. Similar strategies for controlling beam, stage, and imaging operations can be employed through the instrument API of other manufacturers. The total time to perform stress relief cuts, mill an initial lamella, and acquire the LM images is approximately 4 to 5 min per site. The rough lamella can then be thinned down to <200 nm, with quantitative feedback on the thickness, as outlined below.

Thickness determination through q4STEM

Reproducible FIB micromachining of high-quality frozen-hydrated lamella requires robust control over the sample thickness during the milling process. The scattering patterns of transmitted electrons can be recorded by converting our integrated light microscope into an optical 2D-STEM detector. As shown in previous work, this is achieved by replacing the ITO-coated glass coverslip of the integrated optical microscope with a scintillator positioned directly below the AutoGrid (Figure 4.3a) (Daan B Boltje, Hoogenboom, Jakobi, Jensen, Jonker, Kaag, Koster, Last, Agrela Pinto, J. M. Plitzko, et al., 2022; Skoupỳ et al., 2023). While we previously used a Yttrium aluminium garnet (YAG) scintillator in our proof-of-principle work, its optical emission spectrum in the visible range conflicts with the absorption and emission spectra of typical fluorescent targets. For this reason, we opted for lutetium aluminium perovskite (LuAP), which has a relatively low optical emission wavelength and interferes only with 440 nm-centered fluorescence emission. To record electron scattering patterns, the OL is lowered along the SEM optical axis to focus on the top scintillator surface while maintaining alignment with the SEM (Figure 4.3a). When the estimated lamella thickness is below approximately 1 µm, the thickness can be determined using q4STEM Skoupỳ et al., 2023. With the SEM in spot mode, the optical microscope focus is fine-tuned through direct electron beam exposure on empty grid foil holes (Figure 4.3b, inset). Individual scattering profiles from different parts of the lamella are then recorded using the SEM beam shift. In our setup, temporal coordination of electron exposure is managed by controlling the Fast Beam Blanker on our Helios Nanolab 650 (Thermo Fisher Scientific) via the transistor-transistor-logic (TTL) signal output from our optical camera. At each probe position, the lamella thickness is calculated through a radial sum over the scattering profile (Figure 4.3c)

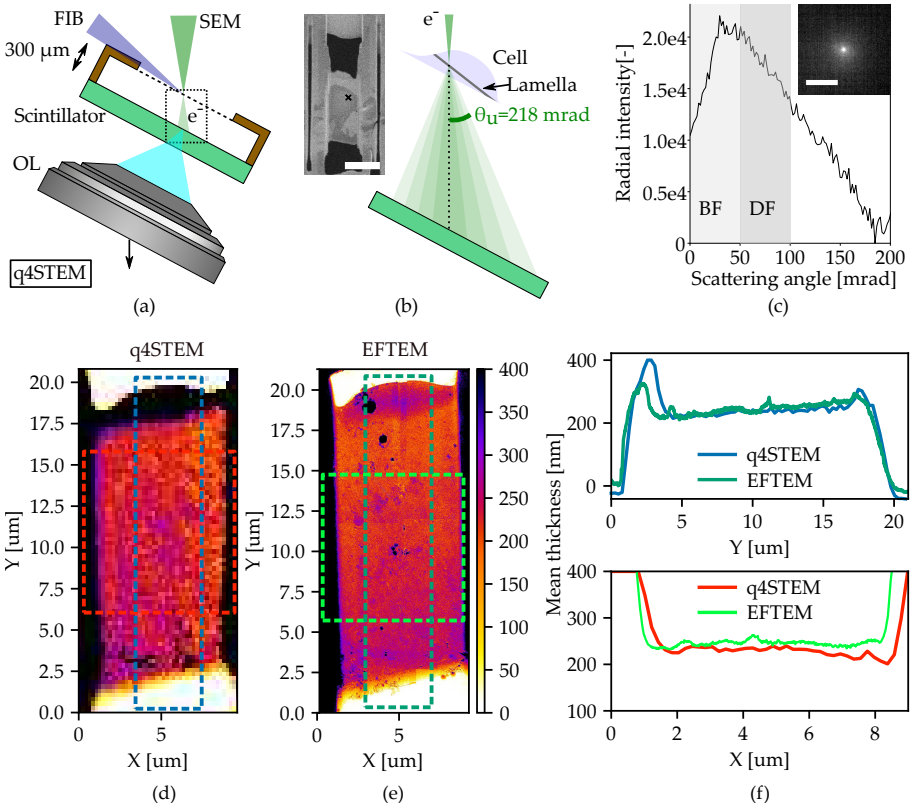

Figure 4.3: q4STEM-measured thickness of frozen hydrated lamella compared quantitatively with thickness estimates from energy filtered TEM. **(a)** Schematic diagram showing the geometry and detection principle used to measure lamella thickness with q4STEM. The OL focus is moved downward (arrow, along the electron optical axis) to the top scintillator surface, where the scattered electron pattern is visualized by collecting the scintillation light (transparent blue). **(b)** Schematic illustration showing the scattering process in more detail (dotted box in (a)). The left inset shows a SEM image from an intermediate milling step; the black cross marks the position at which the q4STEM measurement was acquired. **(c)** The integrated radial intensity profile as computed from the acquired image (see inset). The thickness is determined by taking the ratio of the virtual dark- and bright field intensity sum, as discussed in earlier work Skoupỳ et al., 2023. **(d)** q4STEM thickness map after correcting for the SEM angle of incidence of 52°. The map consists of a 64 × 100 pixel grid acquired with a 200 nm pixel size. **(e)** EFTEM thickness map from zero-loss imaging after correcting the lamella pre-tilt of 10°; pixel size is 3.59 nm. A baseline correction has been applied to the EFTEM data to yield zero thickness outside the lamella (vacuum), **(f)** Mean line profiles along the *X* and *Y* direction of the lamella. The dotted boxes in **(d, e)** annotate the region across which the mean intensity was computed. Scale bars: **(b)** 10 µm, **(c)** 33 µm or 109 mrad.

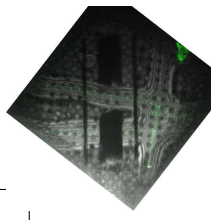

and computing the integrated dark field/bright field (DF/BF) ratio. The DF/BF ratio, along with an estimate of the most common scattering angle, can then be compared to tabulated data from Monte Carlo (MC) electron scattering simulations to derive the final thickness Skoupỳ et al., 2023.

To validate the robustness of thickness estimation using q4STEM on frozen-hydrated lamella, we employed fluorescence-guided FIB milling to fabricate a lamella from vitrified HeLa cells stably expressing mRFP-EGFP tandem fluorescent-tagged Microtubule-associated protein 1A/1B light chain 3B (mRFP-GFP-LC3), a dual fluorophore probe used for studying autophagosomes and their trafficking Kimura et al., 2007b (Figure S.4). After automatic milling to an approximate thickness of 250 nm, we acquired a 2D convergent beam electron diffraction pattern at each pixel position of a 2D STEM raster covering the lamella. The resulting 4D STEM dataset was then evaluated using the q4STEM method, yielding local thickness measurements at each probe position, corrected for the non-perpendicular incidence of the electron beam (Figure 4.3d). We then transferred the sample to a JEOL JEM3200-FSC TEM operating at 300 kV and acquired a baseline-corrected EFTEM thickness map using zero-loss imaging (Figure 4.3e). The two techniques showed good agreement, with a mean thickness difference of only 7 nm across the central 4 µm region of the lamella (Figure 4.3d, e).

Figure 4.3f shows the mean line profiles corresponding to overlays in the respective 2D maps. Both the q4STEM and EFTEM profiles reveal a ~50 nm reduction in thickness from the Pt-coated leading edge to the trailing edge of the lamella, caused by the diminished incident ion flux along the lamella due to the grazing angle. The bump indicating an apparent increase in thickness at $Y = 3\,\mu m$ of the lamella is attributed to the platinum-rich GIS coating used to protect the lamella during FIB milling, as the scattering profile is interpreted using simulated data of pure frozen water.

We assessed the possibility of beam-induced damage due to low-voltage electron exposure in the SEM by examining a sample of lysosome crystals, as detailed in the Supplemental Information (Figure S.5). Our analysis focused on low-order reflections due to the limited sensitivity of the scintillator-based detection method. With increasing electron fluence, the intensity of the 0-order peak increases due to electron beam-induced degradation of the crystal structure. While a more detailed assessment of radiolytic damage affecting higher-resolution features would require future studies using a more sensitive, pixelated direct detection STEM detector, we argue that thickness determination via q4STEM remains a viable method as we apply q4STEM exclusively to the edges of the lamella, located 2 to 10 µm away from the ROI for tilt series acquisition to avoid damage to critical areas. To support this, we have performed MC simulations of 30 kV electrons impinging on a 1000 nm lamella using CASINO Drouin et al., 2007. The MC electron trajectories suggest that 95 % of the deposited energy remains within a maximum radius of 50 nm of the incident beam profile, which is consistent with previous estimates Pimblott et al., 1990. The cross-sectional diffusive radius of reactive radiolytic products in amorphous water

ice, mediated through for instance low energy (secondary) electrons, is reported to range between 2 to 70 nm Abellan et al., 2023; Aronova et al., 2011. We therefore estimate that beam-inflicted radiolytic damage is likely restricted to several tens of nanometers off the q4STEM scan line and will not affect the ROI at several micrometers distance from that scan line.

Thickness & quality control using RLM

Live feedback on lamella thickness and quality during milling can be obtained by acquiring RLM images with the coincident light microscope in addition to FM targeting (Figure 4.4). We demonstrate this process using fluorescence-targeted lamella preparation from HeLa cells expressing mRFP-GFP-LC3, which allows simultaneous localization of autophagosomes and autophagolysosomes. First, ROIs are selected based on the fluorescence images (Figure 4.4a) of suitable cells, originally chosen via the low-magnification SEM image (Figure 4.4a, inset). The overlay of the two-channel FM image with the simultaneously acquired RLM image clearly shows the fluorescence embedded in the context of the frozen-hydrated cell and grid support (Figure 4.4a).

FIB milling is then performed at a 10° angle relative to the plane perpendicular to the light microscope's optical axis, creating the geometry shown in Figure 4.4b. The optical focus depth is approximately 500 nm (red shaded area), allowing focus on either the top (Pt, blue) or bottom (foil, green) side of the lamella by adjusting the z position of the sample stage. The lamella thickness is estimated by measuring the width w of the bottom (foil) side of the lamella (Figure 4.4b, inset). The thickness d is then calculated using the relation $d = w \cdot \sin(\theta)$, where θ is the milling angle.

Acquiring an RLM z-stack during intermediate milling steps allows for assessing the milling process beyond thickness estimation. Both the foil and Pt GIS sides can be brought into focus (Figure 4.4c), allowing us to evaluate the: (i) lamella thickness d by measuring w from the foil side; (ii) state and uniformity of the Pt GIS layer, which protects the lamella during ion beam milling; (iii) overall uniformity of the milled lamella; and (iv) accuracy of the milling angle by measuring the defocus (4 µm) over the full lamella length (22.4 µm), yielding $\theta = \arcsin\left(4\,\mu m / 22.4\,\mu m\right) = 10.2°$. By setting the optical focus between the top and bottom of the lamella (at 1.6 µm in Figure 4.4c), an approximate lamella thickness d can be estimated, while the highly reflective Pt GIS layer is used to assess the protective layer's uniformity.

Snapshots showing the progress of the milling process are presented in Figure 4.4d. These images are taken after pausing FIB milling, with the foil side of the lamella in focus. The width w decreases as the lamella becomes thinner, and the instantaneous thickness d is displayed at the top of the snapshots along with the milling duration, color-coded. Additionally, a series of RLM images is acquired during FIB milling, with the optical focus set between the bottom and top of the lamella. The mean reflected intensity along the Y axis is plotted in Figure 4.4e for different milling stages. Characteristic intensity peak at the beginning (Y = ~7µm) and end (Y =

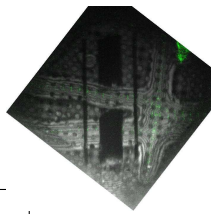

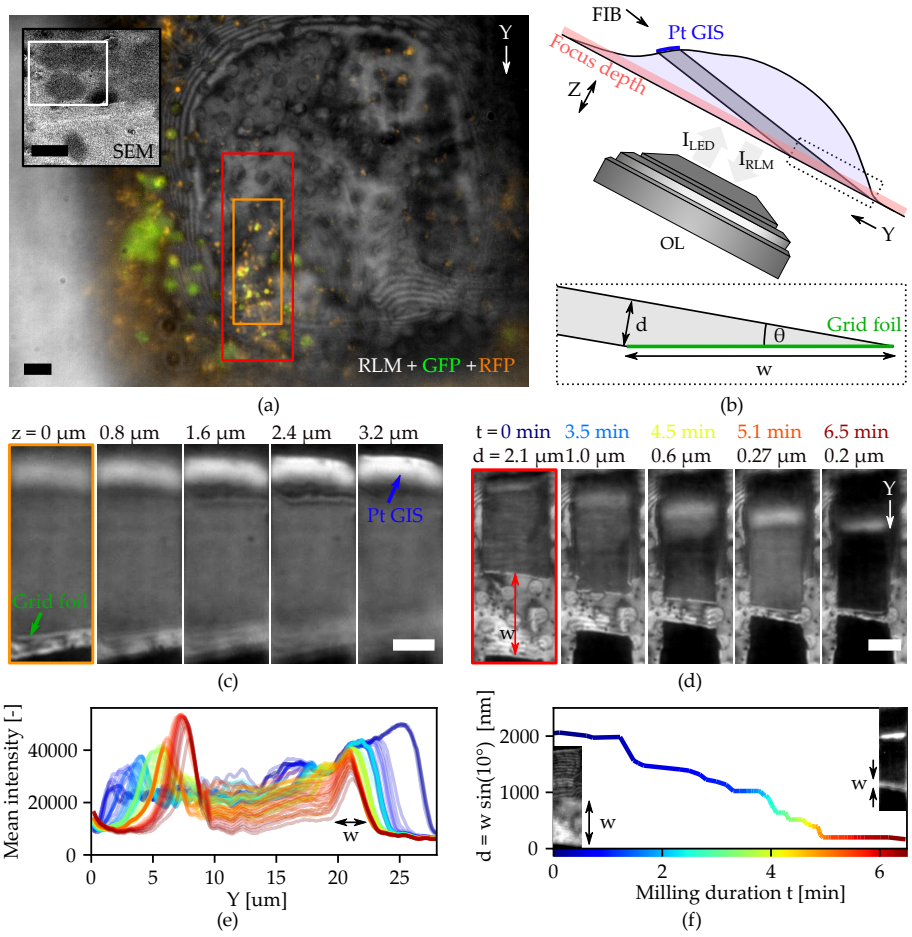

Figure 4.4: Targeted and quality controlled FIB milling with in-situ fluorescence and reflected light imaging. **(a)** Initial target selection in HeLa cells expressing mRFP-GFP-LC3 using fluorescence microscopy (colors) overlaid on reflected light (grayscale). Green & yellow: autophagosomes and red: autophagolysosomes. The light microscope FOV is denoted by the white rectangle in the top left inset, showing the grid square in the SEM overview image. **(b)** Sketch showing the lamella- and RLM imaging geometry. The optical focus depth (red translucent are) is about 500 nm. The dotted box shows the lamella geometry close to the grid foil. The lamella thickness d can be estimated by measuring distance w along the tapered wedge of the lamella by $d = w \cdot \sin(\theta)$. **(c)** Cropped slices (orange rectangle in (a)) from a RLM z-stack acquired with the lamella milled to about 300 nm in thickness. Top and bottom side of the lamella can be imaged by changing the optical focus (respectively Pt GIS and foil sides, green and blue annotations, also visible in (b)). **(d)** Various stages (time points) of the lamella milling process (FOV cut to red marked area from (a)). The lamella thickness d can be estimated by measuring w along the bottom wedge of the lamella. **(e)** Mean X RLM intensity profiles along the lamella length Y (line color indicates milling progression/time according to the color scale in (f)). w can be measured from the width of the foil-side intensity peak. **(f)** Estimated lamella thickness d versus milling duration. The two insets show the lamella as imaged in RLM at the start and end points of thinning. The lamella thickness can be estimated to approximately 250 nm. Scale bars: **(a)** 5 µm, inset: 50 µm, **(c)** 5 µm, **(d)** 5 µm.

~25 to ~20 µm) of each line trace correspond to the bottom and top sides of the lamella, respectively. By measuring the width w at each stage, the lamella thickness can be calculated and plotted against milling duration (Figure 4.4f). The insets show the first and final images used to determine w. This method enables monitoring of the milling process down to a thickness of around 1 µm.

Thin-film interference effects can be leveraged to achieve more accurate lamella thickness determination than with geometric estimations, as demonstrated by Last *et al.*, who utilized multicolor RLM to measure thickness at the periphery of vitrified cells grown on cryo-EM support films Last et al., 2023. We demonstrate the application of thin-film interference for thickness determination in our coincident light microscope by first milling a rough lamella to approximately 2.6 µm thickness, as seen in Figure 4.5a.

Next, a cleaning cross-section pattern was defined within the FIB field of view to thin the lamella at a consistent rate (Figure 4.5b, top). The milling process proceeded line by line, with an effective rate of 2.4 nm/s along the FIB Y axis to ensure even thinning, beginning from the top ($t = 0$ s) and continuing until a thin lamella remained after completion (Figure 4.5b, bottom and Figure 4.5c). The final thickness, approximately 430 nm, was derived from the width w measured in the RLM image. Further thinning was prevented by a discontinuous Pt GIS layer, highlighting the utility of monitoring Pt coating integrity during milling.

We acquired RLM images during FIB milling using three different wavelengths ($\lambda = 463,\ 542$ and 632 nm, 189 images per channel, 567 total images), as depicted in Figure 4.5d. For each wavelength, 35 individual line traces were extracted from the white rectangles and plotted against lamella thickness. The reduction in thickness was calculated based on the image timestamp and the constant milling rate of 2.4 nm/s. A lamella thickness offset of 390 nm was applied to the traces, which falls within the error margin of the geometric estimate, especially given the non-uniformity of the protective Pt GIS layer. The dashed black line represents the reflectivity model $r(d, \lambda, T)$, similar to Last et al., 2023:

$$r(d, \lambda, T) = r_{\text{mea}} + \frac{r_{\text{A}} e^{-d/L}}{2} \cos\left(\frac{4\pi\, d\, n_2(\lambda, T)}{\lambda} + \pi\right) \tag{4.1}$$

Here, r_{mea} and r_{A} are constants adjusted to match the measured reflected intensity, as determined from the acquired images. d is the lamella thickness, and L is a constant accounting for scattering and coherence loss in the thin film, set to 500 nm. The refractive index values for amorphous ice, $n_2(\lambda, T)$, are taken from Kofman *et al.* Kofman et al., 2019.

Good agreement between the reflectivity model and the measured data was observed across all three wavelengths, allowing lamella thickness to be determined according to the method outlined by Last *et al.* Last et al., 2023. To streamline both data acquisition and analysis, we opted to measure reflected intensity for a single wavelength only. By performing error minimization on the reflectivity data, using

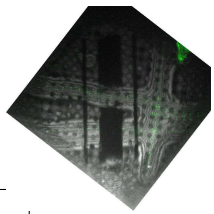

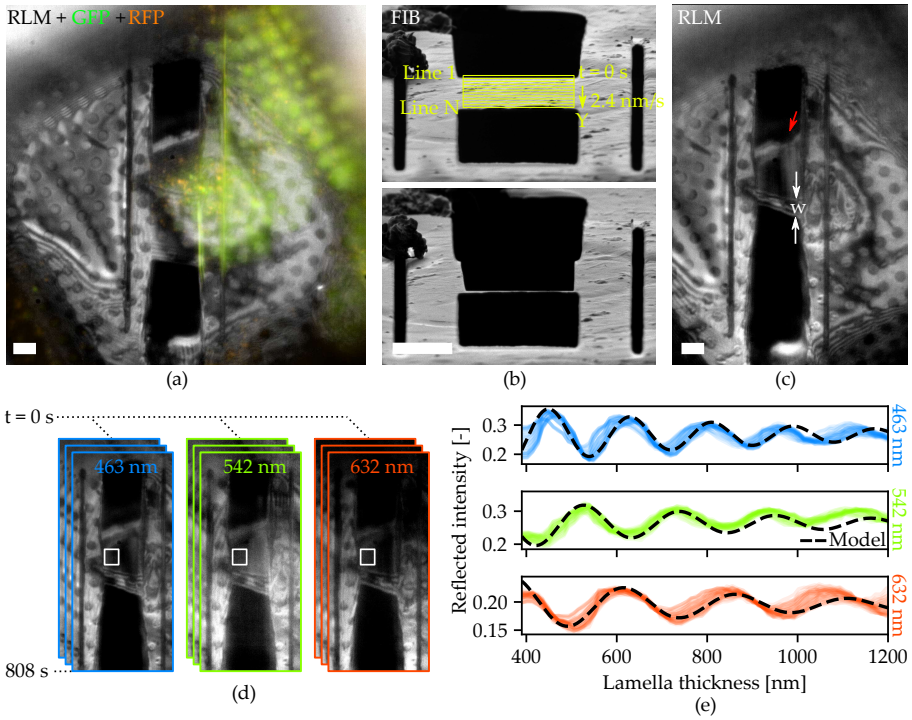

Figure 4.5: Reflected light intensity monitors lamella thickness during milling. **(a)** Lamella after rough milling, as imaged with fluorescence microscopy (colors) overlaid on reflected light (grayscale). At this stage, the lamella thickness d is approximately 2.6 µm (w = 15.3 µm). **(b)** The lamella after rough milling (top) and after thinning (bottom), as imaged with the FIB. The lamella is evenly thinned by defining a cleaning cross-section pattern in the FIB field of view (yellow marked area), having a constant milling rate of 2.4 nm/s along the FIB Y direction. The FIB milling progresses line-by-line at this rate, starting at the top (line 1) and ending at the bottom (line N)**(c)** Lamella after thinning, as imaged with reflected light (grayscale). At this stage, the lamella thickness d is approximately 430 nm (w = 2.5 µm), and the Pt GIS layer has been partially removed (red arrow), preventing further thinning. **(d)** Reflected light images are recorded in three different channels during the even lamella thinning. **(e)** For each reflected light channel, the normalized reflected intensity is plotted against the lamella thickness. 35 individual intensity traces are plotted for each channel (from white rectangle in (d)), along with the reflectivity model based on thin film interference (dashed black, Equation 4.1). All scale bars: 5 µm.

the geometric thickness estimate as an initial approximation, we can generate 2D thickness maps of the lamella as a function of milling progress, as shown in the next section.

Controlled lamella fabrication workflow

Finally, we combine the above into a single workflow for quality- and thickness-controlled fabrication of fluorescence-targeted lamellae. Initial target selection is done with fluorescence microscopy, and quality control is performed using the RLM, as discussed earlier. In reflected light imaging, the wedge-shaped endpoints of the lamella act as a Newton interferometer (NI) due to the changing thickness (Figure 4.6a). From an approximate lamella thickness of 1.5 µm, a region of constant thickness starts to appear in the middle, where thin-film interference (TFI) occurs. The normalized reflected intensity is recorded at a single point (blue cross) and plotted using the geometrical thickness estimate d_{est} in Figure 4.6b (blue scatter). The thickness can then be further refined through error minimization using the normalized version of the reflectivity model (Equation 4.1), yielding the green scatter in Figure 4.6b, and the green curve in Figure 4.6c. This reflects more intricate thickness differences compared to the initial (geometrical) thickness estimate, partly because the thickness measurements come from different locations on the section, but also because the (local) lamella reflectivity is more sensitive to thickness variations.

As reflected light *images* are acquired, this process can be extended to all the pixels on the lamella showing TFI, thus converting a grayscale reflected light image into a 2D thickness map of the lamella, as shown in Figure 4.6d. To visualize thickness variations at each stage of lamella thinning, the minimum and maximum values of the color scale are adjusted for each image. At three time points during lamella thinning (4.5, 5.1 and 6.5 min), q4STEM data along the Y direction were acquired (colored dots). Along with the line traces of the 2D thickness maps (black lines) and the thickness estimate from the milling geometry (dotted line), the lamella thickness is plotted along the Y direction in Figure 4.6e. The three different methods are in good overall agreement, showing an approximate lamella thickness of 600, 300 and 200 nm at different stages of milling, although d_{est} overestimates the thickness below 300 nm. The mean difference between q4STEM and TFI measured thicknesses is −57, 56 and −21 nm for the three time points, resulting in a relative difference of 10 to 20 %. At the 6.5 min time point, a lamella thickness of 188 nm was reached, with a uniformity of less than 5 nm (one sigma) from the error-minimized TFI data. Since the protective Pt GIS layer was too thin and non-uniform, polishing was stopped.

The polished lamella was unloaded from the FIB-SEM using a cryogenic transfer system and loaded into a JEOL JEM3200-FSC TEM operated at 300 keV. An overview image was acquired in the TEM (see Figure 4.7a). After polishing was completed, fluorescence data was overlaid on the overview image, and alignment between the TEM and the (reflected) light microscopy data was performed using eC-CLEM Paul-Gilloteaux et al., 2017. This overlay is used to set the ROI for tomogram ac-

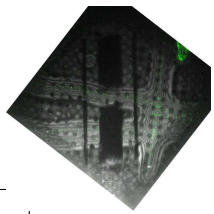

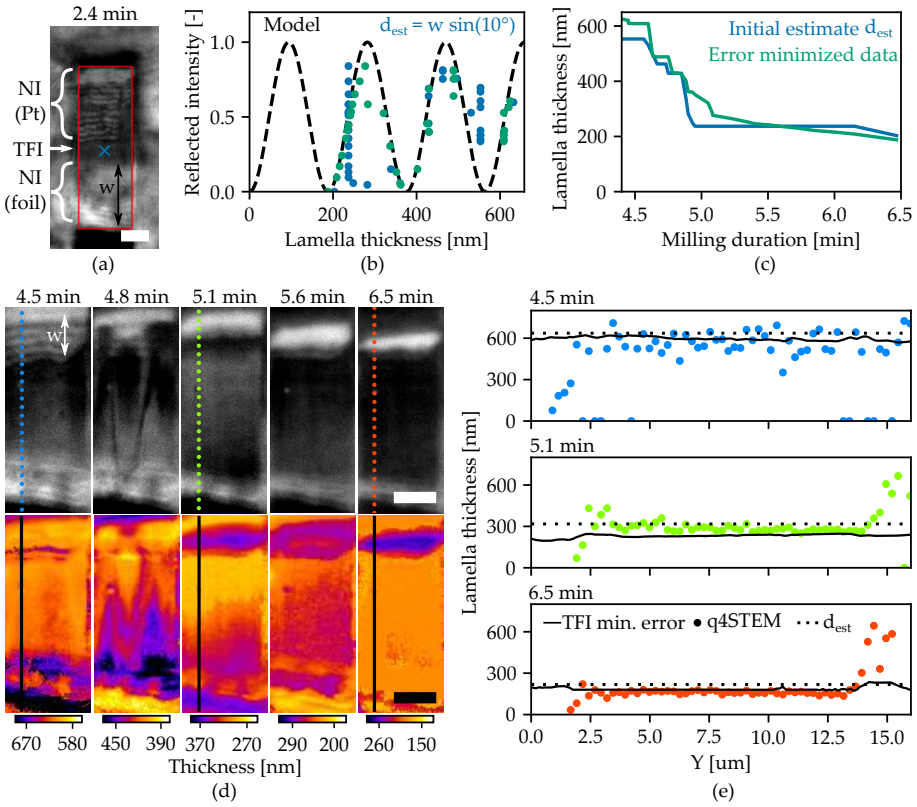

Figure 4.6: Thickness controlled lamella fabrication. **(a)** The lamella imaged in RLM ($\lambda = 463\,\text{nm}$) at an intermediate milled state ($d \approx 1.5\,\mu\text{m}$). The bottom (foil) and top (Pt GIS) sides of the lamella are wedge shaped and act as a Newton interferometer (NI). The region between has a more uniform thickness, and hence thin film interference (TFI) occurs. **(b)** With milling progression, the reflected intensity is recorded (at the blue cross in (a)), along with the lamella thickness estimate $d_{\text{est}} = w\sin(10°)$ from the milling geometry (blue scatter). Error minimization is performed using a normalized version of the reflectivity model (dashed black), which outputs a refined lamella thickness estimate (green scatter), and finally yields **(c)** the lamella thickness versus milling duration. **(d)** The lamella imaged in RLM at varying stages of milling (top, grayscale). q4STEM data has been acquired at three time points during the milling (dotted colored lines). The error minimization process as outlined in (b) and (c) can be performed for all pixels in the RLM images, yielding thickness maps at varying stages of milling (bottom, colored). **(e)** Lamella thickness line traces along the Y direction, at three different time points. Thickness measurements include q4STEM (colored dots, see also (d) top), the error minimization of the normalized reflectivity (black lines, see also (d) bottom), and estimates from geometry d_{est} (dotted black lines). The increase in measured thickness around $Y = 15\,\text{um}$ is due to the increased density of the Pt GIS layer. All scale bars: $5\,\mu\text{m}$.

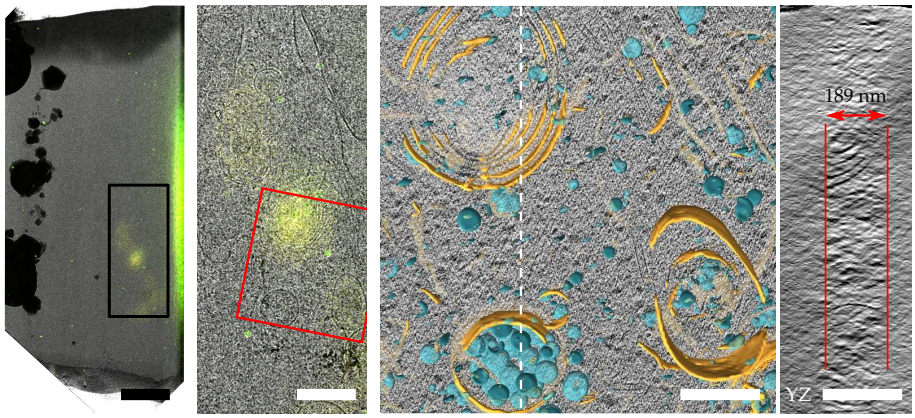

Figure 4.7: Cryo-electron tomography with fluorescence-targeted, thickness and quality controlled FIB-milled lamella. **(a)** Overview image of the lamella in TEM with overlaid fluorescence data. TEM and fluorescence images are aligned based on the reflected light image. This overlay is used for tomography target selection. **(b)** Zoom of the black-boxed area in (a). **(c)** Snapshot from the reconstructed tomogram with membrane segmentation as an overlay, acquired at the red rectangular area marked in (b). A YZ slice taken along the dashed white line is shown on the right, annotating the lamella thickness as measured from the reconstruction. Scale bars: **(a)** 2.5 µm, **(b)** 1.0 µm, **(c)** 250 nm.

quisition (Figure 4.7b, red box). A snapshot from the acquired tomogram is shown in Figure 4.7c (left), along with the segmentation overlay. The lamella thickness is measured from the YZ slice along the dashed white line (Figure 4.7c, right), yielding 189 nm, which is in close agreement with the 188 nm estimate from TFI.

4.3 DISCUSSION

We have presented three different methods to accurately determine the lamella thickness during FIB milling, using a light microscope integrated in a FIB-SEM system; (i) by selecting a scintillator better suited for use in a fluorescence microscope, we were able to apply an earlier presented quantitative 4D-STEM technique Skoupỳ et al., 2023 to the cryogenic lamella fabrication workflow. Benchmarking this technique to EFTEM showed good agreement in the determined thickness. (ii) The lamella thickness was estimated during milling via the known milling and imaging geometry, which produced reliable estimates between 2000 to 400 nm. (iii) Exploiting thin-film interference phenomena on a per-pixel basis yields a fine-grained thickness map of the lamella, thus providing quantitative feedback on the lateral thickness variations. The final lamella thickness estimate was compared with the thickness determined from reconstructed TEM data and showed excellent agreement.

We further showed how to target fluorescent regions of interest whilst correcting for the axial distortion induced by the inherent presence of a refractive index mis-

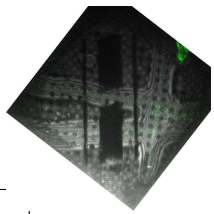

match when imaging into a frozen cell. RLM is used to inspect milling sites to discard those sites which have parasitic ice present underneath the EM grid. A rudimentary form of communication between the FIB and FM control PCs is used to perform automated rough milling of fluorescent targets.

For different sample types, such as specimen prepared by the Waffle method or high-pressure freezing (HPF) the thickness can extend up to ~200 µm K. Kelley et al., 2022; Monaghan et al., 1998. As such, depth dependent axial scaling effects need to be considered, and quantitatively corrected for by accurately measuring the axial coordinate z_N (distance between refractive index interface and emitter) as observed in the optical microscope.

Our methods provide live feedback on lamella thickness and uniformity, integrity of the Pt coating layer, and presence of the fluorescent target when preparing a lamella out of a frozen hydrated cell. This reduces the complexity of the milling process and substantially increases the yield for producing lamella suitable for high-resolution cryo-EM analysis. Combined with its ability for fluorescence-based targeting, our procedure paves the way towards an automated workflow that allows for fluorescence, thickness, and quality control, facilitating the routine fabrication of frozen-hydrated cell sections and highlights potential advantages of coincident FM-FIB-SEM instruments in workflow automation.

4.4 LIMITATIONS OF STUDY

q4STEM and RLM thickness determination during the milling process requires a coincident light microscopy setup integrated in the FIB-SEM system. This is absolutely required for the RLM measurements; for q4STEM an optional pixelated STEM detector may also be used and could provide improved sensitivity compared to the optical STEM signal detection employed in our setup. The q4STEM thickness determination method relies on Monte Carlo simulations of the scattering process of transmitted electrons and currently depends on parametric approximations of material composition and uniformity. Based on theoretical considerations these approximations may lead to thickness over- or underestimation of ~ 2-3% for vitreous cellular material.

Alternative to a light microscope coincident with the FIB, an *in-situ* reflected light microscope might also be used for thickness determination through the geometry. Although this would require stage moves between the LM and FIB, this can be implemented through software automation in commercially available systems Smeets et al., 2021; ThermoFisher Scientific, 2021, 2024.

4.5 ACKNOWLEDGMENTS

We thank Ernest B. van der Wee for the useful discussions, and extend our gratitude towards Joyce van Loenhout and Leanid Kresik for providing cellular samples

used during optimisation of automated FIB milling. We are thankful for the helpful discussions on the cryo-TEM workflow with the groups of C. Genoud and H. Stahlberg, during JPHs research stay at UNIL-EPFL. This work was financially supported by NWO-TTW project Nº 17152 to JPH and the European Research Council (ERC-StG-852880) to AJ.

4.6 AUTHOR CONTRIBUTIONS

AJJ and JPH conceived and initialized the collaboration between their two research groups. First principle q4STEM experiments were carried out by RS, extended to the cryogenic workflow by DBB. DBB performed the experiments on thickness determination through the use of reflected light imaging. CT prepared the various cellular samples and together with DBB performed cryo-FIB milling. cryo-ET experiments were done by CT and WHE. DBB drafted the manuscript together with AJJ and JPH. All authors provided feedback and commented on the final version.

4.7 DECLARATION OF INTERESTS

CT and WHE declare no competing interest. Parts of this work are covered in; NL Patent 2032641 (RS, JPH, AJJ, DBB) and 2028497 (DBB). DBB is an employee of Delmic BV. JPH has a financial interest in Delmic BV.

4.8 SUPPLEMENTAL INFORMATION

Table S1: **Overview of scintillator candidates.**

Scint.	Cryst. struct.	λ_{ab} [nm]	λ_{em}^{max} [nm]	BF	Ref
YAG	C	460, 340	550	No	1
YAP	OR	300	370	Yes	2
LYSO	MC	250, 360	425	Yes	3
LuAP	OR	300	365	Yes	4

C, OR and MC refer to cubic, orthorhombic or monoclinic, BF indicates birefringence.

1 Crytur, 2023
2 Crytur, 2023; Donnald et al., 2018
3 Blahuta et al., 2013; Crytur, 2023; Pidol et al., 2004
4 Crytur, 2023; Drozdowski et al., 2006; Lempicki et al., 1998; Surface preparation laboratory, 2023

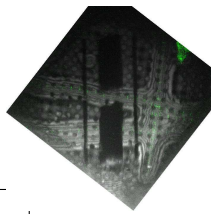

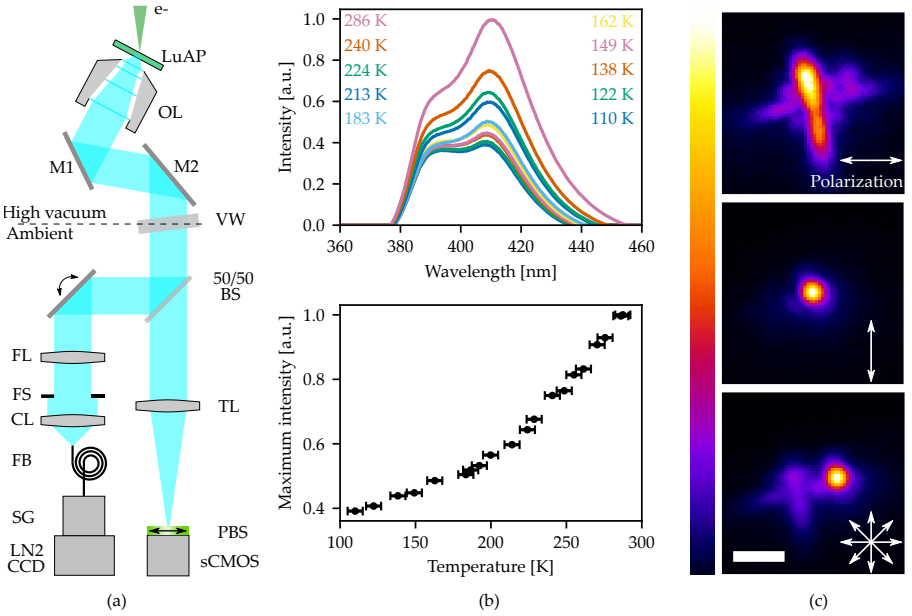

Figure S1: Optical properties of a LuAP scintillator under electron irradiation and the layout of the optical path. **(a)** Overview of the optical path denoting relevant components. The LuAP scintillator is irradiated with 5 keV, 100 pA electons. The scintillation light is collected by the objective lens (OL) and passed to the 50/50 beam splitter (BS), where it is divided between the excitation- and emission arms. This allows part of the light to be passed to the tube lens (TL) and focussed onto the camera (sCMOS) to form an image. A polarizing beam splitter (PBS) is added in front of the camera. The fiber coupled light source is replaced with a spectograph (SG) fitted with a liquid nitrogen cooled CCD camera. **(b)** Electron induced scintillaton emission spectra as a function of scintillator temperature (top). Peak positions do not shift, but the scintillation yield decreases. Peak maxima are plotted against temperature (bottom). The scintillation yield decreases with a factor of 2.5 going from 286 to 110 K. Horizontal errorbars of 5 K. **(c)** Scintillator birefringence is visualized by imaging the electron induced scintillation spot with the optical system. Without PBS present two spots are present (top) and the parasitic spot (middle) can be filtered out (bottom) depending on the PBS orientation. Scale bars: **(c)** 2 µm.

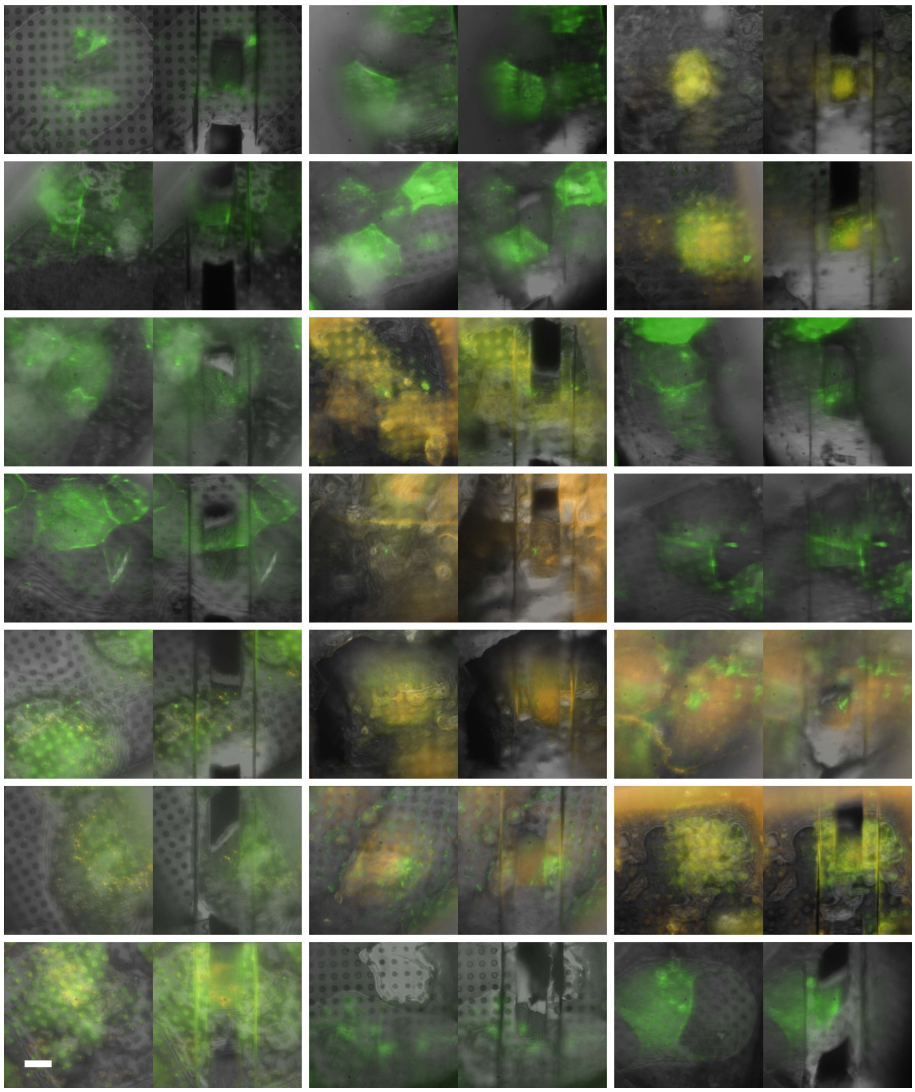

Figure S2: Fluorescent (colors) overlaid on reflected light (grayscale) image pairs as obtained by automated milling. For each set, the left image is acquired prior to rough milling and the right image after. Scale bar 10 µm.

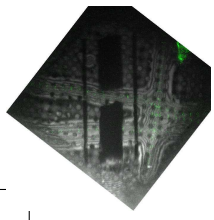

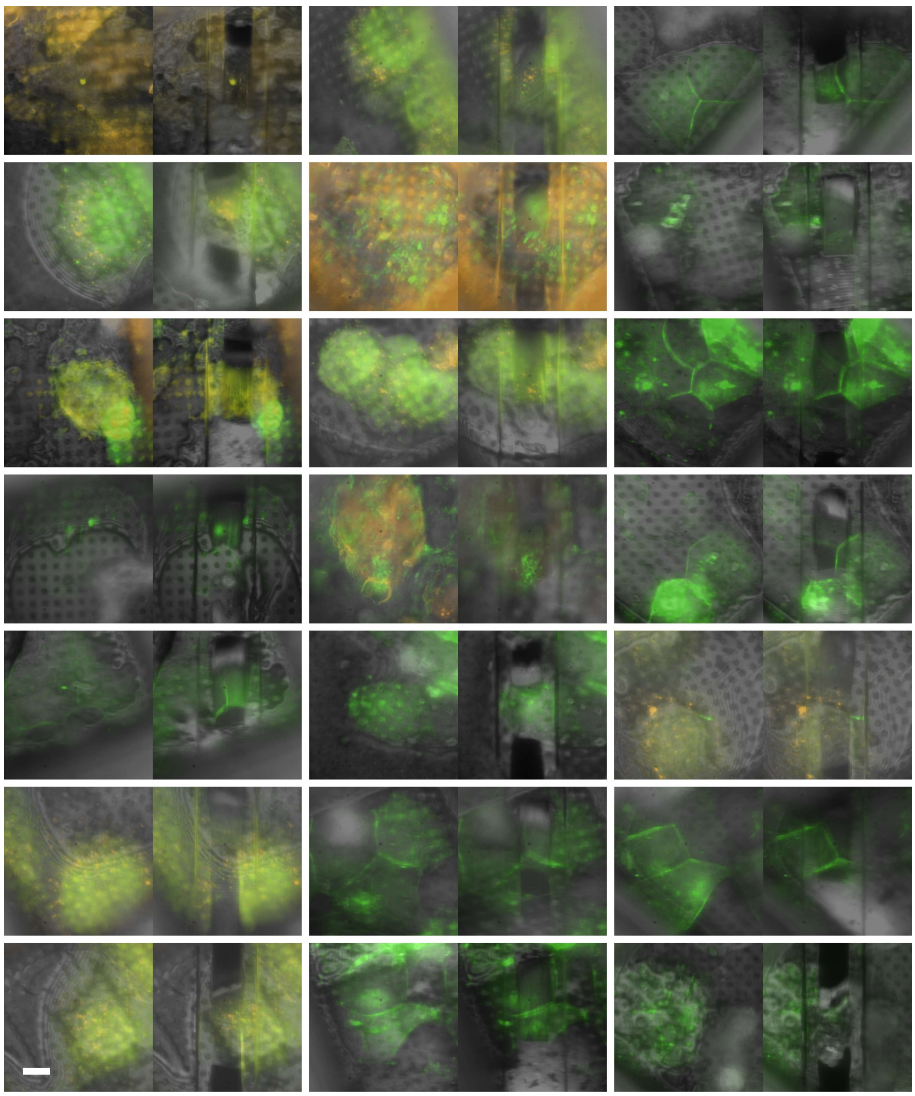

Figure S3: Fluorescent (colors) overlaid on reflected light (grayscale) image pairs as obtained by automated milling. For each set, the left image is acquired prior to rough milling and the right image after. Scale bar 10 µm.

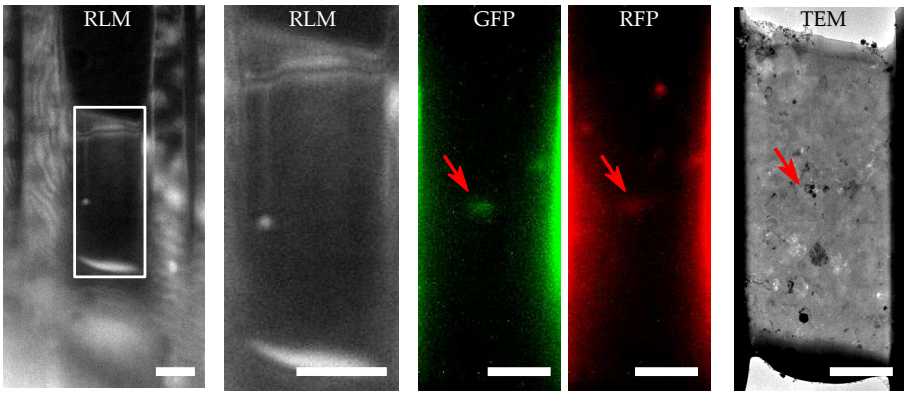

Figure S4: Fluorescence targeted lamella as fabricated for q4STEM thickness determination and verification with EFTEM. A red fluorescent protein (RFP)-GFP tandem fluorescent-tagged LC3 (mRFP-GFP-LC3) single molecule-based probe is used that can monitor the autophagosome maturation process Kimura et al., 2007b. **(a)** lamella as imaged with RLM after thinning with the FIB, and in **(b)** zoom from white rectangle. **(c)** Separated fluorescence microscopy channels, imaged after polishing (white rectangle from **(b)**), with target present (red arrows). From left to right: GFP emission (525 nm in green), and RFP emission (607 nm in orange). **(d)** Overview image as acquired in the TEM. All scale bars: 5 µm.

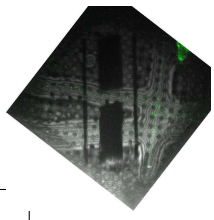

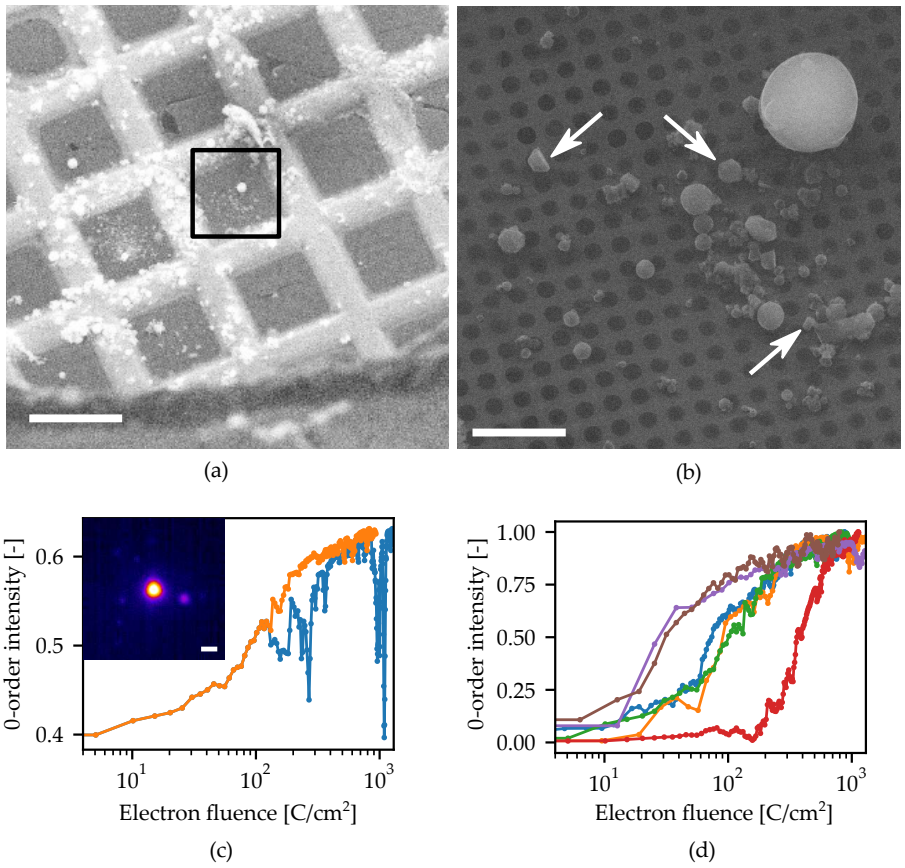

Figure S5: Assessment of radiolytic damage by q4STEM measurements. **(a)** Overview image of the EM grid containing small protein crystals. **(b)** The area as indicated in (a, black rectangle) shown at a larger magnification. White arrows denote the crystals which showed (partial) diffraction patterns. **(c)** With the optical focus set to the scintillator, the electron beam was moved over each crystal in search of a (partial) diffraction pattern (example shown in inset). Once found, a time-lapse acquisition was started, from which the 0-order intensity is plotted against electron fluence. The discontinuities seen in the blue trace originate from ~ 2 to 4 nm peak-to-peak sample vibrations, causing slightly different parts of the crystal to be exposed Daan B Boltje, Hoogenboom, Jakobi, Jensen, Jonker, Kaag, Koster, Last, Agrela Pinto, J. M. Plitzko, et al., 2022. By enforcing a monotonic increase, we filter and remove these discontinuities (orange trace). **(d)** Filtered 0-order intensity against electron fluence for different crystals, as indicated by the white arrows in (b). The electron fluence is determined through the estimated beam diameter (10 nm) and the set beam current (25 to 100 pA). Scale bars: **(a)** 100 µm, **(b)** 10 µm, **(c, inset)** 6 µm or 20 mrad.

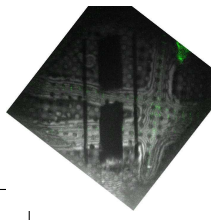

5

PROSPECTS AND IMPLEMENTATION IN STRUCTURAL BIOLOGY

This work presented a novel fluorescence targeted lamella fabrication workflow using integrated light, ion and electron microscopy, and described a progressive enhancement of cryo-ET sample preparation techniques. The introduction of a coincident, fluorescence-guided FIB milling setup (Chapter 2) allowed for unprecedented precision in targeting specific fluorescence labelled cellular structures, overcoming the limitations of earlier presented methods (Arnold et al., 2016; Gorelick et al., 2019; Smeets et al., 2021; ThermoFisher Scientific, 2021). A major technical challenge associated with using cryogenic fluorescence microscopy for targeting within frozen-hydrated cells is the axial deformation caused by refractive index mismatch between the sample and the imaging system. This deformation can lead to inaccuracies in identifying the correct depth at which structures of interest inside the cells are located, and thus to off-target milling and the fabrication and inspection of lamellae that do not contain the structure of interest. This was addressed by developing and validating a depth-dependent axial scaling correction method (Chapter 3). With the targeting precision and deformation correction in place, the final step was to ensure that the fabricated lamellae were of optimal thickness for electron tomography (i.e., 100 to 200 nm), and free from defects due to e.g. improper vitrification. This was achieved by implementing real-time light microscopy monitoring and feedback mechanisms during the milling process, ensuring that the lamellae produced were of the desired thickness and quality, ready for high-resolution imaging inside the TEM (Chapter 4). Collectively, these innovations have the potential to significantly improve the reliability and reproducibility of high-resolution structural biology studies, paving the way for more detailed insights into the molecular machinery of life, and affording several advantages.

(I) The integration of fluorescence-guided milling with real-time monitoring and feedback significantly increases the efficiency, ease of use, and success rate of preparing lamellae. To achieve high resolution in tomogram reconstructions, structure averaging on different lamellae is required, making it crucial to minimize the risk of spending valuable time on lamellae of insufficient quality or those that do not contain the region of interest, for both expensive human operator and machine time. Structure determination through tomogram reconstruction directly benefits from the efficiency gain, especially when studying i.e. interacting components or sparse regions of interest.

(II) Improved sample quality, precise targeting, and effective correction of imaging distortions, enable more detailed and accurate structural studies. This is par-

ticularly important for investigating dynamic processes within cells natively too thick for cryo-ET. Cells with different culture time points can be applied to different EM grids, and can be serially processed to fabricate lamellae. Consequently, the target inclusion reproducibility in different lamellae is detrimental to produce cryo-ET tomograms at different time points.

(III) Studies towards biomolecular condensation would benefit from precise targeting and high-resolution imaging as the structural changes of forming condensates are subtle (Boeynaems et al., 2018; Franzmann et al., 2019; Lasker et al., 2022; Mathieu et al., 2020). The field of visual proteomics was conceptualized before instrumentation was developed to enable it, and can still benefit significantly from advances in lamella fabrication techniques Beck et al., 2009; R. Kelley et al., 2024; Nickell et al., 2006. Increased throughput in creating these samples enables the combination of relatively lower resolution subtomogram averages with existing molecular models to accurately identify component proteins (Lucas, 2023). Additionally, by leveraging super-resolution fluorescence microscopy, it becomes possible to visualize protein conformations at nanometer resolution, allowing for the characterization of single instances within cells and correlating this with structural data (Berger et al., 2023; Guaita et al., 2022; Sexton et al., 2022).

Direct targeting from fluorescence imaging is particularly critical in understanding how interactions inside cells take place. For example, when studying dynamic cell processes, pharmaceutical drug delivery or how pathogens interact with and manipulate host cell structures. The techniques described facilitate the preparation of lamellae from specific regions of infected cells, allowing molecular-level studies of pathogen-host interactions. Exactly this is showcased in the next section, as this is under active investigation in collaboration with the group of Arjen Jakobi at the Kavli Institute of Nanoscience in Delft. Furthermore, preliminary data from another collaboration with the group of Dimphna Meijer on trans-synaptic protein complexes studies are also presented.

5.1 ULTRASTRUCTURE OF IMMUNE-DIRECTED GTPASES AROUND INTRACELLULAR PATHOGENS

The immune system employs a multitude of strategies to defend the body against microbial infections. Among these, the cell-autonomous immune response is the first line of defense to combat intracellular pathogens, organisms that invade and replicate within host cells (Randow et al., 2013). A key player in this defense is the family of guanylate binding proteins (GBPs), which are involved in various host-mediated immune effector functions in the defense against bacterial pathogens and parasites (Rivera-Cuevas et al., 2023).

GBP1 has emerged as the central organizer of the antibacterial activity of interferon-activated GBPs. (Fisch et al., 2020; Kutsch et al., 2020; Rivera-Cuevas et al., 2023; San-

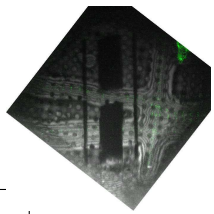

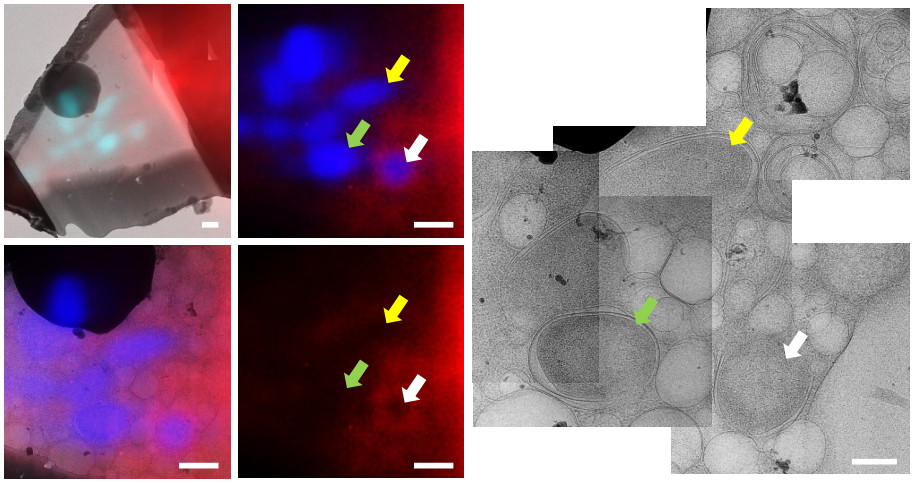

(a) (b) (c)

Figure 5.1: Preliminary data on the ultrastructure of both GBP1-coated, and non-coated cytosolic salmonella enterica serovar typhimurium (STM). (a) The top image shows the lamella imaged in the TEM, prepared through fluorescence targeting and monitoring. The two fluoresence channels, acquired after milling, are overlaid in blue (GFP, STM bacteria) and red (mCherry, overexpressed GBP1). The black ball is contamination originating from the transfer. The bottom image shows the central region magnified. (b) The fluorescence recordings acquired after milling (top - mCherry and GFP, bottom - mCherry only). Of the different salmonella enterica serovar typhimurium (STM) bacteria present, only one (white arrow) is coated with GBP1 as shown in the bottom image by the ring of mCherry fluorescence enveloping the bacterium. The arrows facilitate linking the different bacteria to the structural data as shown in (c), recorded in at 8000 × magnification in the TEM. Scale bars: (a) and (b) 1 µm, (c) 200 nm.

tos et al., 2018) by forming supramolecular complexes on the pathogen-containing vacuoles (PCVs), or directly on cytosol-invasive bacteria. In some case, GBP1 can contribute to the disruption of the PCVs or bacterial membranes, leading to release of pathogen-associated molecular pattern but the mechanism has remained controversial until recently. Cryo-EM studies on reconstituted systems have shown that GBP1 assembles on cytosol-dwelling Gram-negative bacteria and lipopolysaccharide (LPS), where its GTP activity promotes structural changes that disrupt the bacterial membrane to make LPS accessible for binding to inflammatory caspases(Kuhm et al., 2025), in turn triggering the onset of lytic cell death. While recent studies have established key aspects of the molecular mechanism of GBP1 activation and mega-complex assembly(Kuhm et al., 2025), ta full molecular-level comprehension of this pathway requires in situ structural studies in the native complexity of infected cells.

Here, we illustrate how utilizing the techniques developed in this thesis may help the further study of these mechanisms. HeLa cells overexpressing mCherry tagged GBP1 were infected with STM overexpressing green fluorescent protein (GFP). Lamellae containing (cytosolic) bacteria were milled from the plunge-frozen cells through fluorescent targeting and monitoring. Through the use of cryo-ET, we can study the ultrastructure of both the coated, and non-coated cytosolic STM, of which

preliminary data is presented in Figure 5.1. The lamella overview as acquired in the TEM is shown in the top image of Figure 5.1a, along with the fluorescent channels in overlay (blue for STM bacteria and red for overexpressed GBP1). The fluorescence channels are shown separated from the TEM data in Figure 5.1b, where multiple non-coated, along with a single GBP1-coated STM bacteria (white arrow) are visible . The three arrows facilitate linking to the TEM data recorded at higher magnification as shown in Figure 5.1c. Thus, we can now directly identify the different species in the tomogram data aiding to resolve the structural differences, which is research now ongoing at TU Delft. [1]

5.2 THE STRUCTURE OF SYNAPTIC CELL ADHESION MOLECULES

Proper functioning of the brain relies on the maintenance of accurate neural connections, with synapses acting as vital links. Synaptic cell adhesion molecules (CAMs) such as Teneurin, Latrophilin, FLRT, and N-cadherin play critical roles in neuronal development, axon guidance, synaptic assembly, and specificity regulation. Research into the molecular mechanisms of these CAMs is essential for understanding neuronal recognition at a molecular level. The project as envisioned by Dimphna Meijer aims to create a versatile and simplified minimal synapse model using chronic myelogenous leukemia lymphoblast (K562) cells. This model will allow to structurally examine key synaptic CAMs with increasing structural and functional complexity and explore the potential formation of macromolecular complexes in synaptic transcellular junctions. Through direct fluorescent labeling, targeting and monitoring of intercellular junctions organized by trans-synaptic CAM complexes, cryo-lamellae containing these junctions are prepared. They are then imaged through cryo-ET and utilized in a subtomogram averaging workflow to determine the structure of trans-synaptic CAM complexes.

A fluorescent label is added through electroporating non-adherent K562 cells with a Teneurin-4-GFP fusion protein construct. This leads to the formation of cell clusters, with a distinct GFP signal localized in the cell junction regions, indicating proper expression, localization, and cell adhesion ability of Teneurin-4 Figure 5.2a. The clustered cells were then directly applied to a glow-discharged EM grid and plunge-frozen. Cryo-lamella preparation was performed on cell clusters exhibiting a strong GFP signal in the junction. Throughout the milling steps, the fluorescence signal in the junction region was continuously monitored and the final lamellae, typically around 200 nm thick, contained the junction region marked by the presence of a GFP signal, see Figure 5.2b.

TEM data was collected on a Titan Krios microscope equipped with a Gatan K3 camera at the NeCEN cryo-EM facility in Leiden. During TEM data acquisition, tilt-series positions were chosen based on the cellular junction localization in the

1 This work has been done in collaboration with Clémence Taisne, Wiel Evers and Arjen Jakobi at the Kavli Institute of Nanoscience in Delft. CT prepared the cellular samples and together with DBB performed cryo-FIB milling. cryo-ET experiments were carried out by CT and WHE.

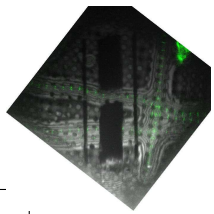

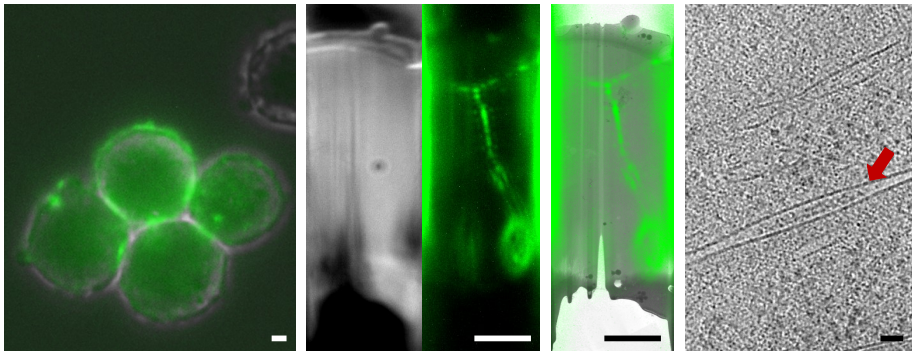

(a) (b) (c) (d)

Figure 5.2: Preliminary data on the intercellular junction expansion and protein density between K562 cells clusters expressing Teneurin-4-GFP. (a) Cell clusters with a distinct GFP signal (green) localized in the cell junction regions. (b) Reflected light image (left) of the lamellae as prepared around 200 nm thick, containing the junction region marked by the presence of a GFP signal (right). (c) TEM overview image of the lamella, along with the cellular junction localization (overlay in green). (d) Reconstructed tomogram slice showing the intercellular junction, having a characteristic junction width expansion and protein density (red arrow). Scale bars: (a), (b) and (c) 5 µm, (d) 50 nm.

cryo-lamellae, see the overlay in Figure 5.2c. The reconstructed tomogram slice as shown in Figure 5.2d shows the intercellular junction, having a characteristic junction width expansion and protein density, which are likely associated with Teneurin-4 complexes (red arrow). Going forward we aim to prepare more lamellae containing the junctions, and acquire multiple tomograms on each lamella. This will allow to collect enough data for subtomogram particle picking and averaging, thus building a versatile and simplified minimal synapse model is within grasp. [2]

5.3 OUTLOOK AND VALORIZATION

The system presented has been designed and built in close collaboration with Delmic B.V. Three identical systems have been constructed and are currently in use in different laboratories: (i) the Centre for Microscopy and Microanalysis at the University of Queensland, (ii) SLAC National Accelerator Laboratory at Stanford University, and (iii) the Department of Imaging Physics at Delft University of Technology. The different groups are working on their own ongoing research in structural biology and are involved in further developing the technology, but there are challenges that remain unaddressed. One key concern is the operation time of about 8 to 10 h. Although this may not be an immediate issue if the maximum number of lamellae obtainable from a single EM grid is around ten (achievable in a one-day run), it could become limiting in for example photo-micropatterning of EM grids for site-specific deposition of

2 This work has been done in collaboration with Leanid Kresik, Joyce Van Loenhout and Dimphna Meijer at the Kavli Institute of Nanoscience in Delft. LK and JVL prepared the cellular samples and together with DBB performed cryo-FIB milling. cryo-ET experiments were carried out by LK and JVL.

cells, where 30 to 40 well positioned cells could yield the same number of lamellae (Toro-Nahuelpan et al., 2020). In such scenarios, extending the operation time and implementing automated overnight milling could greatly enhance productivity. Over the past two years, DEMCON Kryoz has continued the development of the microcooler, extending its uptime to about 80 h. For this to be implemented *in-situ*, the system would first need rigorous testing for potential issues such as vibrations, vacuum compatibility, and drift. As such it could provide a viable improvement, but still requires a substantial effort and validation.

The long-term robustness of the system also remains an open question. Our system has been installed and operated for about 48 to 52 weeks in total over the past 4 years. Based on this, it is difficult to estimate the service intervals for critical components such as the piezo positioning stage and the microcooler. Another aspect to consider is the robustness of the individual components and the system as a whole if this system was to be produced on a larger scale. The microcooler, kinematic positioning stage, and transfer system remain relatively fragile and require an expert operator. As the system was designed with a high degree of flexibility in mind, a design iteration focusing on handling robustness and hardware simplification could in fact mitigate this.

The current coincident configuration presents another potential drawback as the objective lens is positioned below the sample. This works well for cells on EM grids but is incompatible with holders designed for HPF, such as those used in waffle preparation (K. Kelley et al., 2022). By placing the light microscope objective lens on the same side as the SEM and FIB lenses this issue could be avoided. Such configuration would also work well with new techniques like serial lift-out, which are rapidly gaining popularity (Schiøtz et al., 2023; Schneider et al., 2024; Zens et al., 2024). However, for cells, the current design with the objective below the sample could still be advantageous due to the flat air-water interface it provides. In addition, q4STEM only works with the objective lens below the sample thus, while the presented system provides many advantages, specific scenarios call for a re-evaluation of its configuration and further development to overcome these limitations.

The methods described in this thesis can be directly utilized by multiple other coincident systems which have been developed in recent years, such as the ELI trifocal microscope and the Arctis Cryo-Plasma FIB from TFS (S. Li et al., 2023; W. Li et al., 2023; ThermoFisher Scientific, 2024). In addition, Delmic B.V. has developed their METEOR platform (Smeets et al., 2021), a retrofittable light microscope mounted on the top side of the dual-beam chamber, using optics similar to those in the system presented. This platform requires repositioning the sample position stage between milling and light microscopy imaging. Despite this, the monitoring techniques described in this thesis can be integrated into the METEOR system (and others like it) through more advanced software automation.

Looking ahead, there are several avenues for pushing the capabilities of the current system. First, by advancing superresolution localization capabilities toward

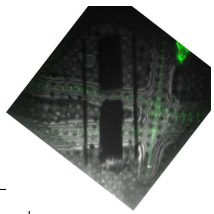

superresolution imaging, it can reduce the current resolution gap with cryo-EM (Berger et al., 2023). Such a correlation could provide unprecedented insight into the structural and functional relationships within biological specimens. For example, this would allow for more direct studies of protein-protein interaction networks, or this combined approach could help visualize the effects of drugs or therapies at the molecular level within cells (Byron et al., 2015; Subramaniya et al., 2021). It should be noted that the quantitative astigmatic localization precision of about 10 to 20 nm using astigmatic localization has still to be shown and relatively sparse labelling is a requirement.

Secondly, the thickness of the frozen hydrated lamella might be inferred through a secondary electron yield signature that changes with the thickness of the ice. A key advantage of this approach is that it is broadly applicable and practical, as it does not require any additional hardware beyond what is conventionally available in FIB-SEM systems. To achieve this, a clever detection geometry would need to be designed along with extensive and validation testing under different (imaging) conditions.

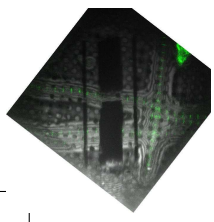

6 CONCLUSION

We have developed an innovative coincident three-beam microscope designed specifically for sample preparation in the cryo-electron tomography workflow, significantly enhancing the efficiency and precision of lamella fabrication. This system enables direct light microscopy targeting during lamella milling, eliminating the need for stage repositioning or fiducial markers. The five-channel inverted epi-fluorescent light microscope allows real-time monitoring of the fluorescence signal from the lamella during the milling process, ensuring that the target area remains contained within the lamella. Any misalignment can be immediately identified and corrected, enhancing the accuracy of the procedure. Cryogenic temperatures of the sample are maintained through a novel liquid nitrogen-free cooling design, which minimizes vibrations and drift, and provides an uptime exceeding nine hours. The entire system is seamlessly integrated into a standard focused ion beam scanning electron microscope, effectively transforming it into a cryo-light microscopy FIB-SEM system.

As frozen hydrated cells are imaged using an optical objective contained in vacuum, a refractive index mismatch is present, and so in addition to the hardware developments, we have introduced an analytical theory predicting that a depth-dependent axial deformation is encountered due to this mismatch. The re-scaling factor can be computed as a function of depth, based on imaging parameters such as the numerical aperture, the refractive indices of the objective and the sample, and the wavelength of light used. Wave-optics calculations have validated the theory, showing excellent agreement between the predicted and observed results and are further supported through experimental measurements of axial scaling. To facilitate the use of this theory, we have developed a web applet for users to calculate the re-scaling factor based on their specific imaging parameters. This is of particular interest when refractive indices cannot be matched, as is the case in cryo-correlative light and electron microscopy in general and our integrated FM-FIB-SEM in particular.

To further improve the sample preparation workflow, we present three methods to accurately determine lamella thickness during focused ion beam milling, using the integrated light microscope within the FIB-SEM system. By selecting a scintillator more suitable for fluorescence microscopy, we applied a previously established quantitative 4D-STEM technique to the cryogenic lamella fabrication process, showing good agreement with thickness measurements from energy filtered transmission electron microscopy. In addition, we estimated lamella thickness during milling based on the known geometry of the milling and imaging setup, which produced reliable estimates in the range of 400 to 2000 nanometers. Lastly, we exploited thin-

film interference phenomena on a per-pixel basis to generate detailed thickness maps of the lamella, providing quantitative feedback on lateral thickness variations. These estimates were validated against thickness measurements from reconstructed TEM data, showing excellent agreement.

To increase the lamellae yield, we demonstrate a fluorescent targeting and focused ion beam milling strategy which corrects for axial distortion caused by refractive index mismatch when imaging into a frozen cell. Reflective light microscopy is used to inspect milling sites and eliminate those with parasitic ice beneath the electron microscope grid. Through a basic communication protocol between the FIB and fluorescence microscope control systems, we demonstrate automated rough milling of fluorescent targets. Our methods provide live feedback on the thickness and uniformity of the lamella, the integrity of the platinum coating layer, and the presence of the fluorescent target during the preparation of a lamella from a frozen hydrated cell. This approach simplifies the milling process and significantly increases the success rate of producing lamellae suitable for high-resolution cryo-EM analysis. Our procedures advance the automation and routine fabrication of frozen-hydrated cellular sections and underscore the potential advantages of coincident FM-FIB-SEM instruments in the lamella preparation workflow for cryogenic electron tomography, as is shown by the ongoing collaborative structural biology projects.

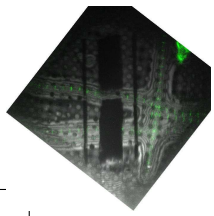

ACKNOWLEDGMENTS

First and foremost, I wish to express my gratitude to my promoter and supervisor, *Jacob Hoogenboom*. I am thankful for the opportunity to continue working with the system developed at Delmic, now within an academic environment. It has allowed me to explore new scientific frontiers, and I am particularly appreciative of the incredible freedom I was given throughout this journey — a freedom that I have come to value more and more as time went on. I would also like to extend my heartfelt thanks to *Arjen Jakobi*, my second promoter, whose opportunistic and dynamic approach to science as a group leader has been a source of inspiration. Despite your consistently overbooked agenda, it has been both amazing and joyful to see how you find your way into the lab, often procrastinating from other responsibilities. Your hands-on involvement is something I truly admire.

My sincere thanks also go to *Sander den Hoedt*, CEO of Delmic, for supporting this entire endeavor. Your willingness to allow me to pursue this academic path has been instrumental in bringing this thesis to fruition.

I would like to acknowledge the fantastic team at Delmic that I had the pleasure of working with when I first joined: magnetron-Wouter, strakke-planga-Thomas, altijd-vrolijke-Thera, fjeze-fur-Ferry, mastermind-Toon, gaan-met-die-banaan-Sangeetha, one-of-the-guys-Noor, oldtimer-Daan, wizard-Eric, classical-Anders, and later on raketje-Marre, astigmatic-Deniz, enzel-Wessel, ferrari-Guido, snelle-Kornee, centrale-verwarming-Caspar, eigenwijze-Mart, AI-Anish, motor-Ronald, klieren-met-ethaan-Bas and wiwa/o-Wilco. PECCAK-Andries, thank you for your support when things were rough and, of course, for teaching me the meaning of PEBCAK.

At DEMCON-kryoz I would like to thank Pieter Lerou, Erik-Jan de Hoon and Bart Schepers for their technical support, the joint development and testing of the microcooler; an achievement which is at the heart of the research presented.

The initial validation experiments were conducted at the Department of Structural Biochemistry at the Max Planck Institute of Molecular Physiology in Dortmund. I would like to thank Stefan, Sebastian, Zhexin, and Oliver for the fruitful collaboration and technical support. Together with Mart and Caspar from Delmic, we made it work given the constraints imposed by the pandemic.

To my colleagues at the TU Delft, I am grateful for your companionship and support. Thank you, Arent, Stijn, Martijn, Mike, Myron, Yoram, Matthijs, Aditi, Laura, Xin and Marco. The ever-inimitable Sergey, thank you for your unique insights. Cristiano, our shared love for Italodisco still makes me smile. And to my great American friend, Ryan, thank you for teaching me about the equestrian, and introducing me to the nuances of American language, although I still don't know what's wrong with chocolate tart. Last but not least Ernest, we bonded immediately over newfound parenthood, painting houses, and hands-on weeks in the lab. You taught me loads

about optical microscopes and their characterization — thank you for your curiosity and camaraderie throughout.

I would also like to express my appreciation to the team at the Bionanoscience department in Delft, who have been instrumental in helping me navigate the intricate world of (structural) biology. Wiel, your guidance and help in cryo-TEM has been invaluable along with of course, 3D printing anything and everything. Clemence, Leanid, and Stefan thank you for all of the sample preparation and milling sessions, and for your unconstrained enthusiasm when spotting some intracellular structure in the TEM. Cecilia, your seemingly perpetual happiness has been a bright spot in the lab, lifting the spirits of everyone around you.

A special thanks to the students in the Hoogenboom lab: Tristan, Magda, Max, and Reint. Your curiosity and enthusiasm have been a constant source of motivation. I would like to acknowledge the incredible technical support team at the university: Johan, Carel, Ruud, Han, Youp, Martin, Dustin, Anjella, Yvonne, Malee, Anneloes, and Hannah. Your expertise and assistance have been critical to the success of this project, and I am grateful for your dedication and patience.

An industrial doctoral track sounds great in theory, but the transition to direct valorization proved more challenging than I had anticipated. That is why I would like to express my sincere thanks to Peter Dahlberg and his team at SLAC for their enthusiastic response and feedback when using the system. Your support gave me a boost in finalizing the last experiments and thesis.

While not directly related to this thesis, I would still like to express my gratitude to Jan Aarts for sending me that email all those years ago, encouraging me to apply as a research technician at Leiden University. It opened the door to an incredible learning experience, especially under the guidance of Marcel Hesselberth, from whom I gained a wealth of technical knowledge and developed a synergetic approach between science and engineering. This experience set me on a non-traditional educational path — one that, in hindsight, I am deeply thankful for.

Nog wat verder terugkijkend in de tijd wil ik graag Marian en Gerard bedanken voor de vrijheid die ik van kleins af aan kreeg om dingen zelf te ondernemen. Van computers tot brommers en later studiekeuze, jullie hebben mij altijd gestimuleerd om het zelf uit te zoeken. Joost en Thomas, we gaan al heel wat jaren met elkaar mee, en ik geniet intens van jullie als broers. Of we nu samen op reis gaan of iets aan het verbouwen zijn, jullie zorgen er altijd voor dat ik weer opgeladen ben en er weer tegenaan kan, dankjulliewel.

Lieve Boaz en Sam, jullie stellen mij onophoudelijk de leukste vragen, zijn altijd nieuwsgierig en verassen me vaak, daar haal ik veel plezier uit en ik hoop dat jullie dat nog lang blijven doen. Allerliefste Thanja, inmiddels hebben we er aardig wat avonturen op zitten, van heel leuk naar verdrietig en alles ertussen in. Ik wil je bedanken voor 11 jaar ondersteuning van een 17 jarig promotietraject. Jij bent een integraal onderdeel van mijn leven en ik wil je nooit kwijtraken.

CURRICULUM VITÆ

DAAN BENJAMIN BOLTJE

25-04-1987 Born in Almere, The Netherlands.

EDUCATION

2020–2025 Ph.D. in Physics
Delft University of Technology
Delft, The Netherlands

2015–2017 M.Sc. in Physics
Universität Stuttgart
Stuttgart, Germany

2004–2008 B.Eng. in Applied Physics (cum laude)
Technische Hogeschool Rijswijk
Rijswijk, The Netherlands

WORK EXPERIENCE

2024–present System architect
QuantaMap B.V.
Leiden, The Netherlands

2018–2024 Experimental physicist & System architect
Delmic B.V.
Delft, The Netherlands

2009–2015 Research Technician in Quantum Matter and Optics
Leiden University
Leiden, The Netherlands

SELECT PUBLICATIONS

Boltje, D. B., Skoupỳ, R., Taisne, C., Evers, W. H., Jakobi, A. J., Hoogenboom, J. P., (2025). "Thickness-and quality-controlled fabrication of fluorescence-targeted frozen-hydrated lamellae." In: *Cell Reports Methods* 5.3.

Perton, E. G., Boltje, D. B., Jakobi, A. J., Hoogenboom, J. P., (2025). "Workflow for Targeted Lamella Milling with a Coincident Fluorescence, Electron, and Ion Beam Microscope." *Invited draft, submitted at Bio-protocol.*

Loginov, S., Boltje, D. B., Hensgens, M. N., Hoogenboom, J. P., Van Der Wee, E., (2024). "Depth-dependent scaling of axial distances in light microscopy." In: *Optica* 11.4, pp. 553–568.

Sica Jr, A. V., Zaoralova, M., Antolini, C., Boltje, D. B., Penzes, J. J., Malmqvist, L. M., Jensen, G. J., Jason, K. T., Dahlberg, P., (2024). "Optical Interference for the Guidance of Cryogenic Focused Ion Beam Milling Beyond the Axial Diffraction Limit." *submitted*. Preprint at *bioRxiv* pp. 2024-11.

Skoupỳ, R., Boltje, D. B., Slouf, M., Mrázová, K., Láznička, T., Taisne, C. M., Krzyžánek, V., Hoogenboom, J. P., Jakobi, A. J., (2023). "Robust Local Thickness Estimation of Sub-Micrometer Specimen by 4D-STEM." In: *Small Methods*, p. 2300258.

Tebyani, A., Schramm, S., Hesselberth, M., Boltje, D. B., Jobst, J., Tromp, R., Molen, S. J., (2023). "Low energy electron microscopy at cryogenic temperatures." In: *Ultramicroscopy* 253, p. 113815.

Boltje, D. B., Hoogenboom, J. P., Jakobi, A. J., Jensen, G. J., Jonker, C. T., Kaag, M. J., Koster, A. J., Last, M. G., Agrela Pinto, C., Plitzko, J. M., (2022). "A cryogenic, coincident fluorescence, electron, and ion beam microscope." In: *eLife* 11, e82891.

Wee, E. B., Boltje, D. B., Jakobi, A. J., Hoogenboom, J. P., (2022). "3D Fluorescence Localization in Frozen Cells for Targeted Lamella Milling for Electron Cryo-Tomography." In: *Microscopy and Microanalysis* 28.S1, pp. 1308–1309.

Gräfe, J., Groß, F., Ilse, S. E., Boltje, D. B., Muralidhar, S., Goering, E. J., (2021). "LeXtender: a software package for advanced MOKE acquisition and analysis." In: *Measurement Science and Technology* 32.6, p. 067002.

Dildar, I., Boltje, D. B., Hesselberth, M., Beekman, C., Aarts, J., (2018). "Mitigating target degradation in sputtering manganite thin films." In: *Vacuum* 148, pp. 131–135.

Dildar, I., Boltje, D. B., Hesselberth, M., Aarts, J., (2016). "Mesoscopic transport in thin films of La0. 67Sr0. 33MnO3." In: *Thin Solid Films* 598, pp. 305–310.

Mattoni, G., Zubko, P., Maccherozzi, F., Torren, A. J., Boltje, D. B., Hadjimichael, M., Manca, N., Catalano, S., Gibert, M., Liu, Y., (2016). "Striped nanoscale phase separation at the metal–insulator transition of heteroepitaxial nickelates." In: *Nature communications* 7.1, pp. 1–7.

Dildar, I., Neklyudova, M., Xu, Q., Zandbergen, H., Harkema, S., Boltje, D. B., Aarts, J., (2015). "Growing LaAlO3/SrTiO3 interfaces by sputter deposition." In: *AIP advances* 5.6, p. 067156.

Verhagen, T., Boltje, D. B., Ruitenbeek, J., Aarts, J., (2014). "Magnetic properties of Sm-Co thin films grown on MgO (100) deposited from a single alloy target." In: *Journal of Applied Physics* 116.5, p. 053903.

Dildar, I., Boltje, D. B., Hesselberth, M., Aarts, J., Xu, Q., Zandbergen, H., Harkema, S., (2013). "Non-conducting interfaces of LaAlO3/SrTiO3 produced in sputter deposition: the role of stoichiometry." In: *Applied physics letters* 102.12, p. 121601.

IM, D., Boltje, D. B., Hesselberth, M., Xu, Q., Zandbergen, H., Harkema, S., Aarts, J., (2012). "Conductivity of LaAlO3/SrTiO3 interfaces made by sputter deposition." In: *e-Journal of surface science and nanotechnology* 10, pp. 619–623.

Heijne, E., Ballabriga, R., Boltje, D. B., Campbell, M., Idarraga, J., Jakubek, J., Leroy, C., Llopart, X., Tlustos, L., Plackett, R., (2010). "Vectors and submicron precision: redundancy and 3D stacking in silicon pixel detectors." In: *Journal of Instrumentation* 5.06, p. C06004.

Hattum, E., Boltje, D. B., Palmero, A., Arnoldbik, W., Rudolph, H., Habraken, F., (2008). "On the argon and oxygen incorporation into SiOx through ion implantation during reactive plasma magnetron sputter deposition." In: *Applied Surface Science* 255.5, pp. 3079–3084.

PATENTS

Skoupy, R., Boltje, D. B., Jakobi, A. J., Hoogenboom, J., (2022). "Method and apparatus for in-situ sample quality inspection in cryogenic focused ion beam milling." NL Patent 2 032 641. Technische Universiteit Delft. Filed Jul. 2022, IDF filed Jun. 2022.

Van Der Wee, E., Boltje, D. B., Hoogenboom, J., (2022). "Method for localizing a region of interest in a sample and micromachining the sample using a charged particle beam." NL Patent 2 032 640. Technische Universiteit Delft. Filed Jul. 2022, IDF filed Jun. 2022.

Boltje, D. B., Last, M., Smeets, M., Jonker, C., Zielinski, M., (2021). "Method and apparatus for micromachining a sample using a Focused Ion Beam." NL Patent 2 028 497. Delmic IP B.V. Filed Jun. 2021, IDF filed Jun. 2021.

SOFTWARE REPOSITORIES

Wee, E. B., Boltje, D. B., Loginov, S., (June 2023). *Re-scaling factor online plotting tool*. Version 0.1. URL: https://github.com/hoogenboom-group/SF.

Boltje, D. B., Last, M. F. G., (June 2022). *Mechanical-Analysis*. Version 0.1. URL: https://github.com/hoogenboom-group/Mechanical-Analysis.

Boltje, D. B., Wee, E. B., Lane, R., (June 2022). *PSF-Extractor*. Version 0.1. URL: https://github.com/hoogenboom-group/PSF-Extractor.

PUBLISHED DATASETS

Boltje, D. B., Skoupy, R., Taisne, C., Evers, W., Jakobi, A. J., Hoogenboom, J. P., (2025). *Data underlying the publication: Thickness and quality controlled fabrication of fluorescence-targeted frozen-hydrated lamellae*. DOI: 10.4121/aeb7cf17-1b4a-4f09-a2fb-88d7875c672d.

Loginov, S., Boltje, D. B., Hensgens, M. N., Hoogenboom, J. P., Wee, E., (2024). *Data underlying the publication: Depth-dependent scaling of axial distances in light microscopy*. DOI: 10.4121/ebdd9ff7-5797-406f-a512-abae2102a021.v1.

Boltje, D. B., Hoogenboom, J. P., Jakobi, A. J., Jensen, G. J., Jonker, C. T., Kaag, M. J., Koster, A. J., Last, M. G., Agrela Pinto, C., Plitzko, J. M.
bibinitperiod o., (2022). *Data underlying the publication: A cryogenic, coincident fluorescence, electron and ion beam microscope*. DOI: 10.4121/20787274.v1.

BIBLIOGRAPHY

Abellan, Patricia, Eric Gautron, and Jay A LaVerne (2023). "Radiolysis of Thin Water Ice in Electron Microscopy." In: *The Journal of Physical Chemistry C* 127.31, pp. 15336–15345.

Alberts, B., A. Johnson, J. Lewis, P. Walter, M. Raff, and K. Roberts (2002). *Molecular Biology of the Cell 4th Edition: International Student Edition*. Routledge. ISBN: 9780815332886. URL: https://books.google.nl/books?id=ozigkQEACAAJ.

Ando, Toshio, Satya Prathyusha Bhamidimarri, Niklas Brending, H Colin-York, Lucy Collinson, Niels De Jonge, PJ De Pablo, Elke Debroye, Christian Eggeling, Christian Franck, et al. (2018). "The 2018 correlative microscopy techniques roadmap." In: *Journal of physics D: Applied physics* 51.44, p. 443001.

Arnold, Jan, Julia Mahamid, Vladan Lucic, Alex De Marco, Jose-Jesus Fernandez, Tim Laugks, Tobias Mayer, Anthony A Hyman, Wolfgang Baumeister, and Jürgen M Plitzko (2016). "Site-specific cryo-focused ion beam sample preparation guided by 3D correlative microscopy." In: *Biophysical journal* 110.4, pp. 860–869.

Aronova, MA, AA Sousa, and RD Leapman (2011). "EELS characterization of radiolytic products in frozen samples." In: *Micron* 42.3, pp. 252–256.

Basgall, EJ and D Nicastro (2006). "Cryo-Focused Ion Beam preparation of biological materials for retrieval and examination by cryo-TEM." In: *Microscopy and Microanalysis* 12.S02, pp. 1132–1133.

Beck, Martin, Johan A Malmström, Vinzenz Lange, Alexander Schmidt, Eric W Deutsch, and Ruedi Aebersold (2009). "Visual proteomics of the human pathogen Leptospira interrogans." In: *Nature methods* 6.11, pp. 817–823.

Berger, Casper, Navya Premaraj, Raimond BG Ravelli, Kèvin Knoops, Carmen López-Iglesias, and Peter J Peters (2023). "Cryo-electron tomography on focused ion beam lamellae transforms structural cell biology." In: *Nature Methods* 20.4, pp. 499–511.

Besseling, Thijs Herman, Jissy Jose, and A Van Blaaderen (2015). "Methods to calibrate and scale axial distances in confocal microscopy as a function of refractive index." In: *Journal of microscopy* 257.2, pp. 142–150.

Blahuta, S, A Bessiere, B Viana, P Dorenbos, and V Ouspenski (2013). "Evidence and Consequences of Ce^{4+} in LYSO: Ce, Ca and LYSO: Ce, Mg Single Crystals for Medical Imaging Applications." In: *IEEE Transactions on Nuclear Science* 60.4, pp. 3134–3141.

Boeynaems, Steven, Simon Alberti, Nicolas L Fawzi, Tanja Mittag, Magdalini Polymenidou, Frederic Rousseau, Joost Schymkowitz, James Shorter, Benjamin Wolozin, Ludo Van Den Bosch, et al. (2018). "Protein phase separation: a new phase in cell biology." In: *Trends in cell biology* 28.6, pp. 420–435.

Boltje, Daan B, Jacob P Hoogenboom, Arjen J Jakobi, Grant J Jensen, Caspar TH Jonker, Max J Kaag, Abraham J Koster, Mart GF Last, Cecilia de Agrela Pinto, Jürgen M Plitzko, et al. (2022). "A cryogenic, coincident fluorescence, electron, and ion beam microscope." In: *Elife* 11, e82891.

Boltje, Daan B, Jacob P Hoogenboom, Arjen J Jakobi, Grant J Jensen, Caspar TH Jonker, Max J Kaag, Abraham J Koster, Mart GF Last, Cecilia de Agrela Pinto, and Jürgen M & others Plitzko (2022). *Data underlying the publication: A cryogenic, coincident fluorescence, electron and ion beam microscope*. DOI: 10.4121/20787274.v1.

Boltje, Daan Benjamin, Ernest Benjamin van der Wee, and Ryan Lane (June 2022). *PSF-Extractor*. Version 0.1. URL: https://github.com/hoogenboom-group/PSF-Extractor.

Buckley, Genevieve, Gediminas Gervinskas, Cyntia Taveneau, Hariprasad Venugopal, James C Whisstock, and Alex de Marco (2020). "Automated cryo-lamella preparation for high-throughput in-situ structural biology." In: *Journal of structural biology* 210.2, p. 107488.

Byron, Olwyn and Bente Vestergaard (2015). "Protein–protein interactions: A supramolecular phenomenon demanding trans-disciplinary biophysical approaches." In: *Current opinion in structural biology* 35, pp. 76–86.

Carlsson, K (1991). "The influence of specimen refractive index, detector signal integration, and non-uniform scan speed on the imaging properties in confocal microscopy." In: *Journal of Microscopy* 163.2, pp. 167–178.

Chalfie, Martin, Yuan Tu, Ghia Euskirchen, William W Ward, and Douglas C Prasher (1994). "Green fluorescent protein as a marker for gene expression." In: *Science* 263.5148, pp. 802–805.

Chiang, Elaine Y, Andrés Hidalgo, Jungshan Chang, and Paul S Frenette (2007). "Imaging receptor microdomains on leukocyte subsets in live mice." In: *Nature methods* 4.3, pp. 219–222.

Conlan, AP, E Tillotson, A Rakowski, D Cooper, and SJ Haigh (2020). "Direct measurement of TEM lamella thickness in FIB-SEM." In: *Journal of Microscopy* 279.3, pp. 168–176.

Crytur (2023). *Scintillator physical properties*. https://www.crytur.com/materials/yagce/ (Retrieved 14-09-2023).

Dalle-Donne, Isabella, Giancarlo Aldini, Marina Carini, Roberto Colombo, Ranieri Rossi, and Aldo Milzani (2006). "Protein carbonylation, cellular dysfunction, and disease progression." In: *Journal of cellular and molecular medicine* 10.2, pp. 389–406.

De Boer, Pascal, Jacob P Hoogenboom, and Ben NG Giepmans (2015). "Correlated light and electron microscopy: ultrastructure lights up!" In: *Nature methods* 12.6, pp. 503–513.

DEMCON-kryoz (2021). *DEMCON kryoz – Kryoz Technologies*. https://www.demcon-kryoz.nl/ (Retrieved 13-09-2021).

Diaspro, Alberto, Federico Federici, and Mauro Robello (2002). "Influence of refractive-index mismatch in high-resolution three-dimensional confocal microscopy." In: *Applied optics* 41.4, pp. 685–690.

Dickerson, Joshua L, Peng-Han Lu, Dilyan Hristov, Rafal E Dunin-Borkowski, and Christopher J Russo (2022). "Imaging biological macromolecules in thick specimens: the role of inelastic scattering in cryoEM." In: *Ultramicroscopy* 237, p. 113510.

Diel, Erin E, Jeff W Lichtman, and Douglas S Richardson (2020). "Tutorial: avoiding and correcting sample-induced spherical aberration artifacts in 3D fluorescence microscopy." In: *Nature protocols* 15.9, pp. 2773–2784.

Donnald, Samuel B, Richard Williams, Charles L Melcher, Fang Meng, Merry Koschan, Stephan Friedrich, Jesse A Johnson, and Jason P Hayward (2018). "Correlation of nonproportionality and scintillation properties with cerium concentration in YAlO 3: Ce." In: *IEEE Transactions on Nuclear Science* 65.5, pp. 1218–1225.

Dowell, LG and AP Rinfret (1960). "Low-temperature forms of ice as studied by X-ray diffraction." In: *Nature* 188.4757, pp. 1144–1148.

Drouin, Dominique, Alexandre Réal Couture, Dany Joly, Xavier Tastet, Vincent Aimez, and Raynald Gauvin (2007). "CASINO V2. 42—a fast and easy-to-use modeling tool for scanning electron microscopy and microanalysis users." In: *Scanning: The Journal of Scanning Microscopies* 29.3, pp. 92–101.

Drozdowski, Winicjusz, Andrzej J Wojtowicz, Tadeusz Łukasiewicz, and Jarosław Kisielewski (2006). "Scintillation properties of LuAP and LuYAP crystals activated with Cerium and Molybdenum." In: *Nuclear Instruments and Methods in Physics Research Section A: Accelerators, Spectrometers, Detectors and Associated Equipment* 562.1, pp. 254–261.

Dubochet, J and AW McDowall (1981). "Vitrification of pure water for electron microscopy." In: *Journal of Microscopy* 124.3, pp. 3–4.

Dunst, Sebastian and Pavel Tomancak (2019). "Imaging flies by fluorescence microscopy: principles, technologies, and applications." In: *Genetics* 211.1, pp. 15–34.

Egner, Alexander and Stefan W Hell (2006). "Aberrations in confocal and multi-photon fluorescence microscopy induced by refractive index mismatch." In: *Handbook of biological confocal microscopy*, pp. 404–413.

Fisch, Daniel, Barbara Clough, Marie-Charlotte Domart, Vesela Encheva, Hironori Bando, Ambrosius P Snijders, Lucy M Collinson, Masahiro Yamamoto, Avinash R Shenoy, and Eva-Maria Frickel (2020). "Human GBP1 differentially targets Salmonella and Toxoplasma to license recognition of microbial ligands and caspase-mediated death." In: *Cell reports* 32.6.

Frank, Joachim (2015). "Generalized single-particle cryo-EM–a historical perspective." In: *Journal of Electron Microscopy* 65.1, pp. 3–8.

Franzmann, Titus M and Simon Alberti (2019). "Protein phase separation as a stress survival strategy." In: *Cold Spring Harbor perspectives in biology* 11.6, a034058.

Fujiwara, Eric, Thiago D Cabral, Miko Sato, Hiromasa Oku, and Cristiano MB Cordeiro (2020). "Agarose-based structured optical fibre." In: *Scientific reports* 10.1, p. 7035.

Gamow, George and Martynas Yčas (1968). *Mr. Tompkins inside himself: adventures in the new biology*. London, UK: George Allen and Unwin.

Ganten, Detlev and Klaus Ruckpaul (2006). *Encyclopedic reference of genomics and proteomics in molecular medicine*. Springer.

Gest, Howard (2004). "The discovery of microorganisms by Robert Hooke and Antoni Van Leeuwenhoek, fellows of the Royal Society." In: *Notes and records of the Royal Society of London* 58.2, pp. 187–201.

Gordon, Ronald E (2014). "Electron microscopy: a brief history and review of current clinical application." In: *Histopathology: Methods and Protocols*, pp. 119–135.

Gorelick, Sergey, Genevieve Buckley, Gediminas Gervinskas, Travis K Johnson, Ava Handley, Monica Pia Caggiano, James C Whisstock, Roger Pocock, and Alex de Marco (2019). "PIE-scope, integrated cryo-correlative light and FIB/SEM microscopy." In: *eLife* 8, e45919.

Grauw, Cees J de, Jurrien M Vroom, Hans TM van der Voort, and Hans C Gerritsen (1999). "Imaging properties in two-photon excitation microscopy and effects of refractive-index mismatch in thick specimens." In: *Applied optics* 38.28, pp. 5995–6003.

Guaita, Margherita, Scott C Watters, and Sarah Loerch (2022). "Recent advances and current trends in cryo-electron microscopy." In: *Current opinion in structural biology* 77, p. 102484.

Hagen, Christoph, Kyle C Dent, Tzviya Zeev-Ben-Mordehai, Michael Grange, Jens B Bosse, Cathy Whittle, Barbara G Klupp, C Alistair Siebert, Daven Vasishtan, Felix JB Bäuerlein, et al. (2015). "Structural basis of vesicle formation at the inner nuclear membrane." In: *Cell* 163.7, pp. 1692–1701.

Haguenau, F, PW Hawkes, JL Hutchison, B Satiat-Jeunemaître, GT Simon, and DB Williams (2003). "Key events in the history of electron microscopy." In: *Microscopy and Microanalysis* 9.2, pp. 96–138.

Harris, J Robin (2015). "Transmission electron microscopy in molecular structural biology: a historical survey." In: *Archives of biochemistry and biophysics* 581, pp. 3–18.

Hawkes, Peter W and John CH Spence (2007). *Science of microscopy*. Vol. 1. Springer.

Hayles, MF, DJ Stokes, D Phifer, and KC Findlay (2007). "A technique for improved focused ion beam milling of cryo-prepared life science specimens." In: *Journal of microscopy* 226.3, pp. 263–269.

Hell, S, G Reiner, C Cremer, and Ernst HK Stelzer (1993). "Aberrations in confocal fluorescence microscopy induced by mismatches in refractive index." In: *Journal of microscopy* 169.3, pp. 391–405.

Herzik Jr, Mark A, Mengyu Wu, and Gabriel C Lander (2017). "Achieving better-than-3-Å resolution by single-particle cryo-EM at 200 keV." In: *Nature methods* 14.11, pp. 1075–1078.

Hickey, Shane M, Ben Ung, Christie Bader, Robert Brooks, Joanna Lazniewska, Ian RD Johnson, Alexandra Sorvina, Jessica Logan, Carmela Martini, Courtney R Moore,

et al. (2021). “Fluorescence microscopy—An outline of hardware, biological handling, and fluorophore considerations.” In: *Cells* 11.1, p. 35.

Hylton, Ryan K and Matthew T Swulius (2021). “Challenges and triumphs in cryo-electron tomography.” In: *Iscience* 24.9, p. 102959.

Inc, Plotly Technologies (Nov. 2023). *Dash*. Version 2.14. URL: https://github.com/plotly/dash.

Jedrzejczak-Silicka, Magdalena (2017). “History of cell culture.” In: *New insights into cell culture technology* 1, p. 13.

Jenkins, Francis Arthur (1976). *Fundamentals of Optics: By Francis A. Jenkins and Harvey E. White*. Tech. rep. McGraw-Hill.

Katayama, Hiroyuki, Akitsugu Yamamoto, Noboru Mizushima, Tamotsu Yoshimori, and Atsushi Miyawaki (2008). “GFP-like proteins stably accumulate in lysosomes.” In: *Cell structure and function* 33.1, pp. 1–12.

Kaufmann, Rainer, Christoph Hagen, and Kay Grünewald (2014). “Fluorescence cryo-microscopy: current challenges and prospects.” In: *Current opinion in chemical biology* 20, pp. 86–91.

Keller, Joseph B (1962). “Geometrical theory of diffraction.” In: *Josa* 52.2, pp. 116–130.

Kelley, Kotaro, Ashleigh M Raczkowski, Oleg Klykov, Pattana Jaroenlak, Daija Bobe, Mykhailo Kopylov, Edward T Eng, Gira Bhabha, Clinton S Potter, Bridget Carragher, et al. (2022). “Waffle Method: A general and flexible approach for improving throughput in FIB-milling.” In: *Nature Communications* 13.1, pp. 1–13.

Kelley, Ron, Sagar Khavnekar, Ricardo D Righetto, Jessica Heebner, Martin Obr, Xianjun Zhang, Saikat Chakraborty, Grigory Tagiltsev, Alicia K Michael, Sofie van Dorst, et al. (2024). “Towards community-driven visual proteomics with large-scale cryo-electron tomography of Chlamydomonas reinhardtii.” In: *bioRxiv*, pp. 2024–12.

Kim, Boyoung and Takeshi Naemura (2016). “Blind deconvolution of 3D fluorescence microscopy using depth-variant asymmetric PSF.” In: *Microscopy Research and Technique* 79.6, pp. 480–494.

Kimura, Shunsuke, Takeshi Noda, and Tamotsu Yoshimori (2007a). “Dissection of the Autophagosome Maturation Process by a Novel Reporter Protein, Tandem Fluorescent-Tagged LC3.” In: *Autophagy* 3.5. PMID: 17534139, pp. 452–460. DOI: 10.4161/auto.4451. eprint: https://doi.org/10.4161/auto.4451. URL: https://doi.org/10.4161/auto.4451.

– (2007b). “Dissection of the autophagosome maturation process by a novel reporter protein, tandem fluorescent-tagged LC3.” In: *Autophagy* 3.5, pp. 452–460.

Kofman, Vincent, Jiao He, Inge Loes ten Kate, and Harold Linnartz (2019). “The refractive index of amorphous and crystalline water ice in the UV–vis.” In: *The Astrophysical Journal* 875.2, p. 131.

Koning, Roman I, Abraham J Koster, and Thomas H Sharp (2018). “Advances in cryo-electron tomography for biology and medicine.” In: *Annals of Anatomy-Anatomischer Anzeiger* 217, pp. 82–96.

Kuba, Jakub, John Mitchels, Miloš Hovorka, Philipp Erdmann, Lukáš Berka, Robert Kirmse, Julia Koenig, Jan De Bock, Bernhard Goetze, and Alexander Rigort (2021).

"Advanced cryo-tomography workflow developments–correlative microscopy, milling automation and cryo-lift-out." In: *Journal of Microscopy* 281.2, pp. 112–124.

Kuhm, Tanja, Clémence Taisne, Cecilia de Agrela Pinto, Luca Gross, Evdokia A. Giannopoulou, Stefan T. Huber, Els Pardon, Jan Steyaert, Sander J. Tans, and Arjen J. Jakobi (2025). "Structural basis of antimicrobial membrane coat assembly by human GBP1." In: *Nature Structural & Molecular Biology* 32.1, pp. 172–184.

Kutsch, Miriam, Linda Sistemich, Cammie F Lesser, Marcia B Goldberg, Christian Herrmann, and Jörn Coers (2020). "Direct binding of polymeric GBP1 to LPS disrupts bacterial cell envelope functions." In: *The EMBO journal* 39.13, e104926.

Lasker, Keren, Steven Boeynaems, Vinson Lam, Daniel Scholl, Emma Stainton, Adam Briner, Maarten Jacquemyn, Dirk Daelemans, Ashok Deniz, Elizabeth Villa, et al. (2022). "The material properties of a bacterial-derived biomolecular condensate tune biological function in natural and synthetic systems." In: *Nature Communications* 13.1, p. 5643.

Last, Mart GF, Lenard M Voortman, and Thomas H Sharp (2023). "Measuring cryo-TEM sample thickness using reflected light microscopy and machine learning." In: *Journal of Structural Biology* 215.2, p. 107965.

Lempicki, A and J Glodo (1998). "Ce-doped scintillators: LSO and LuAP." In: *Nuclear Instruments and Methods in Physics Research Section A: Accelerators, Spectrometers, Detectors and Associated Equipment* 416.2-3, pp. 333–344.

Lerou, P. P. P. M., H. J. M. ter Brake, H. V. Jansen, J. F. Burger, H. J. Holland, and H. Rogalla (2008). "Micromachined Joule-Thomson Coolers." In: *AIP Conference Proceedings* 985.1, pp. 614–621.

Li, Shuoguo, Ziyan Wang, Xing Jia, Tongxin Niu, Jianguo Zhang, Guoliang Yin, Xiaoyun Zhang, Yun Zhu, Gang Ji, and Fei Sun (2023). "ELI trifocal microscope: a precise system to prepare target cryo-lamellae for in situ cryo-ET study." In: *Nature Methods* 20.2, pp. 276–283.

Li, Weixing, Jing Lu, Ke Xiao, Maoge Zhou, Yuanyuan Li, Xiang Zhang, Zhixun Li, Lusheng Gu, Xiaojun Xu, Qiang Guo, et al. (2023). "Integrated multimodality microscope for accurate and efficient target-guided cryo-lamellae preparation." In: *Nature Methods* 20.2, pp. 268–275.

Loginov, SV, DB Boltje, Myron NF Hensgens, Jacob P Hoogenboom, and EB Van Der Wee (Apr. 2024). "Depth-dependent scaling of axial distances in light microscopy." In: *bioRxiv* 60.4, pp. 2024–01. DOI: 10.1364/OPTICA.520595. URL: https://opg.optica.org/optica/abstract.cfm?URI=optica-11-4-553.

Lucas, Bronwyn A (2023). "Visualizing everything, everywhere, all at once: Cryo-EM and the new field of structureomics." In: *Current Opinion in Structural Biology* 81, p. 102620.

Lyakin, DV, LA Maksimova, A Yu Sdobnov, and VP Ryabukho (2017). "The influence of the numerical aperture of a beam probing an object on the determination of the thickness of a layered object in confocal microscopy." In: *Optics and Spectroscopy* 123, pp. 487–494.

Mahamid, Julia, Stefan Pfeffer, Miroslava Schaffer, Elizabeth Villa, Radostin Danev, Luis Kuhn Cuellar, Friedrich Förster, Anthony A Hyman, Jürgen M Plitzko, and Wolfgang Baumeister (2016). "Visualizing the molecular sociology at the HeLa cell nuclear periphery." In: *Science* 351.6276, pp. 969–972.

Marko, M, C Hsieh, W Moberlychan, CA Mannella, and J Frank (2006). "Focused ion beam milling of vitreous water: prospects for an alternative to cryo-ultramicrotomy of frozen-hydrated biological samples." In: *Journal of microscopy* 222.1, pp. 42–47.

Marko, M, CE Hsieh, R Shalek, C Ting, C Mannella, and J Frank (2006). "Focused ion beam (FIB) preparation methods for 3-D biological cryo-TEM." In: *Microscopy and Microanalysis* 12.S02, pp. 98–99.

Marko, Michael, Chyongere Hsieh, Richard Schalek, Joachim Frank, and Carmen Mannella (2007). "Focused-ion-beam thinning of frozen-hydrated biological specimens for cryo-electron microscopy." In: *Nature methods* 4.3, pp. 215–217.

Masters, Barry R (2009). "History of the electron microscope in cell biology." In: *eLS*.

Mathieu, Cécile, Rohit V Pappu, and J Paul Taylor (2020). "Beyond aggregation: Pathological phase transitions in neurodegenerative disease." In: *Science* 370.6512, pp. 56–60.

Mierlo, Willem van, Dorin Geiger, Alan Robins, Matthias Stumpf, Mary Louise Ray, Paul Fischione, and Ute Kaiser (2014). "Practical aspects of the use of the X2 holder for HRTEM-quality TEM sample preparation by FIB." In: *Ultramicroscopy* 147, pp. 149–155.

Monaghan, Perusinghe, and Müller (1998). "High-pressure freezing for immunocytochemistry." In: *Journal of Microscopy* 192.3, pp. 248–258. DOI: https://doi.org/10.1046/j.1365-2818.1998.00387.x. URL: https://onlinelibrary.wiley.com/doi/abs/10.1046/j.1365-2818.1998.00387.x.

Nickell, Stephan, Christine Kofler, Andrew P Leis, and Wolfgang Baumeister (2006). "A visual approach to proteomics." In: *Nature reviews Molecular cell biology* 7.3, pp. 225–230.

Paul-Gilloteaux, Perrine, Xavier Heiligenstein, Martin Belle, Marie-Charlotte Domart, Banafshe Larijani, Lucy Collinson, Graça Raposo, and Jean Salamero (2017). "eC-CLEM: flexible multidimensional registration software for correlative microscopies." In: *Nature methods* 14.2, pp. 102–103.

Pawley, James (2006). *Handbook of biological confocal microscopy*. Vol. 236. Springer Science & Business Media.

Petrov, Petar N and WE Moerner (2020). "Addressing systematic errors in axial distance measurements in single-emitter localization microscopy." In: *Optics express* 28.13, pp. 18616–18632.

Pidol, Ludivine, Andrée Kahn-Harari, Bruno Viana, Eric Virey, Bernard Ferrand, Pieter Dorenbos, Johan TM de Haas, and Carel WE van Eijk (2004). "High efficiency of lutetium silicate scintillators, Ce-doped LPS, and LYSO crystals." In: *IEEE Transactions on Nuclear Science* 51.3, pp. 1084–1087.

Piel, Éric et al. (Apr. 2022). *Open Delmic Microscope Software*. Version 3.2.0. URL: https://www.delmic.com/.

Pimblott, Simon M, Jay A LaVerne, A Mozumder, and Nicholas JB Green (1990). "Structure of electron tracks in water. 1. Distribution of energy deposition events." In: *Journal of Physical Chemistry* 94.1, pp. 488–495.

Prasher, Douglas C, Virginia K Eckenrode, William W Ward, Frank G Prendergast, and Milton J Cormier (1992). "Primary structure of the Aequorea victoria green-fluorescent protein." In: *Gene* 111.2, pp. 229–233.

Quorum Technologies Ltd (June 2021). *PP3006 CoolLok brochure*. v4.

Randow, Felix, John D. MacMicking, and Leo C. James (2013). "Cellular Self-Defense: How Cell-Autonomous Immunity Protects Against Pathogens." In: *Science* 340.6133, pp. 701–706.

Renz, Malte (2013). "Fluorescence microscopy—A historical and technical perspective." In: *Cytometry Part A* 83.9, pp. 767–779.

Ribatti, Domenico (2018). "An historical note on the cell theory." In: *Experimental cell research* 364.1, pp. 1–4.

Rigort, Alexander, Felix JB Bäuerlein, Elizabeth Villa, Matthias Eibauer, Tim Laugks, Wolfgang Baumeister, and Jürgen M Plitzko (2012). "Focused ion beam micromachining of eukaryotic cells for cryoelectron tomography." In: *Proceedings of the National Academy of Sciences* 109.12, pp. 4449–4454.

Rivera-Cuevas, Yolanda, Barbara Clough, and Eva-Maria Frickel (2023). "Human guanylate-binding proteins in intracellular pathogen detection, destruction, and host cell death induction." In: *Current Opinion in Immunology* 84, p. 102373.

Santos, José Carlos, Mathias S Dick, Brice Lagrange, Daniel Degrandi, Klaus Pfeffer, Masahiro Yamamoto, Etienne Meunier, Pawel Pelczar, Thomas Henry, and Petr Broz (2018). "LPS targets host guanylate‐binding proteins to the bacterial outer membrane for non‐canonical inflammasome activation." In: *The EMBO Journal* 37.6, e98089.

Saxena, Manish, Gangadhar Eluru, and Sai Siva Gorthi (2015). "Structured illumination microscopy." In: *Advances in Optics and Photonics* 7.2, pp. 241–275.

Schaffer, Miroslava, Stefan Pfeffer, Julia Mahamid, Stephan Kleindiek, Tim Laugks, Sahradha Albert, Benjamin D Engel, Andreas Rummel, Andrew J Smith, Wolfgang Baumeister, et al. (2019). "A cryo-FIB lift-out technique enables molecular-resolution cryo-ET within native Caenorhabditis elegans tissue." In: *Nature methods* 16.8, pp. 757–762.

Schiøtz, Oda Helene, Christoph JO Kaiser, Sven Klumpe, Dustin R Morado, Matthias Poege, Jonathan Schneider, Florian Beck, David P Klebl, Christopher Thompson, and Jürgen M Plitzko (2023). "Serial Lift-Out: sampling the molecular anatomy of whole organisms." In: *Nature Methods*, pp. 1–9.

Schneider, Jonathan and Marion Jasnin (2024). "Molecular architecture of the actin cytoskeleton: From single cells to whole organisms using cryo-electron tomography." In: *Current Opinion in Cell Biology* 88, p. 102356.

Sexton, Danielle L, Steffen Burgold, Andreas Schertel, and Elitza I Tocheva (2022). "Super-resolution confocal cryo-CLEM with cryo-FIB milling for in situ imaging of Deinococcus radiodurans." In: *Current Research in Structural Biology* 4, pp. 1–9.

Sheppard, CJR and Peter Tö rö k (1997). "Effects of specimen refractive index on confocal imaging." In: *Journal of microscopy* 185.3, pp. 366–374.

Siemons, Marijn E, Lukas C Kapitein, and Sjoerd Stallinga (2022). "Axial accuracy in localization microscopy with 3D point spread function engineering." In: *Optics Express* 30.16, pp. 28290–28300.

Skoupỳ, Radim, Daan B Boltje, Miroslav Slouf, Kateřina Mrázová, Tomáš Láznička, Clémence M Taisne, Vladislav Krzyžánek, Jacob P Hoogenboom, and Arjen J Jakobi (2023). "Robust Local Thickness Estimation of Sub-Micrometer Specimen by 4D-STEM." In: *Small Methods* 7.9, p. 2300258.

SmarAct GmbH (2021). *High Precision Positioning and Metrology Solutions - SmarAct*. https://www.smaract.com/index-en (Retrieved 13-09-2021).

Smeets, Marit, Anna Bieber, Cristina Capitanio, Oda Schioetz, Thomas van der Heijden, Andries Effting, Éric Piel, Bassim Lazem, Philipp Erdmann, and Juergen Plitzko (2021). "Integrated Cryo-Correlative Microscopy for Targeted Structural Investigation In Situ." In: *Microscopy Today* 29.6, pp. 20–25.

Stallinga, Sjoerd (2005). "Finite conjugate spherical aberration compensation in high numerical-aperture optical disc readout." In: *Applied optics* 44.34, pp. 7307–7312.

Stamnes, Jakob J (2002). "Waves, rays, and the method of stationary phase." In: *Optics express* 10.16, pp. 740–751.

Stelzer, Ernst HK, Frederic Strobl, Bo-Jui Chang, Friedrich Preusser, Stephan Preibisch, Katie McDole, and Reto Fiolka (2021). "Light sheet fluorescence microscopy." In: *Nature Reviews Methods Primers* 1.1, p. 73.

Stokes, GG (1849). "On a mode of measuring the astigmatism of a defective eye." In: *Rep. Br. Assoc* 2, pp. 10–11.

Subramaniya, Sai Raghavendra Maddhuri Venkata, Genki Terashi, and Daisuke Kihara (2021). "Super resolution Cryo-EM maps with 3D deep generative networks." In: *Biophysical Journal* 120.3, 283a.

Surface preparation laboratory (2023). *Premier supplier of single crystal surfaces - SPL*. https://www.spl.eu/ (Retrieved 14-09-2023).

Tacke, Sebastian, Philipp Erdmann, Zhexin Wang, Sven Klumpe, Michael Grange, Jürgen Plitzko, and Stefan Raunser (2021). "A streamlined workflow for automated cryo focused ion beam milling." In: *Journal of Structural Biology* 213.3, p. 107743. ISSN: 1047-8477.

Tegunov, Dimitry, Liang Xue, Christian Dienemann, Patrick Cramer, and Julia Mahamid (2021). "Multi-particle cryo-EM refinement with M visualizes ribosome-antibiotic complex at 3.5 Å in cells." In: *Nature Methods* 18.2, pp. 186–193.

ThermoFisher Scientific (May 2021). *iFLM Correlative System*. ds0366. Rev. 1.2.

– (Sept. 2024). *Arctis Cryo-Plasma-FIB*. https://www.thermofisher.com/order/catalog/product/ARCTIS (Retrieved 14-09-2024).

Thompson, Silvanus P (1899). "On Obliquely-crossed Cylindrical Lenses." In: *Proceedings of the Physical Society of London (1874-1925)* 17.1, p. 81.

Timmermans, Frank Jan and Cornelis Otto (2015). "Contributed review: Review of integrated correlative light and electron microscopy." In: *Review of scientific instruments* 86.1.

Toro-Nahuelpan, Mauricio, Ievgeniia Zagoriy, Fabrice Senger, Laurent Blanchoin, Manuel Théry, and Julia Mahamid (2020). "Tailoring cryo-electron microscopy grids by photo-micropatterning for in-cell structural studies." In: *Nature methods* 17.1, pp. 50–54.

Turk, Martin and Wolfgang Baumeister (2020). "The promise and the challenges of cryo-electron tomography." In: *FEBS letters* 594.20, pp. 3243–3261.

Utke, Ivo, Patrik Hoffmann, and John Melngailis (2008). "Gas-assisted focused electron beam and ion beam processing and fabrication." In: *Journal of Vacuum Science & Technology B: Microelectronics and Nanometer Structures Processing, Measurement, and Phenomena* 26.4, pp. 1197–1276.

Villa, Elizabeth, Miroslava Schaffer, Jürgen M Plitzko, and Wolfgang Baumeister (2013). "Opening windows into the cell: focused-ion-beam milling for cryo-electron tomography." In: *Current opinion in structural biology* 23.5, pp. 771–777.

Virtanen, Pauli, Ralf Gommers, Travis E Oliphant, Matt Haberland, Tyler Reddy, David Cournapeau, Evgeni Burovski, Pearu Peterson, Warren Weckesser, Jonathan Bright, et al. (2020). "SciPy 1.0: fundamental algorithms for scientific computing in Python." In: *Nature methods* 17.3, pp. 261–272.

Visser, TD, JL Oud, and GJ Brakenhoff (1996). "Refractive index and axial distance measurements in 3-D microscopy." In: *SPIE MILESTONE SERIES MS* 131, pp. 286–289.

Vulović, Miloš, Raimond BG Ravelli, Lucas J van Vliet, Abraham J Koster, Ivan Lazić, Uwe Lücken, Hans Rullgård, Ozan Öktem, and Bernd Rieger (2013). "Image formation modeling in cryo-electron microscopy." In: *Journal of structural biology* 183.1, pp. 19–32.

Wagner, Felix R, Reika Watanabe, Ruud Schampers, Digvijay Singh, Hans Persoon, Miroslava Schaffer, Peter Fruhstorfer, Jürgen Plitzko, and Elizabeth Villa (2020). "Preparing samples from whole cells using focused-ion-beam milling for cryo-electron tomography." In: *Nature protocols* 15.6, pp. 2041–2070.

Wee, Ernest Benjamin van der, Daan Benjamin Boltje, and Sergey Loginov (June 2023). *Re-scaling factor online plotting tool*. Version 0.1. URL: https://github.com/hoogenboom-group/SF.

Wikimedia, Commons (2002). *Scanning electron micrograph of Escherichia coli, grown in culture and adhered to a cover slip.* File: E. coli Bacteria (7316101966).jpg. URL: %5Curl%7Bhttps://en.m.wikipedia.org/wiki/File:E._coli_Bacteria_%287316101966%29.jpg%7D.

– (2010). *An image of a Human cancer cell dividing. Taken with an epifluorescence microscope.* File: Dividing_Cell_Fluorescence.jpg. URL: %5Curl%7Bhttps://commons.wikimedia.org/wiki/File:Dividing_Cell_Fluorescence.jpg%7D.

– (2015). *Central slice through a cryotomogram of an intact Bdellovibrio bacteriovorus cell*. File: Slice_from_electron_cryotomogram_of_Bdellovibrio_bacteriovorus_cell.jpg. URL: %5Curl%7Bhttps://en.m.wikipedia.org/wiki/File:Slice_from_electron_cryotomogram_of_Bdellovibrio_%5C%5C%20bacteriovorus_cell.jpg%7D.
– (2018). *Quadriviridae. Transmission electron micrograph of vitrified virions, and three-dimensional cryo-electron microscopy reconstruction of RnQV1 virions at 8Å resolution*. File: ODR.Quadri.fig1.png. URL: %5Curl%7Bhttps://commons.wikimedia.org/wiki/File:ODR.Quadri.fig1.png%7D.

Wolf, E (1959). "A scalar representation of electromagnetic fields: II." In: *Proceedings of the Physical Society* 74.3, p. 269.

Wolff, Georg, Christoph Hagen, Kay Grünewald, and Rainer Kaufmann (2016). "Towards correlative super-resolution fluorescence and electron cryo-microscopy." In: *Biology of the Cell* 108.9, pp. 245–258.

Wolff, Georg, Ronald WAL Limpens, Shawn Zheng, Eric J Snijder, David A Agard, Abraham J Koster, and Montserrat Bárcena (2019). "Mind the gap: Micro-expansion joints drastically decrease the bending of FIB-milled cryo-lamellae." In: *Journal of Structural Biology* 208.3, p. 107389.

Yesibolati, Murat Nulati, Simone Laganá, Shima Kadkhodazadeh, Esben Kirk Mikkelsen, Hongyu Sun, Takeshi Kasama, Ole Hansen, Nestor J Zaluzec, and Kristian Mølhave (2020). "Electron inelastic mean free path in water." In: *Nanoscale* 12.40, pp. 20649–20657.

Zens, Bettina, Florian Fäßler, Jesse M Hansen, Robert Hauschild, Julia Datler, Victor-Valentin Hodirnau, Vanessa Zheden, Jonna Alanko, Michael Sixt, and Florian KM Schur (2024). "Lift-out cryo-FIBSEM and cryo-ET reveal the ultrastructural landscape of extracellular matrix." In: *Journal of Cell Biology* 223.6, e202309125.

Zimmerli, Christian E, Matteo Allegretti, Vasileios Rantos, Sara K Goetz, Agnieszka Obarska-Kosinska, Ievgeniia Zagoriy, Aliaksandr Halavatyi, Gerhard Hummer, Julia Mahamid, Jan Kosinski, et al. (2021). "Nuclear pores dilate and constrict in cellulo." In: *Science* 374.6573, eabd9776.

Zonnevylle, AC, RFC Van Tol, N Liv, AC Narvaez, APJ Effting, P Kruit, and JP Hoogenboom (2013). "Integration of a high-NA light microscope in a scanning electron microscope." In: *Journal of microscopy* 252.1, pp. 58–70.

COLOPHON

CRYOGENIC, COINCIDENT FLUORESCENCE, ELECTRON, AND ION BEAM MICROSCOPY

DAAN BENJAMIN BOLTJE

JUNE 20, 2025

This document was typeset using the typographical look-and-feel `classicthesis v4.6` developed by André Miede and Ivo Pletikosić. The style was inspired by Robert Bringhurst's seminal book on typography "*The Elements of Typographic Style*". The color scheme used is derived from the `Fire LUT` as implemented in `ImageJ`, whilst humming the 1968 song *Fire* by Arthur Brown, starting with the exclamation: *I am the god of hellfire! And I bring you - Fire.*